EXTENSIONAL FLOW PHENOMENA
IN POLYMER SOLUTIONS

A Dissertation

Presented to

the Faculty of the Department of Chemical Engineering

University of Houston

In Partial Fulfillment

of the Requirements for the Degree

Doctor of Philosophy in Chemical Engineering

---

by

Joseph Ching-hsiang Hsu

December 1975

ACKNOWLEDGEMENTS

The author is deeply indebted to Professor R.W. Flumerfelt for his guidance and help throughout the course of this dissertation research.

The author also wishes to thank Professor R.L. Everett, Professor W.P. Schneider, and Mr. C. Tracy of the Electrical Engineering Department for their helpful work and suggestions on the control and light sensing assembly of the apparatus.

Sincere acknowledgements are due to Mr. Roy M. Priest, Mr. Lee Bennet, Mr. J. Richard, and Mr.H. Flores for their assistance in contructing the experimental apparatus; Mr. James Payne and Mr. Mike Smith for their help in building the analog electronic devices; and Mr. Herb Kent for his kindly administrative assistance.

A very special gratitude should be expressed to the author's beloved wife, Emily, whose sacrifice, patience, and love have been an incomparable drive in the completion of this work.

Finally, the author is glad to dedicate this dissertation to his paraents and his wife with all his love.

EXTENSIONAL FLOW PHENOMENA

IN POLYMER SOLUTIONS

An Abstract of a Dissertation

Presented to

the Faculty of the Department of Chemical Engineering

In Partial Fulfillment

of the Requirements for the Degree

Doctor of Philosophy in Chemical Engineering

---

by

Joseph Ching-hsiang Hsu

December 1975

ABSTRACT

The objective of the present work was to develop techniques for establishing uniaxial extensional flow and to use these techniques to study the extensional flow response of polymer solutions. To this end, an elongation drop apparatus was built in which either the extension rate or the imposed stress could be controlled. A Newtonian silicone oil and two viscoelastic polymer solutions (10% polyisobutylene in Decalin(PIB) and 2.8% Separan AP 30 in 50:50 glycerol-water solution(PAA)) were tested in both stress growth (controlled extension rate) and approximate creep (controlled stress) experiments. Viscometric flow measurements were also performed on the polymer solutions using the Weissenberg Rheogoniometer.

Extensional flow tests with the Newtonian silicone oil established the capabilities of the drop elongation apparatus. The prescribed responses in both stress growth and approximate creep experiments were reached within a time period of less than one second. The steady extensional viscosities obtained from both experiments were in good agreement with Trouton's law.

From the extensional flow tests with the two polymer solutions, the steady extensional viscosities for both PIB and PAA were found to increase with increasing extension rate over a range of extension rates from 0.003 sec^{-1} to o.035 sec^{-1} for

PIB and from 0.003 sec^{-1} to 0.016 sec^{-1} for PAA. Two models(the Bird-Carreau model and the truncated Goddard expension) were tested with the experimental results. The parameters in both models were determined by fitting the viscometric and steady extensional flow data with the viscometric and steady extensional flow data being weighted equally. Predictions of both models were in poor agreement with the transient extensional flow data on the two polymer solutions. For the viscometric and steady extensional flow data, the Bird-Carreau model described the observed behavior better than the truncated Goddard expansion.

In addition, several analyses were performed to estimate the interfacial effects in the drop elongation experiments. The analysis based on the assumption that the fluids near the end of the drop surface experience extensional flow was found to be the most satisfactory when compared with experimental results.

TABLE OF CONTENTS

LIST OF FIGURES

LIST OF TABLES

CHAPTER I

INTRODUCTION

The behavior of polymeric materials in extensional flow is pragmatically important, since this type of flow occurs in such processes as fibre spinning, film drawing and certain extrusion operations. In each of these processes, the predominant motion is elongation, caused by differential motions of mechanical boundaries. Problems such as melt fracture in extrusion and draw resonance in fibre spinning are probably related to the elongational character of these operations. Thus, the behavior of polymeric materials in extensional flow has become a subject of much interest.

Beyond this practical motivation, there is a fundamental interest in the behavior of fluid materials subjected to this motion. While the great majority of rheological investigations are expended to the study of polymeric, non-Newtonian fluids under shear conditions, little work has been done with extensional flow. In addition, many forms of constitutive equations which are currently popular predict widely different responses for the relation between stress and strain rate in extensional flow. Thus the extensional flow data would be quite valuable both to test existing constitutive equations and to guide the future development of others.

In recent years, a number of experiments have been conducted to determine the extensional viscosity of several different materials. Because of the experimental difficulty of generating a well defined extensional flow field where the kinematic and dynamic conditions can be measured, most of these works have been limited by either very restrictive low levels of strain rate (1-3), inaccurate analyses of the deformation process (4), or uncertainties in stress measurement due to changing strain histories (5-7). The limited amount of quantitatively reliable data has been obtained mainly for molten polymers or solutions with high viscosity(10^5 poise). Materials with viscosities lower than 10^5 poise are encountered in many commercial operations. To date, few well defined experimental techniques for studying extensional flow behavior of low to moderate viscosity materials have been established.

In this connection, an elongating drop technique has been proposed by Hsu and Flumerfelt(8). Using an experimental technique first suggested by Vonnegut(9), and extended later by Princen(10), Princen, Zia, and Mason(11), and Wade et.al. (69) for measuring the interfacial tension, a liquid drop of interest is placed horizontally along the axis of a glass cylinder filled with an immiscible liquid of high density. At increasingly high speeds of rotation, an initially spherical drop is elongated along the axis of the cylinder. The extensional flow properties of the drop phase can be obtained by knowing the drop dynamics during extension and the variables which affect it. This technique has been verified successfully(8) by testing a Newtonian fluid drop (ASTM Standard Oil). However, for proper use of this technique, a more sophisticated experimental apparatus is required. In particular, either the extension rate or the imposed stress must be controllable.

The purpose of the work presented here is to construct such an apparatus and test it. To this end, a controlled rotating cylinder apparatus was built. The kinematics of the drop are controlled by employing a feedback loop where the instantaneous drop diameter is measured with a photomultiplier tube assembly and compared with a prescribed diameter signal from a function generator. Any existing difference between the values of those two signals will result in appropriate changes in the rotational speed of the apparatus. With this apparatus, a Newtonian silicone oil and two viscoelastic polymer solutions (10% polyisobutylene in Decalin and 2.8% Separan AP 30 in 50-50 glycerin-water solution) have been tested in both controlled extension rate and creep experiments. In addition, the dynamics of the drop elongation phenomena, particularly, the resulting shape, internal flow patterns etc., have been analyzed. This involves the solution of a free surface problem using approximate methods such as orthogonal collocation and least squares. Finnally, the extensional flow data obtained with the viscoelstic polymer solutions were compared with the predictions of the Bird-

Carreau model (12) and Truncated Goddard Expansion model (13). In addition to providing a basis for discrimination between constitutive equation, these studies provide various insight into the response of polymeric material in extensional flow.

CHAPTER II

BACKGROUND

2-1. Definition

Extensional flows have been defined in several ways (14-17). In this work, using the rectangular Cartesian co-ordinate system, an extensional flow is defined as one in which the components of the velocity of a material point having coordinates (x_1, x_2, x_3) are given as follows:

$$V_i = \bar{a}_i x_i \qquad \text{(no summation)} \qquad (2\text{-}1\text{-}1)$$

In general, $\bar{a}_i$ are defined by equation (2-1-1) and may be arbitrary functions of time and of ith coordinate but not of the remaining two coordinate directions. If $\bar{a}_i$ are constant, the extension is steady and uniform. In such a case, the rate of deformation tensor, $\Delta_{ij} = \frac{1}{2}\left(\frac{\partial V_i}{\partial x_j} + \frac{\partial V_j}{\partial x_i}\right)$ (2-1-2) reduces to the simple form:

$$[\Delta_{ij}] = \begin{bmatrix} \bar{a}_1 & 0 & 0 \\ 0 & \bar{a}_2 & 0 \\ 0 & 0 & \bar{a}_3 \end{bmatrix} \qquad (2\text{-}1\text{-}3)$$

In the special case of uniaxial extensional flow in, say, the "1" direction, the continuity equation insures

$$\bar{a}_1 = \dot{\bar{\gamma}}, \quad \bar{a}_2 = \bar{a}_3 = -\frac{\bar{a}_1}{2} = -\frac{\dot{\bar{\gamma}}}{2} \qquad (2\text{-}1\text{-}4)$$

where $\dot{\bar{\gamma}}$ is the extension rate defined by Middleman (18). By comparison, the kinematics of a simple steady shear flow are written as follows:

$$V_1 = a_5 x_2, \quad V_2 = 0 = V_3 \qquad (2\text{-}1\text{-}5)$$

Here, a_5 is the shear rate and the equation of continuity is satisfied identically.

The extensional viscosity , $\bar{\eta}$, is defined as the ratio of the primary normal stress difference $\Pi_{11}-\Pi_{22}$ to the extension rate $\dot{\bar{\gamma}}$:

$$\bar{\eta} = \frac{\Pi_{11}-\Pi_{22}}{\dot{\bar{\gamma}}} \qquad (2\text{-}1\text{-}6)$$

which can be easily proved to be a unique function of extension rate $\dot{\bar{\gamma}}$ (15).

2-2. Theoretical Predictions of The Extensional Viscosity

The relationship between the present state of stress in a material and the complete history of the motion of that material is called a constitutive equation. The equation can take various forms, depending upon one's previous understanding of the behavior of materials and conceptual notions of realistic material response.

Newtonian fluids can be characterized by the following constitutive equation

$$\tau_{ij} = 2\eta_0 \Delta_{ij} \qquad (2\text{-}2\text{-}1)$$

where η_0 , the shear viscosity, is a constant coefficient and Δ_{ij} is the rate of deformation tensor defined by equation (2-1-2).

A straightforward calculation shows that for Newtonian fluids the extensional viscosity is independent of extension rate and is a constant multiple of the shear viscosity:

$$\bar{\eta} = 3\eta_0 \qquad (2\text{-}2\text{-}2)$$

This is known as Trouton's Law. In the case of pure viscous fluids, the dependence of extensional viscosity on extension rate is qualitatively similar to the dependence of the shear viscosity on the shear rate (5).

A completely different situation arises when visco-elastic fluids are considered. The reasons for this have been discussed in detail by Astarita (19). Basically, the principal axes of the rate-of-deformation ellipsoid always lie on the same material lines for extensional flow, so that such materials having a memory for the past history of deformation are severely stressed, and may be unable to relax stresses more rapidly than they are built up by continuous extensional deformation.

A host of constitutive theories for viscoelastic fluids have been proposed. In particular, theories stemming from the generalization of the simple Maxwell model with constant characteristic times tend to predict an infinite extensional viscosity at some finite extension rate. Such behavior is also characteristic of the Lodge (20,21), Macdonald and Bird (22), Bird and Carreau (12), Meister (23), WJFLMB (24), Bird and Spriggs (25), Fredrickson (26), Walters(27), and Ward and Jenkin(28) theories.

In contrast, a network rupture model by Tanner (29,30) predicts the extensional viscosity $\bar{\eta}$ increasing to a maximum and then decreasing indefinitely. Essentially, this theory is based on the idea that a maximum possible strain exists, above which the network is broken and the memory function collapses to zero. In other words, such materials have finite memories.

In addition to the diverse prediction of the above theories, there are a number of theories such as Bogue (31), Lodge (20), BKZ (32), and Yamamoto (33) which can exhibit both types of response. Astarita (5) classifies such theories as "The first type of complex phenomenological theories." Basically, this type of theory is one where the memory function is assumed to depend on the deformation rate as well as on elapsed time. Since the extensional viscosity is determined by the long time behavior of the memory function, these theories may not predict an infinite extensional viscosity at some critical extension rate.

Comparison of the predictions of several other models have been published by Tanner (34), Astarita and Nicodemo (5), Dealy (35), and by Bird et.al. (36). A list of models for which extensional viscosity predictions have been published is given in Table 2-1.

2-3. Previous Experimental Works and Techniques

Over the past ten years, there has been considerable interest in the material response of polymer melts and solutions in extensional flow. Since the early work of Trouton (42), Ballman (1) in 1965 conducted a series of extensional tests with molten polystyrene. This fluid is, in a sense, rather solid-like, possessing a zero shear viscosity of approximately 10^8 poise and, indeed, the tensile testing machine Ballman used to extend

Table 2-1 Constitutive Equations for Viscoelastic Fluids Which Have Been Used to Predict the Extensional Viscosity $\bar{\eta}$ (from Dealy(35))

Constitutive Equation	Predicts Bounded $\bar{\eta}$ at All Finite $\dot{\gamma}$	Reference for Application to Extensional Flow
2nd-order fluid	Yes	37
3rd-order fluid	Yes	38
Williams-Bird	No	25
Spriggs	No	25
Lodge	No	20
Macdonald-Bird	No	34
Bird-Carreau	No	39
Meister	No	23
Bogue	Yes	40
Tanner-Simmons	Yes	30,34
Yamamoto	yes	36
Carreau	Yes	39
BKZ	Yes	40
Bead [illegible]-spring solution	No	36
Bead-rod solution	yes	36
Non-linear bead-spring	No	41

the specimen of a circular rod is normally used with solid materials. By programming the instrument to accelerate one end of the specimen exponentially, constant extension rate was achieved. Ballman's experiments showed that the experimental extension rates are less than 10^{-2} sec^{-1}, and the extensional viscosity obtained is nearly constant at these extension rates.

In similar experiments, Cogswell(2) measured the extensional viscosity of low density polyethylene and polymethylmethacrylate under the condition of constant extensional stress. The experimental results indicated that the extensional viscosity for polymethylmethacrylate is constant up to extensional stresses equal in magnitude to shear stresses for which the shear viscosity is decreasing. For low density polyethylene, Cogswell reported that the extensional viscosity increases with increasing extensional stress at stresses which are comparable in magnitude to shear stresses at which the shear viscosity is decreasing.

Vinogradov et.al. (3,43-45) have measured the extensional viscosity along with recoverable and irrecoverable components of the extensional strain for polyisobutylene and atactic polystyrene. In their experiments the specimen, an extruded rod which floated on a liquid bath, was extended by a tensile testing machine controlled by an electronic programming device to produce either constant extension rate or constant extensional stress. The experimental results showed a gradual increase in the extensional viscosity with extension rate above 10^{-1} sec^{-1} for polyisobutylene and 10^{-3} sec^{-1} for polystyrene. The recoverable strain for polyisobutylene increased with time to a steady state value at all extension rates investigated, while the recoverable strain for polystyrene reached a steady state value only at low extension rate.

Using an experimental technique similar to Ballman's, Stevenson (46) carried out a series of constant extension rate experiments with an elastomeric copolymer of isobutylene and isoprene. The extensional viscosity was found to be constant at extension rates ranging from 10^{-4} to 10^{-1} sec^{-1}.

Meisser (47,48,49) has developed a novel extensional rheometer and studied low density polyethylene. In Meisser's experiments, each end of a rod-shaped sample was clamped by a pair of gears rotating at a constant angular velocity. The portion of the sample remaining between the two pairs of gears was then stretched at a constant extension rate from 10^{-3} to 1 sec^{-1}. Meisser's data and the subsequent fit (50) from the Lodge's rubberlike liquid strongly suggest that the extensional viscosity increases with increasing extension rate.

Recently, Baily (51) studied Vistanex L-100 in a tensile testing machine at extension rate in the range of 10^{-5} sec^{-1} to 10^{-1} sec^{-1}. The data showed that the extensional viscosity decreases with increasing extension rate.

Another major class of experiments successfully used to measure the extensional viscosity is the bubble inflation technique of Denson and Gallo (52) for equal biaxial extensional flow. A sheet of the testing material is clamped in such a way that the inflated sheet will result in a hemispherical bubble. Near the pole of the bubble, the material experiences a uniform biaxial extensional flow. This bubble inflation technique has been used to study the biaxial extensional flow behavior of different grades of Vistanex polyisobutylene. Joye (53) has found that, for Vistanex L-80,the biaxial extensional viscosity is a decreasing function of extension rate. Maerker and Schowater (54) observed a slight decrease in the biaxial extensional viscosity first and then an increase for two lower molecular weight grades of Vistanex.

A final technique which could be used to measure the extensional flow properties of a viscoelastic fluid is the bubble collapse method of Glearson and Middleman (55). A nearly spherical gas bubble supported by a steel tube is suspended in a fluid to be studied. An uniaxial extensional flow is created while the bubble is forced to collapse by decreasing the pressure inside the bubble. This technique has been used to study Newtonian fluids successfully. The data for two polymer solutions (Hydroxypropylcellulose in water (HPC) and Polyacrylamide in water and glycerine (PA)) showed a decrease in the extensional viscosity with increasing extension rate in the range from 10^{-1} to 10^{1} sec^{-1}. However, it is doubtful that steady state conditions were reached during the experiments. Thus the trend of the extensional viscosity versus extension rate in the data shown is subject to question.

A number of experimental techniques have been used to measure the extensional viscosity with less success than those mentioned above. The main difficulty is associated with creating extensional flow fields which have controllable extension rate and extension rate histories, and in which the resulting stress can be measured. Methods such as fibre spinning methods (7, 56-64), tubeless siphon method (5,65), converging flow through apertures (4,56), and triple jet method (66) do not present well defined and easily controlled steady or unsteady experiments. In many cases the flow field is only approximately elongational and the results are often only of semi-quantitative and qualitative value.

Obviously, a reliable technique for experimentally studying extensional flow behavior for more liquid-like materials over a wider range of extension rate is needed.

2-4. Theory of Elongating Drop Method

Recently in a paper by Hsu and Flumerfelt (8), a promising technique for measuring the extensional flow properties of viscoelastic fluids has been proposed. The details of the analysis of drop dynamics along with the possible rheological applications of this technique have been presented elsewhere (8). A diagram of the system is shown in Fig. 2-1. An immiscible drop is placed in a fluid of higher density which is contained in a cylinder. When the cylinder is rotated, the centrifugal forces resulting from the density differences caused the drop to elongate as shown.

The time dependent response of this system is analyzed subject to the following conditions:

1) The fluids are incompressible and can be classified under the simple fluid theory of Coleman and Noll (67), where the total stress $\Pi_{ij} = -P\delta_{ij} - \tau_{ij}$ at a material point at time t is given by:

$$\Pi_{ij} = -P\delta_{ij} + \mathop{H_{ij}}_{s=0}^{\infty} \left(C_{mn}^{(t)} (t-s) \right) \qquad (2\text{-}4\text{-}1)$$

That is, the stress is related to the "history" of strain measured in terms of Cauchy-Green strain tensor $C_{mn}^{(t)}$ through a tensor functional H_{ij}.

2) The fluids are sufficiently viscous and the angular acceleration $\alpha = \frac{d\omega}{dt}$ is sufficiently small that the fluids rotate in a rigid body manner.

3) The drop and the fluid immediately surrounding it experience uniaxial extensional flow. The r and z components in the region $r < R + \epsilon$ (ϵ being small) are given by:

$$V_r = -\frac{1}{2}\dot{\gamma}(t)\, r \quad ; \quad V_z = \dot{\gamma}(t)\, z \qquad (2\text{-}4\text{-}2)$$

where $\dot{\gamma} = -\frac{2}{r}\frac{dr}{dt} = \frac{1}{z}\frac{dz}{dt}$ is the extension rate.

The assumptions (2) and (3) have been proved to be valid

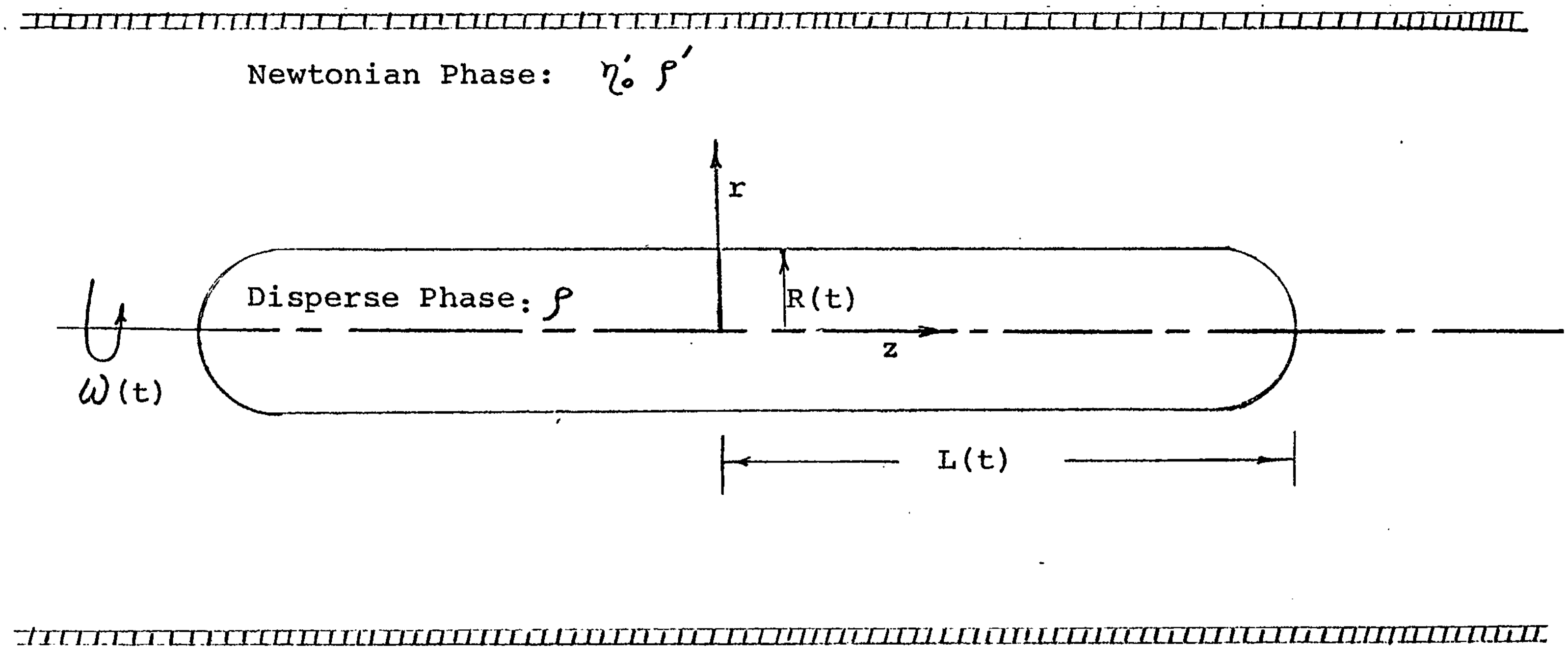

Necessary condition for elongation: $\rho' > \rho$

Figure 2-1 Schematic Represention of Drop Elongation Experiment

(8), and do not appear to be serious limitations of the method.

Since the off-diagonal elements in the stress matrix are zero for extensional flow, the stress field is completely specified by the normal stress (15,17). Also, asymmetry considerations require that $\Pi_{rr} - \Pi_{\theta\theta} = 0$.

If inertial effects other than the centrifugal force term are neglected, as well as the body force term, the r component of the equation of motion can be integrated to give:

$$\Pi_{rr} = -\frac{1}{2}\rho(\omega r)^2 + f(z,t) \tag{2-4-3}$$

the function f(z,t) can be determined from Laplace's equation for conditions at the interface at r=R; i.e.

$$\Pi_{rr}(R) = \Pi_{rr}'(R) - \frac{\sigma}{R} \tag{2-4-4}$$

where Π_{rr}' represents the stress component in the surrounding fluid and σ the interfacial tension between the two phases. This of course assumes that surface viscosity coefficients and gradients of the interfacial tension are negligibly small (68). The normal stress component Π_{rr} inside the drop then takes the form

$$\Pi_{rr}(r) = \frac{1}{2}\rho\omega^2(R^2-r^2) + \Pi_{rr}'(R) - \frac{\sigma}{R} \tag{2-4-5}$$

For negligible inertial and body force terms, the z component of the equation of motion can be integrated to give

$$\Pi_{zz} = g(r,t) \tag{2-4-6}$$

The form of g(r,t) is restricted by the assumption of extensional flow and the simple fluid assumption of Equation (2-2-1). Since the Cauchy-Green strain tensor for this flow is a function of time only (17)

$$\Pi_{rr} - \Pi_{zz} = h(t) \tag{2-4-7}$$

and
$$g(r,t) = -\frac{1}{2}\rho(\omega r)^2 + \hat{g}(t) \tag{2-4-8}$$

The function $\hat{g}(t)$ is evaluated from the boundary condition at r=0 and z=±L; i.e.

$$\hat{g}(t) = \Pi_{zz}(0) = \Pi'_{zz}(0) - H\sigma \tag{2-4-9}$$

where H is the curvature at r=0 and z=±L.

From Equations (2-4-6), (2-4-8), and (2-4-9), it follows that:

$$\Pi_{zz} = -\frac{1}{2}\rho(\omega r)^2 + \Pi'_{zz}(0) - H\sigma \tag{2-4-10}$$

The above expressions for the normal stress components become clearly defined in terms of measurable quantities when it is assumed that the fluid surrounding the drop is Newtonian. In this case,

$$\Pi'_{rr}(R) = -\frac{1}{2}\rho'(\omega R)^2 - \eta'_0\dot{\gamma} - P_0 \tag{2-4-11}$$

$$\Pi'_{zz}(0) = 2\eta'_0\dot{\gamma} - P_0 \tag{2-4-12}$$

where η'_0 is the shear viscosity of the Newtonian fluid, and P_0 is the pressure at r=0 outside the drop.

Combination of (2-4-5), (2-4-10), (2-4-11) and (2-4-12) then gives the normal stress difference (in the drop):

$$\Pi_{zz} - \Pi_{rr} = 3\eta'_0\dot{\gamma} + \frac{\sigma}{R}(\alpha + 1 - K) \tag{2-4-13}$$

where $\alpha = \frac{\Delta\rho\omega^2R^3}{2\sigma}$ and $K = HR$.

For steady extension the extensional viscosity is given by

$$\bar{\eta} = 3\eta_o' + \frac{\sigma}{R\dot{\gamma}}\ (\alpha + 1 - K) \tag{2-4-14}$$

when $\bar{\eta} >>> 3\eta_o'$ and $\alpha >> (K-1)$, the above results become:

$$\Pi_{zz} - \Pi_{rr} = \frac{\Delta\rho\omega^2 R^2}{2} \tag{2-4-15}$$

and

$$\bar{\eta} = \frac{\Delta\rho\omega^2 R^2}{2\dot{\gamma}} \tag{2-4-16}$$

The last four equations are the key expressions in the elongating drop method.

CHAPTER III

THE DROP ELONGATION APPARATUS

3-1. Type of Instrument Needed

A relatively crude rotating drop apparatus was built in a previous study (8). Uncontrolled extension experiments where the extensional stress and the extension rate are both functions of time were carried out. However, the use of such data in the evaluation of viscoelastic theories involves quite tedious numerical calculations, and the use of data from uncontrolled experiments is to be avoided if possible. Meaningful extensional flow data can be obtained only through experiments in which either the extension rate or the extensional stress is constant.

For constant extension rate experiments using the elongating drop technique, the diameter of the drop must decrease with time according to $D=D_0 e^{-\frac{1}{2}\dot{\gamma}t}$, and for constant extensional stress experiments, the resulting normal stress difference $\Pi_{zz}-\Pi_{rr}$ must be held constant. If Equation (2-4-15) is applicable, the latter involves holding ωR constant throughout the experiment. To achieve this, it is necessary to have an experimental apparatus which will instantaneously sense the diameter of the drop, compare it with the desired instantaneous diameter (say for the constant extension rate experiment), and then appropriately control the rotational speed.

An apparatus with such characteristics was built in the present work and will be described in the following sections.

3-2. General Description of Apparatus

The drop elongation apparatus is shown schematically in Fig. 3-1. Its primary components are: the rotating cylinder assembly, the control system, and the measurement apparatus.

During a typical experiment, the liquid drop of interest is located in the center of the rotating glass cylinder as shown in Fig. 3-1. The light sensing assembly in the control system produces a thin collimated light source which passes perpendicular through the glass cylinder and the drop, and is picked up on a photomultiplier tube. The drop is made opaque by the addition of a dye. Hence, the larger the diameter of the drop the more interference with the light from the collimated light source, and the smaller the signal (electric current) generated from the photomultiplier tube. This signal from the photomultiplier tube can be related to the drop diameter by two calibrations. These include: (1) calibration in which several different cylindrical rods with known diameters (ranging from 0.34 cm to 1.12 cm) were inserted into the rotating cylinder and observed with a cathetometer; and (2) calibration in which the diameter of a liquid drop was measured both by the cathetometer and the photomultiplier tube under equilibrium conditions (constant speed of rotation and drop not extending). From the calibration data, the electric signal which corresponds to the desired extension rate can be determined and produced by the function generator. For constant extension rate experiments, this will be one of the inputs to the

Figure 3-1 Schematic Diagram of the Drop Elongation Apparatus

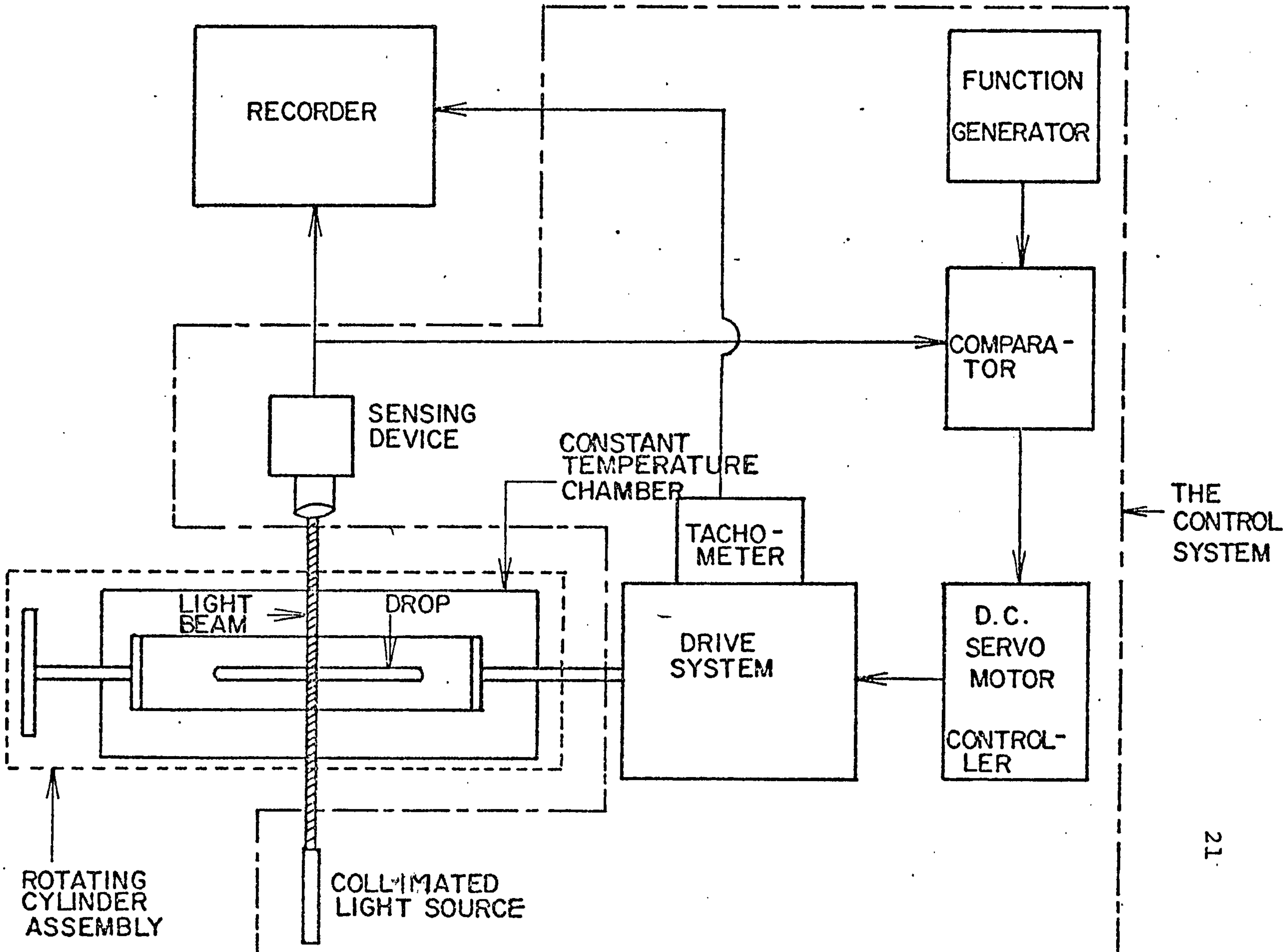

comparator; the other input being from the photomultiplier tube. Through the use of a multiplier, the ω signal from the tachometer along with the D signal from the photomultiplier tube can give a ωD signal. This ωD signal is one of the inputs to the comparator for the constant stress experiments. The other input to the comparator is a constant signal from the function generator. The function of the comparator is to amplify the difference of these two inputs. The controller responds to signal from the comparator and changes the speed of the drive system accordingly. With appropriate control, the difference between the two signals fed into the comparator should be minimized. In that case, based on the signals from the tachometer and from the photomultiplier tube, the extensional flow properties of the drop then can be calculated.

3-3. The Rotating Cylinder Assembly

The rotating cylinder assembly includes a precision glass cylinder, a drop injection system, and a constant temperature chamber. A diagram of the rotating cylinder assembly is shown in Fig. 3-2. The freely rotating glass cylinder is 24" long and 2" I.D. (Wilmad Glass Co., Buena, New Jersey). At each end of the glass cylinder there is a 2" long aluminum end cap. One of the end caps connected to the drive motor is closed. The other end cap is open and has four screw holes designed to fit a head cap. With the bearings on the head cap and the closed end cap, the glass cylinder is mounted in two vertical bearings mounts attached

Figure 3-2 Rotating Cylinder Assembly

1- rotating glass cylinder	2- drop injection system
3- drop	4- temperature sensor
5- heating elements	6- chamber
7- temperature controller	8- double glass window
9- motor	10- hinges

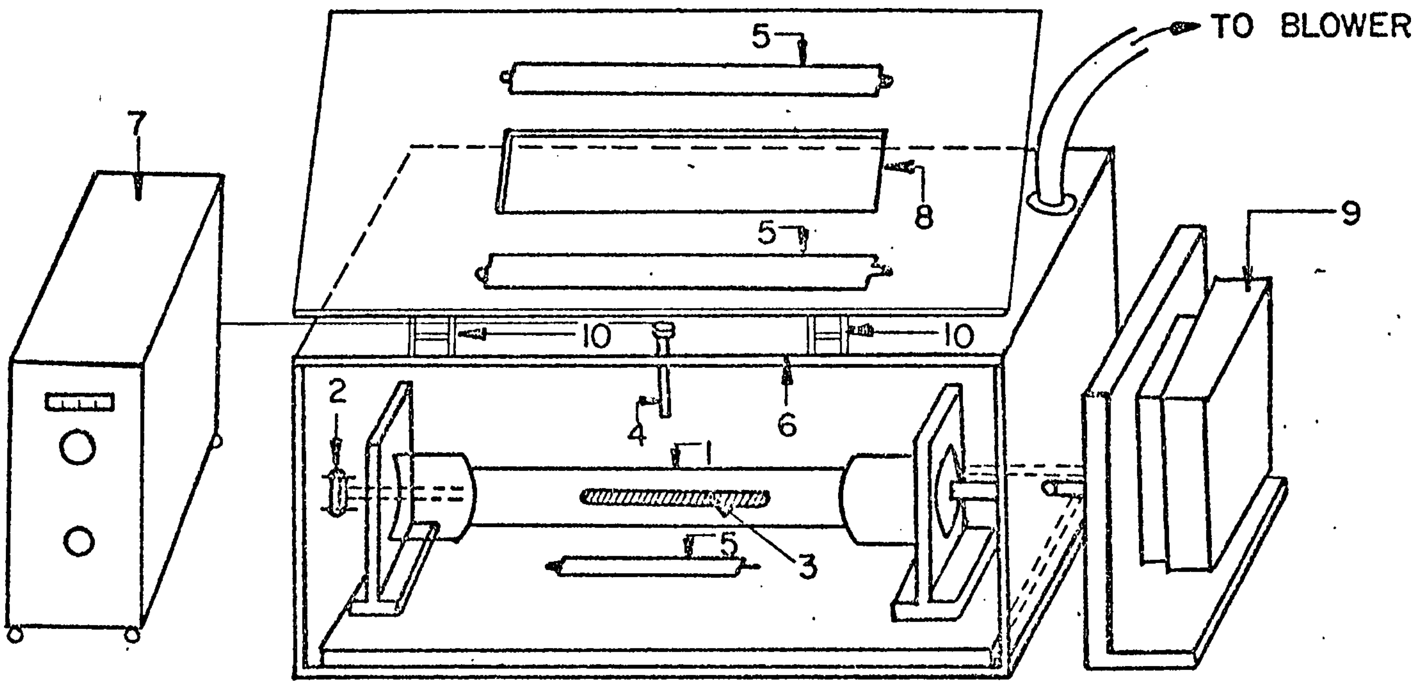

to firm horizontal base. The drop injection system consists of a piston in an injection tube (1/2" I.D., 6 1/8" long). The configuration of the drop injection system along with the head cap is shown in Fig. 3-3. A L-shaped steel wire (the cutter) is mounted on the head cap, and its function is to sever the drop from the injection tube after the drop has been pressed into the cylinder by the piston. The injection tube is made of brass and is fitted into a hole at the center of the head cap with four screws and an O-ring. To eliminate the chance of introducing air bubble into the rotating cylinder, the injection tube remains in place with the glass cylinder after the drop has been injected. In addition, two check valves are designed in the head cap for the continuous phase fluid which is displaced during the injection process.

A (9"x12"x31 1/2") chamber with a temperature control system is used for the purpose of carrying out the drop elongation experiments under constant temperature conditions. The chamber with double glass windows is made of asbestos and has a blower circulation system to eliminate the temperature variation inside the chamber. The temperature controller (controller Model 400, Victory Engineering Co.) with five strip heating elements as heat sources can control the temperature inside the chamber at any desired temperature with the accuracy of $\pm 0.1^{\circ}C$. However, because no cooling source except air is available, the drop elongation experiments can be carried out only at temperatures at or

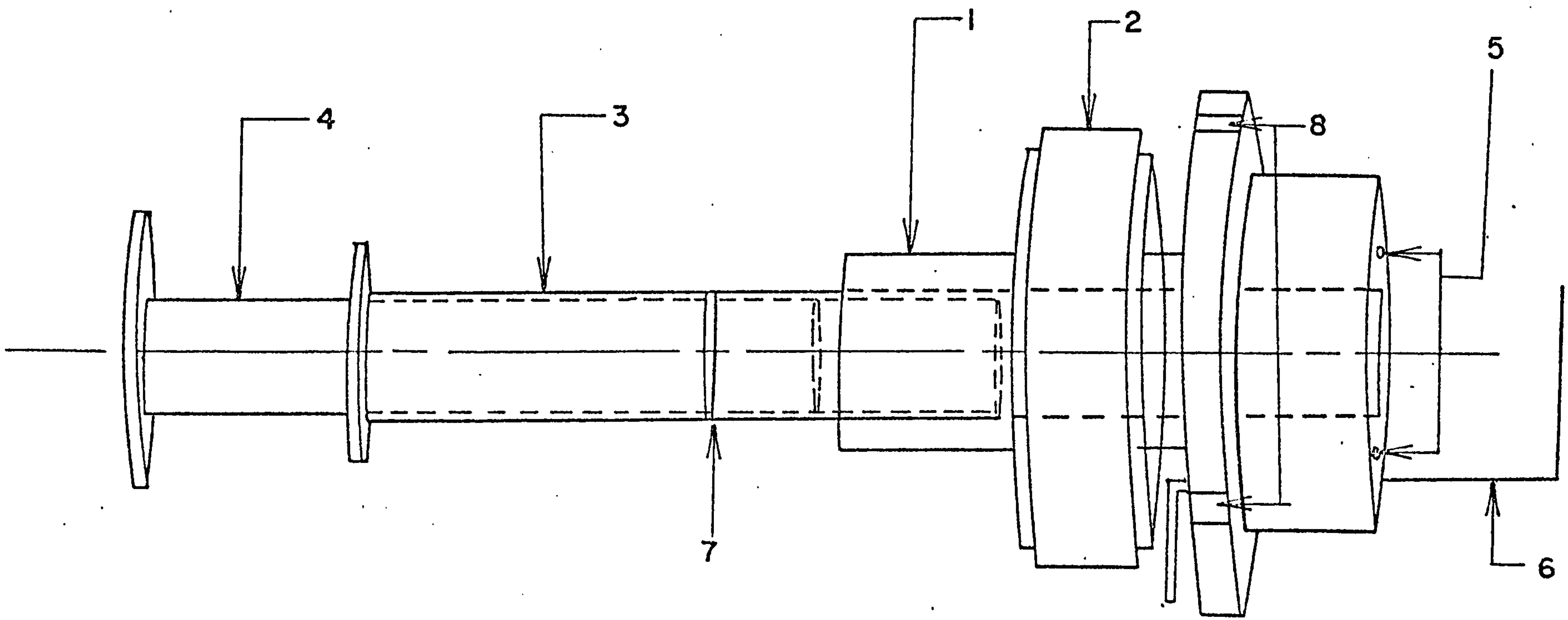

Figure 3-3 Drop Injection System

1- head cap
2- bearings
3- injection tube
4- piston
5- check valve
6- cutter
7- O ring
8- screw hole designed for the head cap to fit into the cylinder

above the room temperature (about 22 ^{o}C).

3-4. The Control System

The control system which includes most of the electronic devices in the drop elongation apparatus consists of a function generator, a light sensing assembly, a servo controller, and a drive system.

3-4-1. The Function Generator

It is well known that a regular potentiometer with its pole connected to a constant dc voltage source will produce a linearly increasing voltage signal when the shaft connected to the wiper is rotated at a constant speed. This is the basic idea behind the function generator built here. The function generator which is made of a +15 volt dc power supply, three potentiometers with different functional characteristics (exponential, linear, and sinusoidal) and a dc stepper motor, can generate signals ranging from 0 to 10 volts of different functions (exponential, linear, and sinusoidal) with respect to time depending on which of the potentiometers is used. The frequency of the sinusoidal function, the $\bar{\xi}$ in the exponential function $e^{\bar{\xi}t}$, and the slope of the linear function are dependent upon the rotational speed level of dc stepper motor. The amplitude of the sinusoidal function and the initial voltage of both the exponential and linear functions are controlled by separate attenuators. Details on the components of the function generator are described in Appendix I.

3-4-2. The Light Sensing Assembly

The light sensing assembly includes a collimated light source and a sensing device. The light source was that from a regular slide projector system. This was followed by a slit arrangement and a ground glass diffuser. A thin (about 1/8") collimated light source was produced with this system. The sensing device has four parts: a focusing lens(Cannon FL 50mm), a diffuser, a photomultiplier tube, and a photomultiplier tube power supply. The focusing lens, the diffuser, and the photomultiplier tube are mounted together on a 3"x$4\frac{1}{2}$"x$6\frac{1}{2}$" aluminum box. The configuration of the box is shown in Fig. 3-4. The functions of each part of the sensing device are as follows:

The focusing lens receives the light passing through the drop and rotating cylinder, and projects it on the diffuser. The color filter in front of the diffuser filters out the wavelengths of light corresponding to the color of the dyed droplet. Hence the light reaching the diffuser is only that which did not intersect the droplet. The photomultiplier tube receives the light passing through the diffuser and generates the corresponding level of electrical output. The amount of electric current generated in the photomultiplier tube also depends on the voltage level imposed by the photomultiplier tube power supply. The higher the voltage level imposed on the photomultiplier tube, the greater the amount of electric current generated. However, it was found that an increase in the voltage level imposed on the

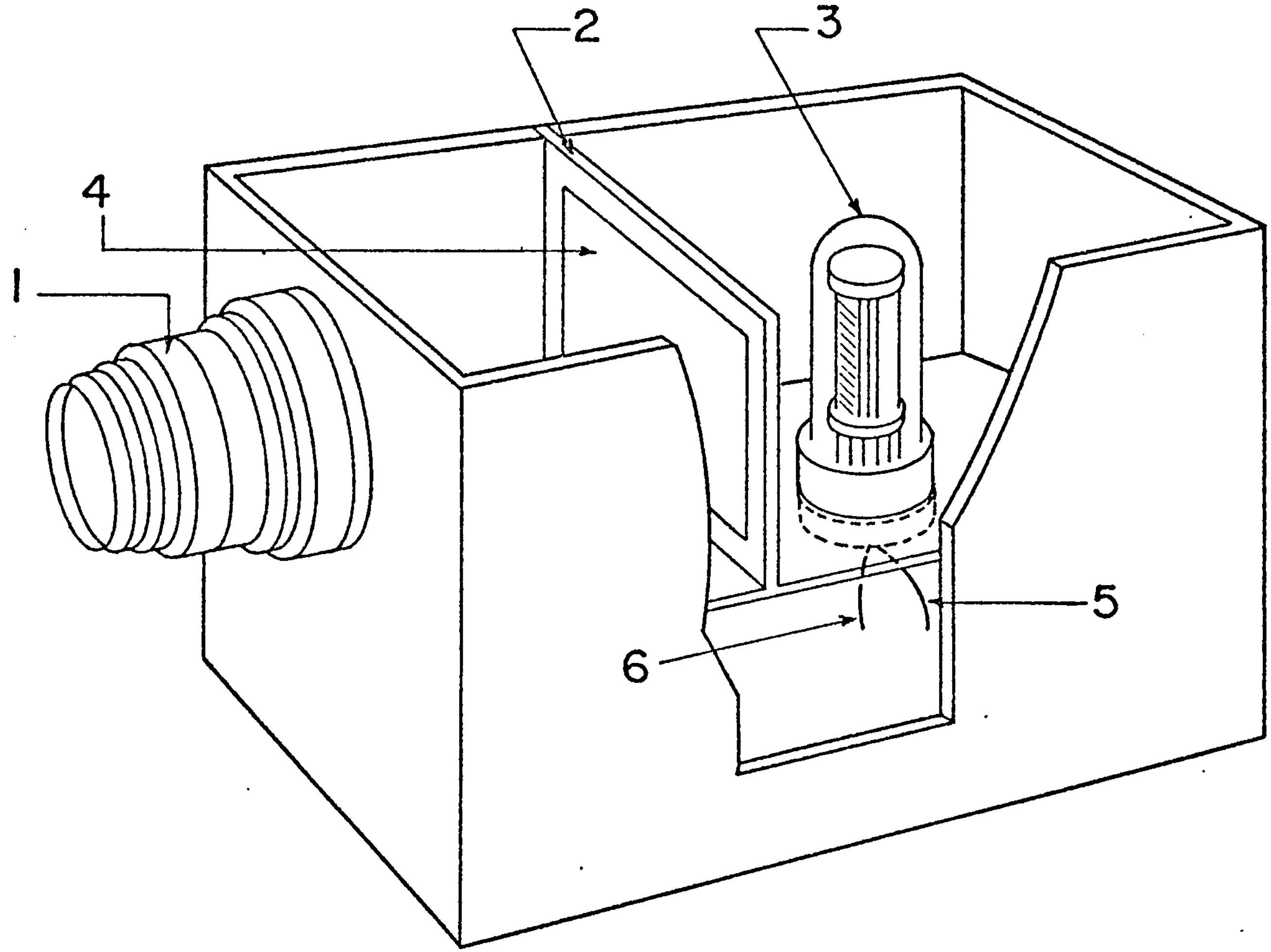

Figure 3-4 Configuration of the Light Sensing Box

1- Cannon Focusing Lens 2- diffuser

3- RCA photomultiplier tube 4- color filter

5- wire connected to the photomultiplier tube power supply

6- output wire of the photomultiplier tube photomultiplier tube will increase the percentage of the noise level in the generated electric current, and in general, will affect the performance of the feedback control system. Thus, in all of the experiments performed, the voltage imposed on the photomultiplier tube was set as low as possible. The geneal characteristics of the photomultiplier tube and the photomultiplier tube power supply can be found in Appendix I.

3-4-3. The Servo Controller

The servo controller used in the drop elongation apparatus is a "proportional" type controller and involves a comparator connected to a dc servo motor controller (Model NC102F, made by Control System Research Inc.). The comparator is basically a variable gain amplifier and its function is to amplify the difference of the two input signals. The output signal of the comparator will be fed into the dc servo motor controller which essentially consists of a preamplifier and a power amplifier. The function of the dc servo motor controller is to impose a proper time dependent voltage on the drive motor so that the rotational speed generated and the corresponding effect on the drop diameter due to the change in the rotational speed will force the two input signals to the comparator to be nearly equal. Details of the dc servo motor controller are described in the Technical Manual of Model NC102 Solid State D.C. Servo Controller.

3-4-4. The Drive System

Micro Switch D.C. Control motor with built-in tachometer (Model No. 6VM-1-C172) is used as a driving system in the drop elongation apparatus. The range of the motor speed can vary from 80 rpm to 5000 rpm. The general characteristics of the motor is listed in Table 3-1. An air cooling system in which a blower blows clean air through the coil inside the motor was attached to reduce the heat generated by the motor at high rotational speed.

Some vibration is generated while the motor rotates. For eliminating the phase difference of the vibration between the drop and the light sensing assembly, the rotating cylinder assembly, the drive motor, and the light sensing assembly were mounted on a $48"\times 50"\times 1\frac{1}{2}"$ aluminum table. With a hydraulic jack, the height of the table is adjustable so that the axial position of the drop inside the glass cylinder can be controlled.

3-5. Measurements of Diameter and Speed

3-5-1. Data Needed and Necessary Calibrations

The behavior of the drop diameter and the corresponding rotational speed during the course of experiment is the basic data required to calculate the extensional flow properties of the liquid drop. The rotational speed is obtained directly from the voltage signal of tachometer using a calibration factor of 2.5 volt/ 1000 RPM. However, because of the optical distortion of the glass cylinder and the inverse nonlinear relationship

Table 3-1 General Characteristics of the Motor

Torque Constant:	11.3 oz-in/amp
Rotor Inertia:	0.00375 oz-in-sec^2
Power Rating:	0.3 kw
Terminal Resistance:	0.42 ohms
Voltage Constant of Tachometer:	2.5 volts/krpm
Voltage Ripple of Tachometer:	1.5% peak to peak (Max)

between the actual diameter (D) and the voltage signal(S_P) of the photomultiplier tube, converting the voltage signal (S_P) of the photomultiplier tube to the actual drop diameter (D) is not as easy as converting the tachometer signal to the rotational speed. Two calibrations are required to relate the actual drop diameter (D) to the voltage signal (S_P) of the photomultiplier tube. These include: (1) calibration in which several different cylindrical rods with known diameters (ranging from 0.34 cm to 1.12 cm) were inserted into the rotating cylinder and observed with a cathetometer; and (2) calibration in which the diameter of a liquid drop was measured both by the cathetometer and the photomultiplier tube under equilibrium condition (constant rotational speed and drop not extending). The purpose of the first calibration was to relate the actual diameter (D) to the visual diameter (S_V), while that of the latter calibration is to relate the visual drop diameter (S_V) to the voltage signal (S_P) of the photomultiplier tube. Combining the results of these calibrations, a quadratic relationship between the actual diameter (D) and the voltage signal of the photomultiplier tube (S_P) was established:

$$S_p = a_1 D^2 + b_1 D + c \qquad (3\text{-}5\text{-}1)$$

where a_1, b_1 and c are constants. The units of S_P and D are volts and cm respectively. After rearranging Equation (3-5-1), we find:

$$S_p = a S_D^2 + b S_D + c \qquad (3\text{-}5\text{-}2)$$

where $S_D = \frac{b_1}{b} D$ and $\frac{b_1^2}{b^2} = \frac{a_1}{a}$.

In both constant extension rate experiments and constant stress experiments, the voltage signal S_D which is quantitatively proportional to the drop diameter (D) was used rather than the voltage signal from the photomultiplier tube S_p. To this end, an analog quadratic inverter with three adjustable potentiometers a,b,and c was built. For a given set of a,b,c, and input S_p, the quadratic inverter is able to produce an output of S_D according to Equation (3-5-2). The procedures of setting values for the potentiometers, as well as the electric diagram of the quadratic inverter are given in Appendix I.

3-5-2. The Measuring Instrument

An Omni Scribe two pen recorder (made by Houston Instrument Co.) is used for recording the output signals from the tachometer and the quadratic inverter. The recorder can record any signal with voltage level ranging from 0.01 volt to 100 volt in five different scales: 0.01 volt, 0.1 volt, 1 volt, 10 volt, and 100 volt. However, depending upon the input voltage level, only certain scales can be used, for example,1 volt, 10 volt and 100 volt scales for signals with voltage >0.5 volt and 100 volt scale for signals with voltage >45 volt, etc. The disadvatage associated with this characteristic of the recorder is that for signals with large absolute voltage level, but relatively small voltage change with respect to time, the recorder is not able to record it with much sensitivity. To correct this, a subtractor is used along with the recorder. The function of the subtractor is to subtract a constant amount of voltage from the recorded input so that the recorder can use the scale with maximum sensitivity to record the input signal. An example of increasing recording sensitivity of the recorder with the help of the subtractor is given as follows: A time dependent signal with voltage changing from 5.8 volt to 4.8 volt in the experiment is the input signal to the recorder. Without the subtractor, the recorder will record this signal in 10 volt scale and the recording sensitivity is about 10% ($\frac{5.8-4.8}{10} \times 100\%$). However, using the subtractor to subtract 4.8 volt from the input signal, the recorder is able to record the signal in 1 volt scale, and in that case, the resulting recording sensitivity is 100% ($\frac{1-0}{1} \times 100\%$).

In addition, depending upon the type of extensional flow experiment, several analog electronic components are used in the experiments, particularly a multiplier for constant extensional stress experiment and a logarithmic amplifier for constant extension rate experiment. Details on those analog electronic circuits are described in Appendix I. An overall view of the drop elongation apparatus is given in Figures 3-5 to 3-9 .

Figure 3-5 Drop Elongation Apparatus

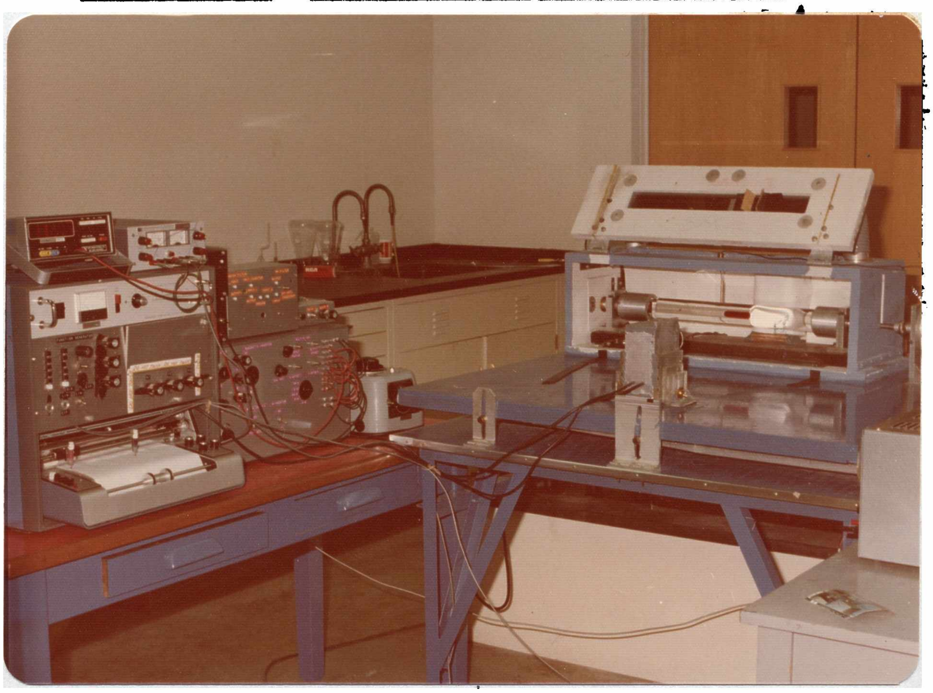

Figure 3-6 Rotating Glass Cylinder

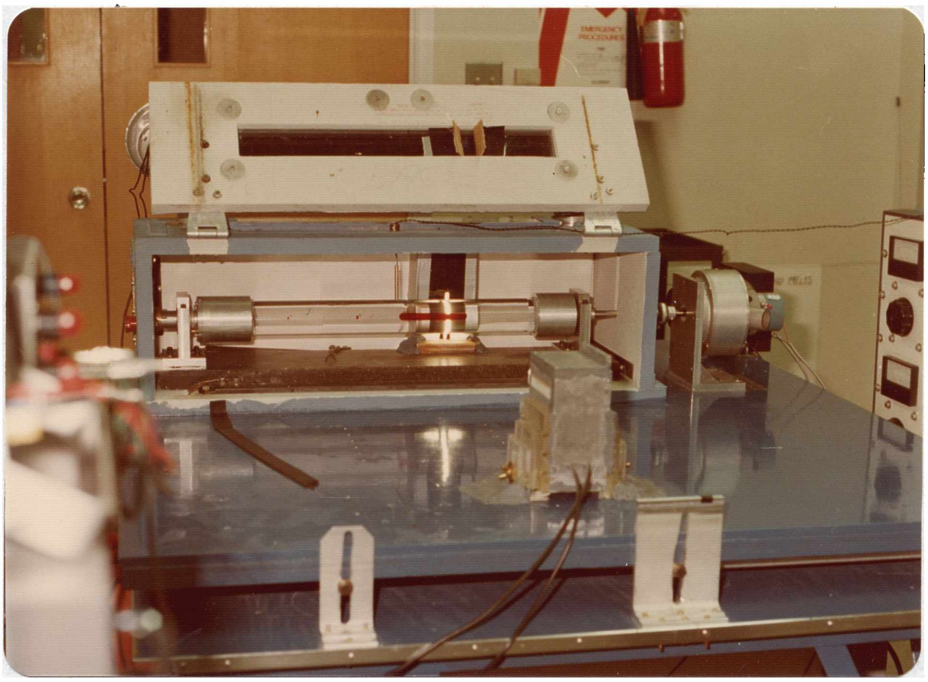

Figure 3-7 The Control System

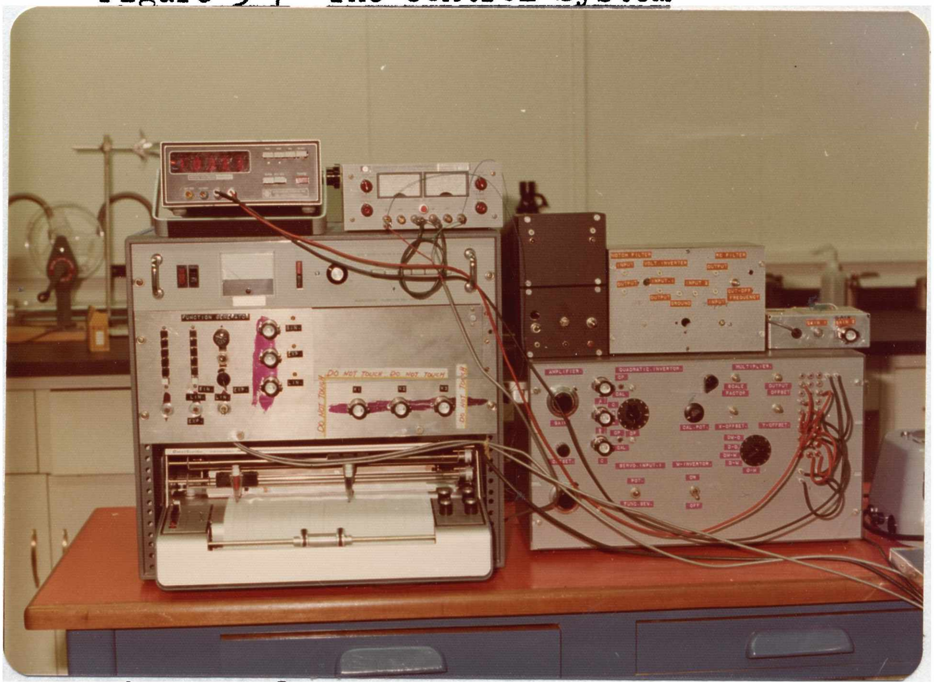

Figure 3-8 The Temperature Controller and the Photomultiplier tube

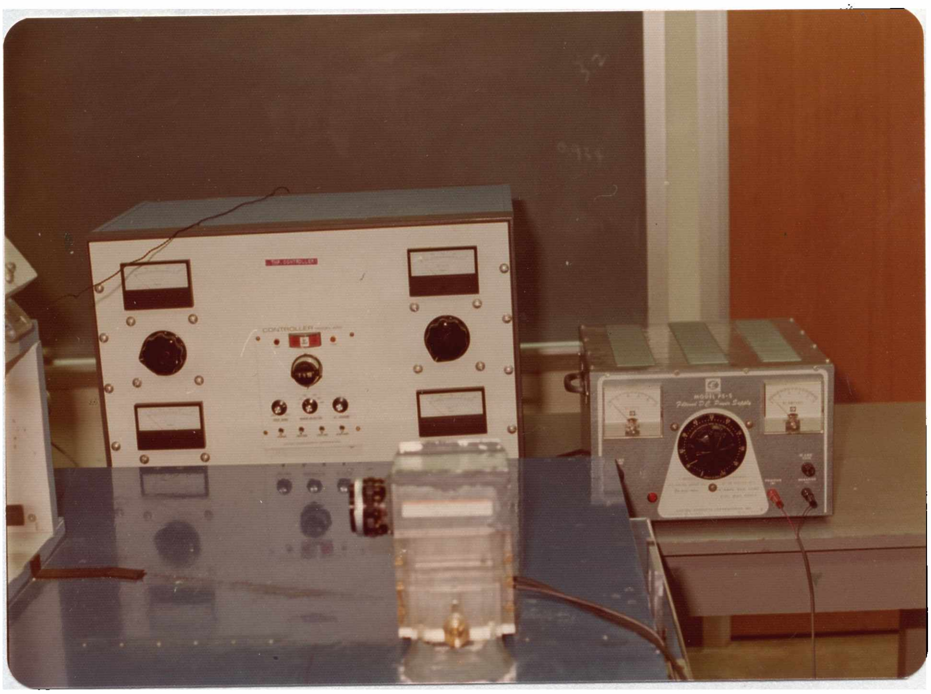

Figure 3-9 The Drive System

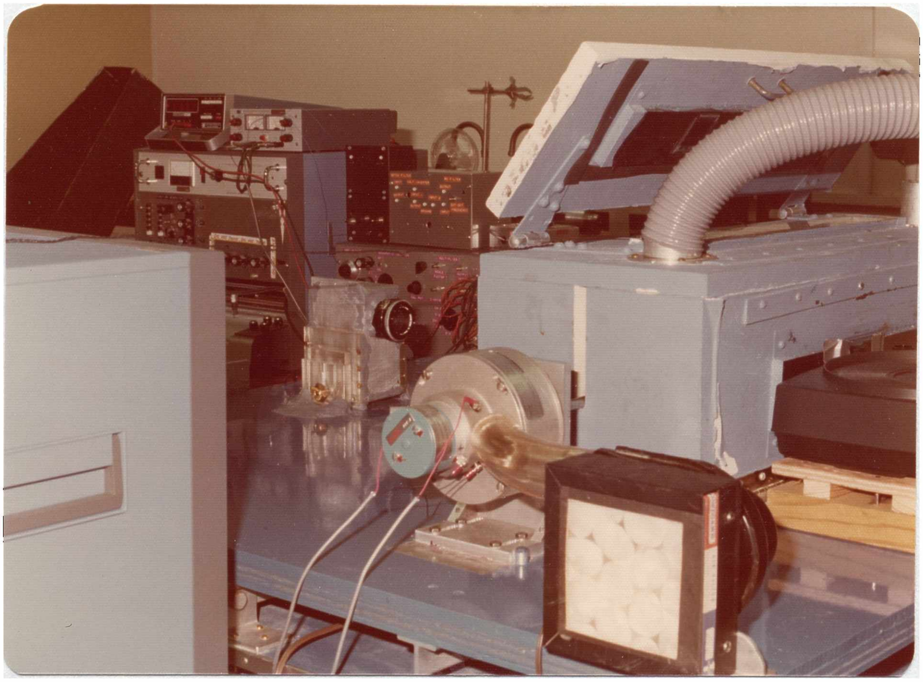

CHAPTER IV

DESIGN OF EXPERIMENTS AND SPECIFICATION OF OPERATING RANGE

4-1. Type of Experiments Possible

With the drop elongation apparatus described previously, both kinematic and stress controlled experiments are possible. The kinematics controlled experiments involve experiments in which the drop diameter D, and the extensional strain (defined as $2\log_e\frac{D(o)}{D(t)}$) vary with time in some prescribed manner. In the stress controlled experiments, a specific extensional stress history is imposed on the drop and the extensional strain $\bar{\gamma}$ is measured. Possible kinematically controlled experiments include stress growth, stress relaxation and oscillatory, while possible stress controlled experiments are creep and recoil. Details on these experiments using the drop elongation apparatus are now described.

(1) Stress growth experiment: This experiment is also termed a "startup experiment". As indicated in Fig. 4-1(a), the experiment is characterized by a step change in extension rate. As a result of this kinematic change, the drop is extended from an equilibrium configuration at a constant extension rate $\dot{\bar{\gamma}}$. The drop diameter and the extensional strain $\bar{\gamma}$ are controlled to change with time in the following manner:

$$\text{when } t<0 \quad D = D_o \quad (\text{equilibrium diameter at } \omega=\omega_o)$$
$$\bar{\gamma} = 0 \tag{4-1-1}$$
$$\text{at } t \geq 0 \quad D = D_o e^{-\frac{1}{2}\dot{\bar{\gamma}}t} \ ; \quad \bar{\gamma} = \dot{\bar{\gamma}}t$$

The stress is determined as a function of time from measurements

Figure 4-1 Kinematics Controlled Experiments

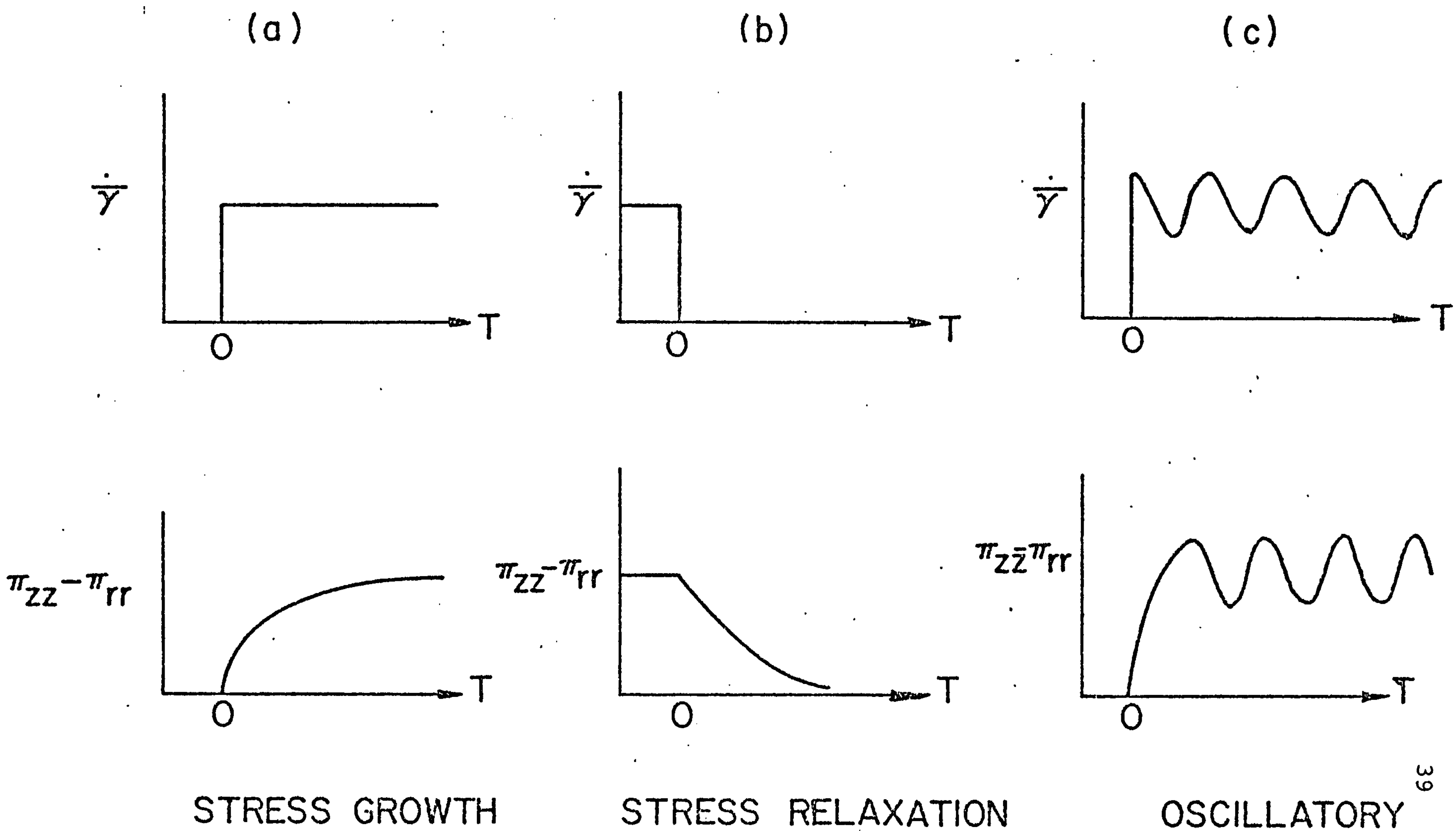

of drop diameter, rotational speed, and use of Equation (2-4-13) or (2-4-15); the equation to be used depends on the conditions and fluids involved.

(2) Stress relaxation experiment: Stress relaxation at a constant extensional strain γ is possible by abruptly ceasing the steady extension which the drop has experienced for a period of time and determining the resulting extensional stress required to maintain the final state of extension. In this case, the time response of the extension rate is given by

$$\begin{aligned} t < 0 \quad & \dot{\gamma} = c \\ t \geq 0 \quad & \dot{\gamma} = 0 \end{aligned} \qquad (4\text{-}1\text{-}2)$$

where c is a constant.

(3) Superimposed oscillatory: This experiment is similar to the common superimposed oscillatory shear experiments carried out in viscometric flows. In the case of extensional flow, small amplitude oscillatory extension is superposed on a constant extension rate by forcing the drop diameter and the extension strain to behave as:

$$D = D_o\, e^{-\frac{1}{2}\left(\dot{\gamma} t + \frac{a_o}{\omega}\sin\omega t\right)}$$

$$\gamma = \dot{\gamma} t + \frac{a_o}{\omega}\sin\omega t \qquad (4\text{-}1\text{-}3)$$

where a_o and ω are the amplitude and frequency of the oscillation respectively, and are restricted by the condition that $\frac{dD}{dt} \leq 0$, or $\dot{\gamma} \geq a_o$.

The latter constraint is necessary in light of the fact that the extension can be controlled only when the drop is extending ; contraction of the drop is a result of uncontrolled interfacial and elastic forces. In this experiment, the corresponding extensional stress is determined from Equation (2-4-13) or (2-4-15), depending on the range of conditions and the fluid systems involved. Typical relations between the extensional stress and the extension rate for stress growth, stress relaxation and superimposed oscillatory are outlined in Fig. 4-1. (a),(b), and(c), respectively.

(4) Creep: Complementary to the condition of a constant extension rate $\dot{\gamma}$ is the condition of a constant extensional stress which defines the creep experiment. The condition $\Pi_{zz} - \Pi_{rr}$ = constant is maintained throughout the course of experiment. If Equation (2-4-15) is applicable, this is equivalent to holding ωR constant. Once the condition of constant extensional stress is fulfilled, both the time-dependent drop diameter and extensional strain are monitored and measured.

(5) Recoil: The final possible stress controlled experiment is recoil, termed by Lodge (20) as instantaneous recovery from steady extensional flow. In this experiment, the whole rotating system is instantaneously braked to a rotational speed just sufficient to keep the drop in the center of the glass cylinder. The subsequent behavior of the drop diameter and the extensional strain due to the resulting contraction are measured as a function of time. This experiment is possible only if the elastic stresses causing the contraction are much greater than the interfacial forces.

Typical relations between the extensional stress and the extension rate for creep and recoil are shown in Fig.4-2(a) and (b) respectively.

It should be noted that in addition to the transient extensional flow data, the extensional viscosity can be obatined from the steady state data of stress growth and creep experiments. The drop is extended at a constant extension rate (or constant extensional stress) until the initial startup effect diminishes and the resulting extensional stress (or extension rate) reaches a constant value. Equation (2-4-14) or (2-4-16) is used, depending upon the operating conditions and the physical properties of fluids involved.

All the experiments except the superimposed oscillatory are tested in the drop elongation apparatus with a Newtonian silicone oil. The experimental feasibilities along with the difficulties associated for each experiment are discussed in Section 4-4.

4-2. Correction for Interfacial Tension Effects

The use of Equation (2-4-13) and (2-4-14) requires the knowledge of the curvature at $r=0$, $z=\pm L$ (that is, K is required). To this end, two analyses have been carried out to obtain this information: an analytical approximation and a numerical analysis. In the former, an expression for the drop shape during extension

Figure 4-2 Stress Controlled Experiments

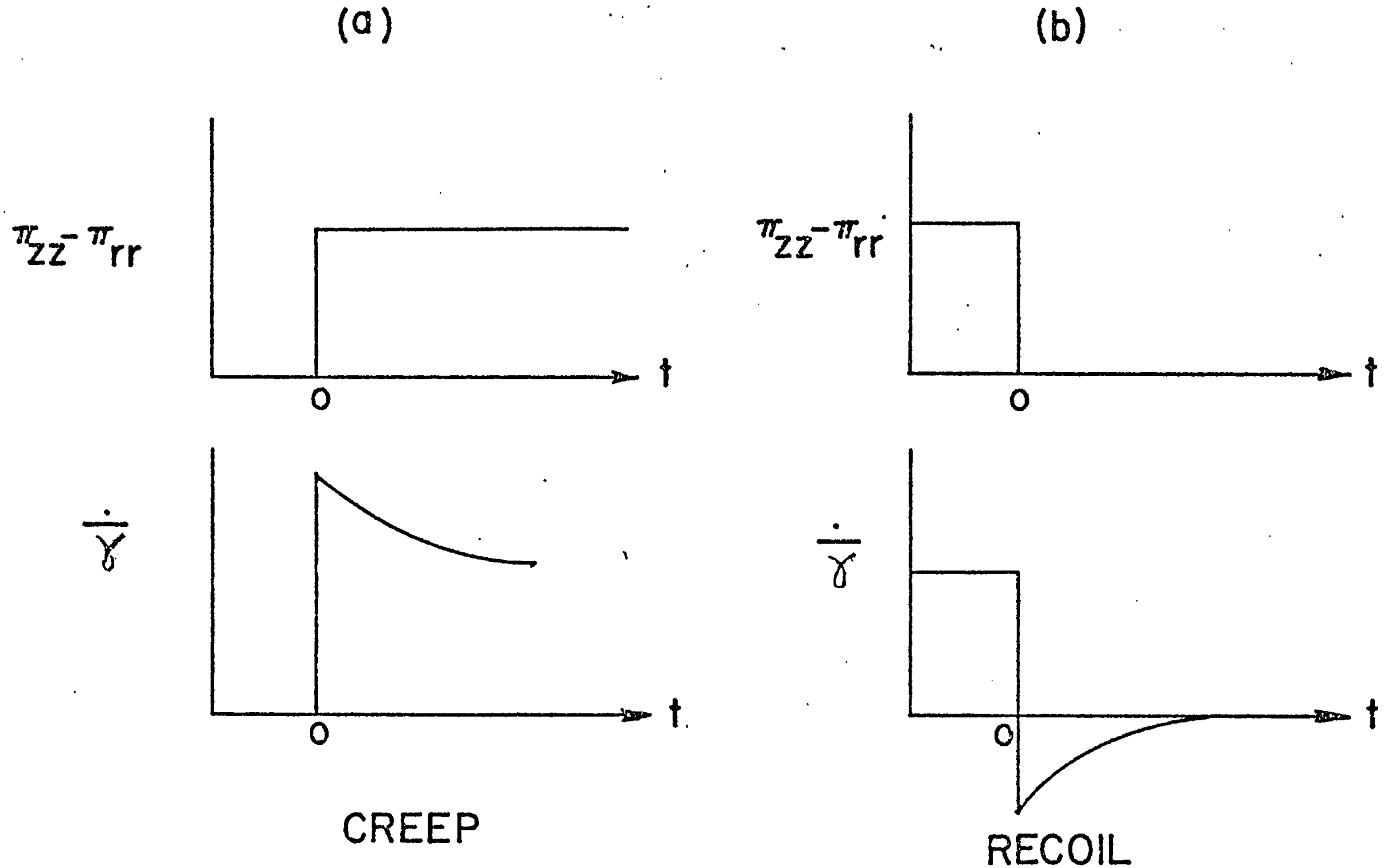

is obtained (and therefore K) by assuming the liquid particles near $r=0$, $z=\pm L$ experience uniaxial extensional flow. In the numerical analysis, the quasisteady state drop elongation phenomena is simulated using approximate methods such as least square and orthogonal collocation. Details on these two analyses are presented in this section. This is followed by a comparison with experimental results.

4-2-1. Analytical Estimation of K

When a fluid drop is placed in a liquid of high density contained in a rotating horizontal cylinder, the drop becomes elongated along the axis of rotation until an equilibrium configuration of the drop is reached which results from the balancing of the centrifugal and interfacial forces. The equilibrium shape of the drop is described elsewhere (11).

A diagram of the system considered here is shown in Fig. 4-3. Cylindrical coordinates (r, z) are chosen with origin at the left hand end of the drop. The semiaxes are z_0 and r_0 ; the densities of the drop and the outer phase are ρ_1 and ρ_2 ($\rho_2 > \rho_1$) and the interfacial tension is σ. For the system rotating at constant speed ω , the equilibrium shape of the drop is given as

$$z = \int_0^r \frac{\frac{H_0 \eta}{2} - \frac{\alpha' \eta^3}{4}}{\left[1 - \left(\frac{H_0 \eta}{2} - \frac{\alpha' \eta^3}{4}\right)^2\right]^{1/2}} \, d\eta \qquad (4\text{-}2\text{-}1)$$

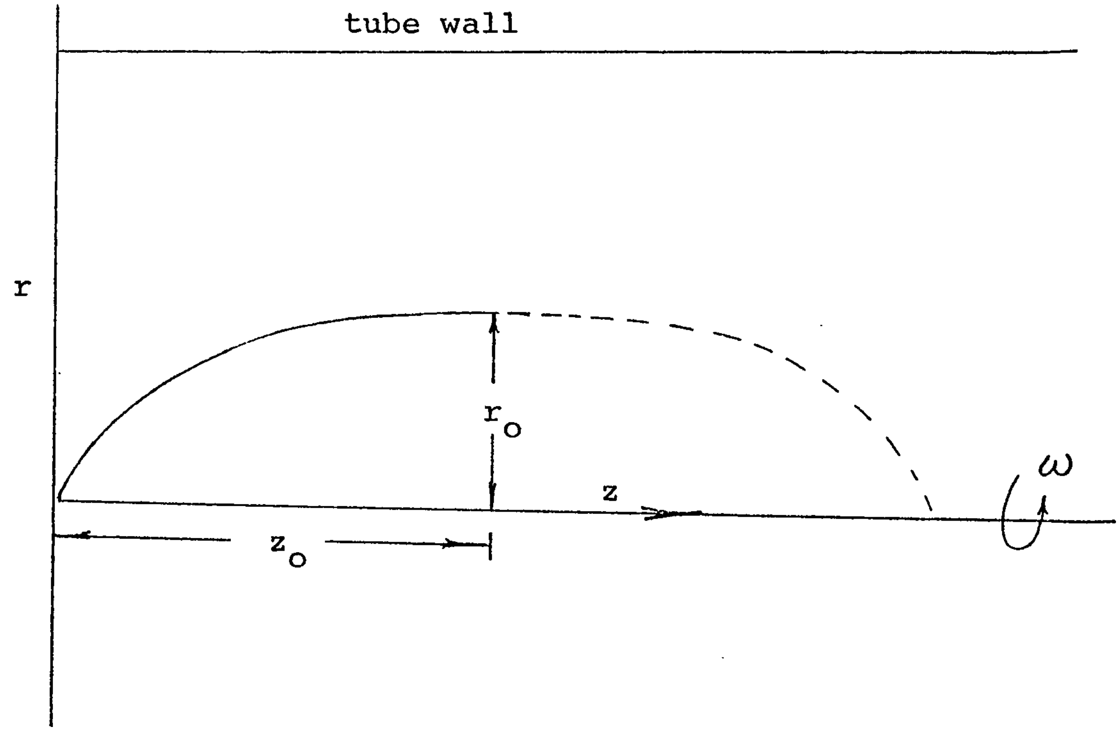

Figure 4-3 Coordinate System to Describe the Shape of a Drop Rotating about a Horizontal Axis

where H_0 is the curvature of the drop phase at the origin and α' is defined as $\frac{(\rho_2-\rho_1)\omega^2}{2\sigma}$. By making the assumption that the liquid particles at the end of the drop surface experience uniaxial extensional flow, then a liquid particle at the end of the drop surface occupying the coordinate (r,z) at t=0 will find itself at the place $(\bar{r},\bar{z})$ at time t, with (r,z) and $(\bar{r},\bar{z})$ connected by

$$\bar{z} = z_0 - (z_0 - z)\, e^{\int_0^t \dot{\gamma}(t')dt'}$$
$$\bar{r} = r\, e^{-\frac{1}{2}\int_0^t \dot{\gamma}(t')dt'} \qquad (4\text{-}2\text{-}2)$$

where $\dot{\gamma}(t)$ is the extension rate at time t. Combination of Equation (4-2-1) and (4-2-2) gives the drop shape in the neighborhood of $\bar{z}=0$ and $2\bar{z}_0$, at time t:

$$\bar{z} = z_0\left(1 - e^{\int_0^t \dot{\gamma}(t')dt'}\right) + e^{\int_0^t \dot{\gamma}(t')dt'} \int_0^{\bar{r}\, e^{\frac{1}{2}\int_0^t \dot{\gamma}(t')dt'}} \frac{\frac{H_0\eta}{2} - \frac{\alpha'\eta^3}{4}}{\left[1 - \left(\frac{H_0\eta}{2} - \frac{\alpha'\eta^3}{4}\right)^2\right]^{1/2}}\, d\eta \qquad (4\text{-}2\text{-}3)$$

The curvature of the drop surface $\bar{H}$ is calculated by

$$\bar{H} = \frac{1}{R_1} + \frac{1}{R_2} \qquad (4\text{-}2\text{-}4)$$

where $\frac{1}{R_1}$ and $\frac{1}{R_2}$ are the principal curvatures and defined as

$$\frac{1}{R_1} = \frac{\frac{d^2\bar{z}}{d\bar{r}^2}}{\left(1+\left(\frac{d\bar{z}}{d\bar{r}}\right)^2\right)^{3/2}} \quad ; \quad \frac{1}{R_2} = \frac{\frac{d\bar{z}}{d\bar{r}}}{\bar{r}\left(1+\left(\frac{d\bar{z}}{d\bar{r}}\right)^2\right)^{1/2}} \qquad (4\text{-}2\text{-}5)$$

Substituting Equation (4-2-3) into Equation (4-2-4) and (4-2-5), the curvature at $\bar{r}=0$ is

$$H = H_0\, e^{2\int_0^t \dot{\gamma}(t')dt'} \qquad (4\text{-}2\text{-}6)$$

Since the dimensionless curvature is defined as

$$K = \bar{r}_0 H = H r_0\, e^{-\frac{1}{2}\int_0^t \dot{\gamma}(t')dt'} \qquad (4\text{-}2\text{-}7)$$

Combination of Equation (4-2-7) and (4-2-6) yields

$$K = K\Big|_{t=0}\, e^{\frac{3}{2}\int_0^t \dot{\gamma}(t')dt'} \qquad (4\text{-}2\text{-}8)$$

If the drop is extended from an equilibrium configuration with large $\frac{z_0}{r_0}$, then the value for $K\big|_{t=0}$ is $K\big|_{t=0} = 3$ (4-2-9)

and it follows that

$$K = 3\, e^{1.5\,\bar{\gamma}} \qquad (4\text{-}2\text{-}10)$$

where $\bar{\gamma}(t)$, the extensional strain, is equal to $\int_0^t \dot{\gamma}(t')dt'$.

Equation (4-2-10) allows the estimation of K for any given $\bar{\gamma}$ during the course of the drop elongation experiment.

4-2-2. Numerical Prediction of K

The dynamics of the drop elongation phenomena, particularly, the resulting shape, internal flow patterns, etc., are analyzed here.

Formulation

Consider a system in which a Newtonian liquid drop with density ρ and viscosity μ is suspended in another Newtonian continuous phase liquid with density ρ' and viscosity μ', all contained in a horizontal rotating cylinder. Initially the whole system (drop+ continuous phase + cylinder) is rotating around the axis of the cylinder at a constant speed ω_0 and the drop configuration is that associated with equilibrium, i.e., the drop shape is described by Equation (4-2-1). At t=0, a special history of rotational speed $\omega(t)$ is applied to the whole system.

We wish to describe the resulting dynamics of the drop caused by these changes in $\omega(t)$.

A spherical coordinate system $(\bar{r},\theta,\phi)$ is used (Fig. 4-4) and the response of this system is analyzed subject to the following assumptions:

(1) The rate of deformation of the drop is sufficiently small that the transient behavior of the drop elongation phenomena can be treated as quasisteady state (Reynolds numder,RE = $1.0 \times 10^{-3} \ll 1$).

(2) The drop particles at the center of the drop ($\theta = 90^\circ$) experience extensional flow.

(3) The viscosity of the continuous phase is small compared to that of the drop and hence, on the drop surface the extra stress components of the continuous phase are negligible compared to those of the drop phase.

(4) The whole system rotates in a rigid body manner.

If inertial effects other than the centrifugal force term are neglected, as well as the body force terms, the $\bar{r}$ and θ components of equation of motion for the drop phase can be reduced to

$$-\rho\frac{\bar{V}_\phi^2}{\bar{r}} = -\frac{\partial\bar{p}}{\partial\bar{r}} + \mu\left(\bar{\nabla}^2\bar{V}_r - \frac{2}{\bar{r}^2}\frac{\partial\bar{V}_\theta}{\partial\theta} - \frac{2}{\bar{r}^2}\bar{V}_\theta\cot\theta\right) \tag{4-2-11}$$

and $$-\rho\frac{\bar{V}_\phi^2\cot\theta}{\bar{r}} = -\frac{1}{\bar{r}}\frac{\partial\bar{p}}{\partial\theta} + \mu\left(\bar{\nabla}^2\bar{V}_\theta + \frac{2}{\bar{r}^2}\frac{\partial\bar{V}_r}{\partial\theta} - \frac{\bar{V}_\theta}{\bar{r}^2\sin^2\theta}\right)$$

where $\bar{V}_\phi = \bar{r}\sin\theta\,\omega$, $\bar{\nabla}^2 = \frac{1}{\bar{r}^2}\frac{\partial}{\partial\bar{r}}\left(\bar{r}^2\frac{\partial}{\partial\bar{r}}\right) + \frac{1}{\bar{r}^2\sin\theta}\frac{\partial}{\partial\theta}\left(\sin\theta\frac{\partial}{\partial\theta}\right)$ and ω is the rotational speed.

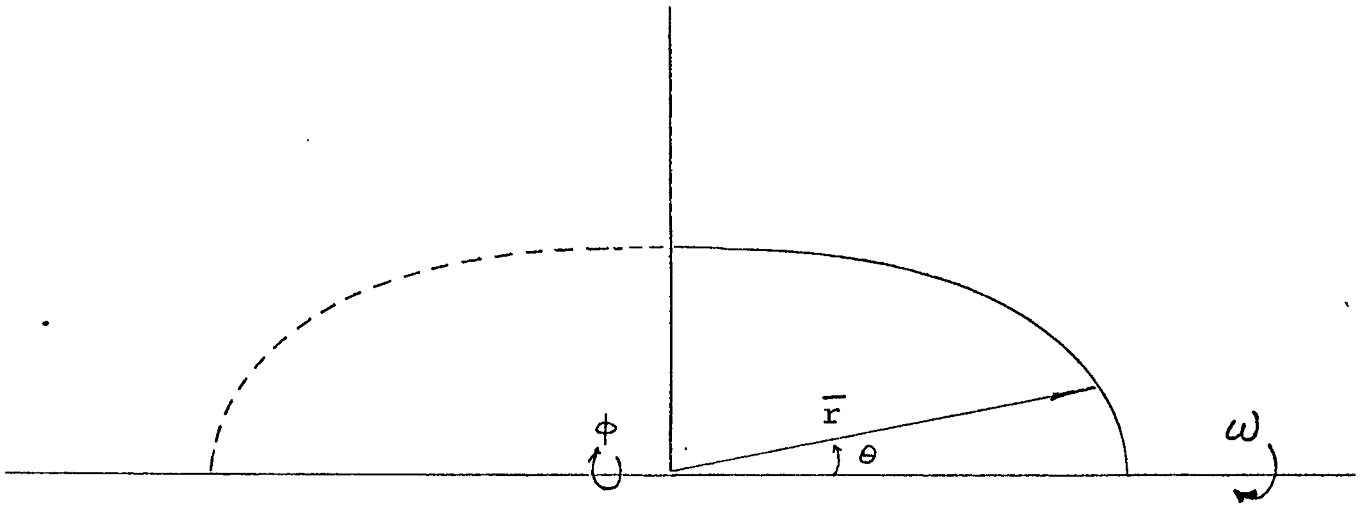

Figure 4-4 Coordinate System Used in the Numerical Simulation of the Drop Elongation Phenomena.

The equations are nondimensionalized by using the initial drop radius R_o at $\theta=90^\circ$, the initial rotational speed ω_o, the viscosity of the drop phase μ, and the density difference, $\Delta\rho=\rho'-\rho$, between the two phases as follows.

Let $r^*=\frac{\bar{r}}{R_o}$, $V_r^*=\frac{\bar{V}_r}{R_o\omega_o}$, $V_\theta^*=\frac{\bar{V}_\theta}{R_o\omega_o}$, $P^*=\frac{\bar{P}}{\Delta\rho\,\omega_o^2R_o^2}$, $S=\frac{\omega}{\omega_o}$,

$$RE=\frac{\Delta\rho R_o^2\omega_o}{\mu}, \quad \text{and} \quad G=\frac{\rho'}{\rho} \tag{4-2-12}$$

then Equation (4-2-11) becomes

$$-\frac{r^*\sin^2\theta\, S^2}{G-1}=-\frac{\partial P^*}{\partial r^*}+\frac{1}{RE}\left(\nabla^2V_r^*-\frac{2}{r^{*2}}V_r^*-\frac{2}{r^{*2}}V_\theta^*\cot\theta\right)$$

and

$$-\frac{r^*\sin^2\theta\cot\theta\, S^2}{G-1}=-\frac{1}{r^*}\frac{\partial P^*}{\partial\theta}+\frac{1}{RE}\left(\nabla^2V_\theta^*+\frac{2}{r^{*2}}\frac{\partial V_r^*}{\partial\theta}-\frac{V_\theta^*}{r^{*2}\sin^2\theta}\right) \tag{4-2-13}$$

where $$\nabla^2=\frac{1}{r^{*2}}\frac{\partial}{\partial r^*}\left(r^{*2}\frac{\partial}{\partial r^*}\right)+\frac{1}{r^{*2}\sin\theta}\frac{\partial}{\partial\theta}\left(\sin\theta\frac{\partial}{\partial\theta}\right)$$

In the present case of axisymmetric flow, Equation (4-2-13) leads to a fourth-order partial differential equation for the stream function:

$$E^4\psi=0 \tag{4-2-14}$$

In spherical coordinate, $E^4=\left(\frac{\partial^2}{\partial r^{*2}}+\frac{1-\hat{\eta}^2}{r^{*2}}\frac{\partial^2}{\partial\hat{\eta}^2}\right)^2$ where $\hat{\eta}=\cos\theta$ and the velocity components are given by

$$V_r^*=-\frac{1}{r^{*2}\sin\theta}\frac{\partial\psi}{\partial\theta}, \quad V_\theta^*=\frac{1}{r^*\sin\theta}\frac{\partial\psi}{\partial r^*} \tag{4-2-15}$$

by which the equation of continuity is satisfied automatically.

The dimensionless boundary conditions on the drop surface for a quasisteady state solution are

$$\Pi_{n\bar{t}}^*=\Pi_{n\bar{t}}^{*\prime}$$

$$\text{and} \quad \Pi_{nn}^*=\Pi_{nn}^{*\prime}+\hat{\sigma}\bar{K} \tag{4-2-16}$$

where Π_{ij}^* and $\Pi_{ij}^{*\prime}$ are the components of the total stress tensor of the drop and the continuous phase respectively, n is the direction normal to the drop surface, $\bar{t}$ is the direction tangential to the drop surface in a meridional plane, $\bar{K}$ is the dimensionless mean curvature, expressed by

$$\bar{K} = R_o \bar{H} = R_o \left(\frac{1}{R_1} + \frac{1}{R_2} \right) \qquad (4\text{-}2\text{-}17)$$

where R_1 and R_2 are the principal radii of curvature. Finally, $\hat{\sigma}$ is a dimensionless interfacial tension

$$\hat{\sigma} = \frac{\sigma}{(\rho' - \rho) R_o^3 \omega_o^2} \qquad (4\text{-}2\text{-}18)$$

Substituting the relation $\Pi^*_{ij} = -p^* \delta_{ij} - \tau^*_{ij}$ into Equation (4-2-16), the boundary conditions can be expressed in terms of components of the extra stress tensor $\underset{\sim}{\tau}^*$ refered to spherical coordinates through the transformation equations.

$$((\tau^*_{\theta\theta} - \tau^{*\prime}_{\theta\theta}) - (\tau^*_{rr} - \tau^{*\prime}_{rr})) \sin\hat{\alpha} \cos\hat{\alpha} + (\tau^*_{r\theta} - \tau^{*\prime}_{r\theta})(\cos^2\hat{\alpha} - \sin^2\hat{\alpha}) = 0$$

$$(4\text{-}2\text{-}19)$$

$$(p^{*\prime} - p^*) - (\tau^*_{rr} - \tau^{*\prime}_{rr}) \cos^2\hat{\alpha} - (\tau^*_{\theta\theta} - \tau^{*\prime}_{\theta\theta}) \sin^2\hat{\alpha} - (\tau^*_{r\theta} - \tau^{*\prime}_{r\theta}) \sin 2\hat{\alpha} + \hat{\sigma} \bar{K} = 0$$

If the surface of the drop enclosing the origin is described by specifying the radius as a function $\bar{R}(\theta)$, then

$$\hat{\alpha} = \tan^{-1}\left(-\frac{1}{\bar{R}} \frac{d\bar{R}}{d\theta} \right) = \tan^{-1}\left(-\frac{1}{R_D} \frac{dR_D}{d\theta} \right) \qquad (4\text{-}2\text{-}20)$$

where $R_D(\theta) = \dfrac{\bar{R}(\theta)}{R_o}$.

In terms of $R_D(\theta)$ the expression for $\bar{K}$ becomes

$$\bar{K} = \frac{\left[2 + 2\left(\frac{1}{R_D} \frac{dR_D}{d\theta} \right)^2 - \frac{d}{d\theta}\left(\frac{1}{R_D} \frac{dR_D}{d\theta} \right) - \left(\frac{1}{R_D} \frac{dR_D}{d\theta} + \left(\frac{1}{R_D} \frac{dR_D}{d\theta} \right)^3 \right) \cot\theta \right]}{R_D \left(1 + \left(\frac{1}{R_D} \frac{dR_D}{d\theta} \right)^2 \right)^{3/2}} \qquad (4\text{-}2\text{-}21)$$

Using the assumption (3), $\tau^{*\prime}_{ij} \lll \tau^*_{ij}$, Equation (4-2-19) can be simplified to

$$(\tau^*_{\theta\theta} - \tau^*_{rr}) \sin\hat{\alpha} \cos\hat{\alpha} + \tau^*_{r\theta} (\cos^2\hat{\alpha} - \sin^2\hat{\alpha}) = 0 \qquad (4\text{-}2\text{-}22(a))$$

$$(p^{*\prime} - p^*) - \tau^*_{rr} \cos^2\hat{\alpha} - \tau^*_{\theta\theta} \sin^2\hat{\alpha} - 2\tau^*_{r\theta} \sin\hat{\alpha} \cos\hat{\alpha} + \hat{\sigma}\bar{K} = 0 \qquad (4\text{-}2\text{-}22(b))$$

Solution

The general solution of equation (4-2-14) is given elsewhere (75)

$$\psi=\sum_{m=1}^{\infty}\left(A_m r^{*\,m+3}+B_m r^{*\,-m+2}+C_m r^{*\,m+1}+D_m r^{*\,-m}\right)\bar{P}_m(\hat{\eta}) \qquad (4\text{-}2\text{-}23)$$

where $\bar{P}_m(\hat{\eta})=\int_{-1}^{\hat{\eta}} P_m(\eta')\,d\eta'$, $P_m(\hat{\eta})$ is the Legendre Polynomial of degree m, and A_m, B_m, C_m, and D_m are arbitrary constants.

Combination of equation (4-2-23) and (4-2-15) gives the velocity components

$$V_r^*=-\sum_{m=1}^{\infty}\left(A_m r^{*\,m+1}+B_m r^{*\,-m}+C_m r^{*\,m-1}+D_m r^{*\,-m-2}\right)P_m(\hat{\eta})$$

and

$$V_\theta^*=\frac{-\sum_{m=1}^{\infty}\left(A_m(m+3)r^{*\,m+1}+(-m+2)B_m r^{*\,-m}+C_m(m+1)r^{*\,m-1}-m\,D_m r^{*\,-m-2}\right)\bar{P}_m(\hat{\eta})}{(1-\hat{\eta}^2)^{1/2}} \qquad (4\text{-}2\text{-}24)$$

Due to the finiteness condition of V_r^* and V_θ^* as r^*goes to zero and the symmetry requirement that $V_r^*(r^*,\hat{\eta})=V_r^*(r^*,-\hat{\eta})$, Equation (4-2-24) is reduced to

$$V_r^*=-\sum_{m=2,4,6..}^{\infty}\left(A_m r^{*\,m+1}+C_m r^{*\,m-1}\right)P_m(\hat{\eta})$$

and

$$V_\theta^*=\frac{-\sum_{m=2,4,6,\cdots}^{\infty}\left(A_m(m+3)r^{*\,m+1}+C_m(m+1)r^{*\,m-1}\right)\bar{P}_m(\hat{\eta})}{(1-\hat{\eta}^2)^{1/2}} \qquad (4\text{-}2\text{-}25)$$

After rearranging Equation (4-2-25), it follows that

$$V_r^*=-C_2P_2(\hat{\eta})r^*-\sum_{m=2,4,6,..}^{\infty}\left(A_mP_m(\hat{\eta})+C_{m+2}P_{m+2}(\hat{\eta})\right)r^{*\,m+1}$$

and

$$V_\theta^*=-\frac{3C_2r^*\bar{P}_2(\hat{\eta})}{(1-\hat{\eta}^2)^{1/2}}-\frac{\sum_{m=2,4,6,..}^{\infty}\left(A_m(m+3)\bar{P}_m(\hat{\eta})+C_{m+2}(m+3)\bar{P}_{m+2}(\hat{\eta})\right)r^{*\,m+1}}{(1-\hat{\eta}^2)^{1/2}} \qquad (4\text{-}2\text{-}26)$$

From the assumption (2) that at $\theta=90^\circ$ ($\hat{\eta}=0$), $\bar{V}_r=-\frac{\dot{\gamma}(t)\bar{r}}{2}$, where $\dot{\gamma}(t)$ is the instantaneous extension rate, the following relations among the coefficients can be obtained

$$A_m=\frac{(m+1)}{(m+2)}C_{m+2}\ ,\ C_2=-\dot{\gamma}(t)/\omega_o \quad m=2,4,6,\cdots \qquad (4\text{-}2\text{-}27)$$

and Equation (4-2-26) is further simplified to

$$V_r^* = -C_2 P_2(\hat{\eta}) r^* - \sum_{m=2,4,6..}^{\infty} C_{m+2} \left(\frac{m+1}{m+2} P_m(\hat{\eta}) + P_{m+2}(\hat{\eta}) \right) r^{*m+1}$$

and

$$V_\theta^* = -\frac{3 C_2 r^* \bar{P}_2(\hat{\eta})}{(1-\hat{\eta}^2)^{1/2}} - \sum_{m=2,4,6,..}^{\infty} \left(\frac{m+1}{m+2} \bar{P}_m(\hat{\eta}) + \bar{P}_{m+2}(\hat{\eta}) \right) \frac{(m+3) C_{m+2} r^{*m+1}}{(1-\hat{\eta}^2)^{1/2}} \quad (4\text{-}2\text{-}28)$$

Substituting Equation (4-2-28) into (4-2-13), the dimensionless pressure inside the drop is obtained as

$$P^* = \frac{r^{*2}(1-\hat{\eta}^2)s^2}{2(G-1)} + \frac{1}{RE} \sum_{m=2,4,6,..}^{\infty} \frac{(4m+6)(m+1)}{m(m+2)} C_{m+2} \left(R_e^m - P_m(\hat{\eta}) r^{*m} \right) + P_o^* \quad (4\text{-}2\text{-}29)$$

where P_o^* and R_e are the dimensionless drop pressure and radius at $\theta=0$ ($\hat{\eta}=1$), respectively. Since μ' is small compared to μ, $P^{*\prime}$ can be directly obtained from the equation of motion.

$$P^{*\prime} = \frac{r^{*2} G (1-\hat{\eta}^2)s^2}{2(G-1)} + P_o^{*\prime} \quad (4\text{-}2\text{-}30)$$

where $P_o^{*\prime}$ is the dimensionless pressure of the continuous phase at $\theta=0$ ($\hat{\eta}=1$). The constant, $P_o^{*\prime} - P_o^*$, is determined using Equation (4-2-22) at $\theta=0$ ($\hat{\eta}=1$, $\hat{\alpha}=0$)

$$P_o^{*\prime} - P_o^* = \frac{2}{RE}\left[C_2 + \sum_{m=2,4,6,..}^{\infty} \frac{(m+1)(2m+3)}{m+2} C_{m+2} R_e^m \right] - \hat{\sigma}\bar{K}\Big|_{\hat{\eta}=1} \quad (4\text{-}2\text{-}31)$$

Substitution of Equations (4-2-28), (4-2-29), (4-2-30) and (4-2-31) into (4-2-22) yields a linear equation for coefficients C_m (m=2,4,6........)

$$\begin{aligned} & C_2\left(2 - 2\frac{\cos^2\hat{\alpha}}{\cos^2\hat{\alpha}-\sin^2\hat{\alpha}} P_2(\hat{\eta}) - \frac{2\sin^2\hat{\alpha}}{\cos^2\hat{\alpha}-\sin^2\hat{\alpha}}\left(3\hat{\eta}(1-\hat{\eta}^2)^{-1}\bar{P}_2(\hat{\eta}) + 2P_2(\hat{\eta})\right)\right) + \sum_{m=2,4,..}^{\infty} C_{m+2}\Big[\\ & -\frac{(4m+6)(m+1)}{m^2+2m}\left(R_e^m - R_D^m P_m(\hat{\eta})\right) + \frac{(m+1)(4m+6)}{m+2} R_e^m - \frac{2\cos^2\hat{\alpha}}{\cos^2\hat{\alpha}-\sin^2\hat{\alpha}}\Big(\frac{m+1}{m+2}P_m(\hat{\eta}) + \\ & P_{m+2}(\hat{\eta})\Big)(m+1)R_D^m - \frac{2\sin^2\hat{\alpha}\, R_D^m}{\cos^2\hat{\alpha}-\sin^2\hat{\alpha}}\Big(\frac{m+1}{m+2}\left((m+3)\hat{\eta}(1-\hat{\eta}^2)^{-1}\bar{P}_m(\hat{\eta}) + (m+2)P_m(\hat{\eta})\right) + \Big(\frac{\hat{\eta}(m+3)\bar{P}_{m+2}(\hat{\eta})}{1-\hat{\eta}^2} \\ & + (m+2)P_{m+2}(\hat{\eta})\Big)\Big)\Big] = RE\left(\hat{\sigma}\left(\bar{K}\Big|_{\hat{\eta}=1} - \bar{K}\right) - \frac{R_D^2}{2}(1-\hat{\eta}^2)\right) \end{aligned} \quad (4\text{-}2\text{-}32)$$

on the drop surface $R_D(\hat{\eta})$.

Equation (4-2-32) is used to determine C_m (m=2,4,6,......) once the drop surface $R_D(\hat{\eta})$ is specified.

(I) Special case- For the purpose of obtaining a simple form of K, it is assumed in this case that two coefficients C_2 and C_4 are enough to describe the velocity flow field, Equation (4-2-28) then becomes

$$V_r^* = -\frac{C_2}{2}(3\cos^2\theta - 1)r^* - \frac{7}{8}C_4(5\cos^4\theta - 3\cos^2\theta)r^{*3}$$

and

$$V_\theta^* = \frac{3}{2}C_2\cos\theta\sin\theta\, r^* + \frac{35}{8}C_4\cos^3\theta\sin\theta\, r^{*3} \qquad (4\text{-}2\text{-}33)$$

The corresponding stress components τ_{rr}^*, $\tau_{\theta\theta}^*$, and $\tau_{r\theta}^*$ are obtained from the Newton's law of viscosity.

$$\tau_{rr}^* = \frac{1}{RE}\left[C_2(3\cos^2\theta - 1) + \frac{21}{4}C_4(5\cos^4\theta - 3\cos^2\theta)r^{*2}\right]$$

$$\tau_{\theta\theta}^* = -\frac{2}{RE}\left[C_2\left(\frac{3}{2}\cos^2\theta - 1\right) + C_4 r^{*2}\frac{21}{8}(5\cos^4\theta - 4\cos^2\theta)\right] \qquad (4\text{-}2\text{-}34)$$

and

$$\tau_{r\theta}^* = -\frac{1}{RE}\left[3C_2\cos\theta\sin\theta + C_4 r^{*2}\left(\frac{210}{8}\cos^3\theta\sin\theta - \frac{42}{8}\cos\theta\sin\theta\right)\right]$$

Near the end of the drop surface, the following approximations are valid.

$$\hat{\alpha} = \tan^{-1}\left(-\frac{1}{R_D}\frac{dR_D}{d\theta}\right) \cong \theta \cong 0 \quad \text{and} \quad R_D \cong R_e \qquad (4\text{-}2\text{-}35)$$

Substituting Equations (4-2-34) and (4-2-35) into (4-2-22(a)), it follows that

$$\tau_{r\theta}^* \cong 0$$

which implies

$$C_4 = -\frac{C_2}{7R_e^2} \qquad (4\text{-}2\text{-}36)$$

The corresponding velocity components in cylindrical coordinates (r,z) can be obtained from combination of Equation (4-2-33) and (4-2-36) through the transformation equations

$$V_z = -\frac{3}{4}C_2 z W_0 = \frac{3}{4}\dot{\gamma}(t)z \qquad (4\text{-}2\text{-}37)$$

and

$$V_r = \frac{1}{8}C_2 r W_0 = -\frac{1}{8}\dot{\gamma}\, r$$

where $\omega_0 C_2 = -\dot{\bar{\gamma}}(t)$ is the relation given in Equation (4-2-27).

If the drop elongation is initiated from a shape described by Equation (4-2-1) with the velocities given in Equation (4-2-37), through the same procedures as that in Section 4-2-1, the curvature K is obtained as

$$K = 3e^{5/2} \tag{4-2-38}$$

(II) Numerical simulation-- In this case, the dynamics of the drop elongation phenomena is simulated under the condition that the product of the rotational speed ω and the drop radius R at $\hat{\eta}=0$. is constant through the course of simulation. If Equation (2-4-15) is applicable, simulation of this kind is equivalent to that of creep experiment described in Section 4-1. An iterative technique is used which is similar to that developed for the free stream line problems (70). In the present case, an initial shape is given, the corresponding velocity field is found under the condition of ωR =constant. These velocities along with a given dimensionless time interval Δt ($\Delta t = \omega_0 \Delta\bar{t}$, $\Delta\bar{t}$ is the dimensional time) are used to compute a new shape (and therfore K), for which a new solution for the velocity field is computed. This procedure is continued until the time response of the drop elongation is aquired.

It should be noted that at each step of the solution, the problem is one of finding the velocity field for a given instantaneous drop shape. For this purpose, two boundary methods are used: the least square and the orthogonal collocation methods (71,72). With the least square method, the boundary condition, Equation (4-2-32), is considered at a finite set of boundary points. The number of equations is greater than the number of unknown coefficients and at each point Equation (4-2-32) is satisfied approximately. The approximation is such that the errors in the entire set of equations are minimized in the least square sense. With the orthogonal collocation method, Equation (4-2-32) is satisfied exactly at a set of special chosen collocation points. The number of equations in this case is equal to the number of unknown coefficients. Details on how to choose the collocation points is described in Appendix II. In performing the numerical calculations, the drop surface is specified by giving R_D, the dimensionless drop radius at a set of θ values which are selected in the following manner.

$$\begin{aligned} 0^\circ < \theta < 20^\circ \qquad & \Delta\theta = 1^\circ \\ 20^\circ < \theta < 40^\circ \qquad & \Delta\theta = 2^\circ \\ 40^\circ < \theta < 90^\circ \qquad & \Delta\theta = 10^\circ \end{aligned} \tag{4-2-39}$$

The values of R_D at these positions are determined from the shape given by Princen,et. al. (11). The first and second derivatives of R_D with respect to θ are then calculated by using three point approximations. These derivatives are used in computing $\hat{\alpha}$ and K. When coefficients C_m (m= 2,4,...) have been determined, the change in the drop shape in a dimensionless time is computed as

$$R_D(\theta, t+\Delta t) = R_D(\theta, t) + \left(V_r^* - V_\theta^* \frac{1}{R_D} \frac{dR_D}{d\theta}\right) \Delta t \qquad (4\text{-}2\text{-}40)$$

The drop elongation has been simulated at Δt intervals over a time period T. An optimal value of Δt is chosen when the successive calculated values of K, after the simulation for different values of Δt, are within 95% of one another.

For the sake of comparing the least square method with the orthogonal collocation method, Equation (4-2-32) is solved using both methods for different number of coefficients on a given drop shape. The degree to which Equation (4-2-32) is satisfied is indicated in Σ which is defined as

$$\Sigma = \frac{\text{total errors in Equation (4-2-32)}}{\text{number of points used}} \qquad (4\text{-}2\text{-}41)$$

The results of Σ versus number of coefficients used in these two methods are shown in Fig. 4-5 for one iteration. Two conclusions can be drawn from Fig. 4-5: First, the orthogonal collocation method works better than the least square method except in the case of four coefficients; and second, two coefficients are enough to describe the velocity field.

Three simulations of drop elongation under the conditions that $\frac{\omega R}{\omega_0 R_0}$ is equal to 1.7, 2 and 3 are carried out using the orthogonal collocation method for two coefficients C_2 and C_4. The time dependent drop shapes along with the stream lines for different values of $\frac{\omega R}{\omega_0 R_0}$ are shown in Fig. 4-6 to 4-8. It is noteworthy that the shapes computed are very similar to the shapes observed in the elongation experiment. The resulting

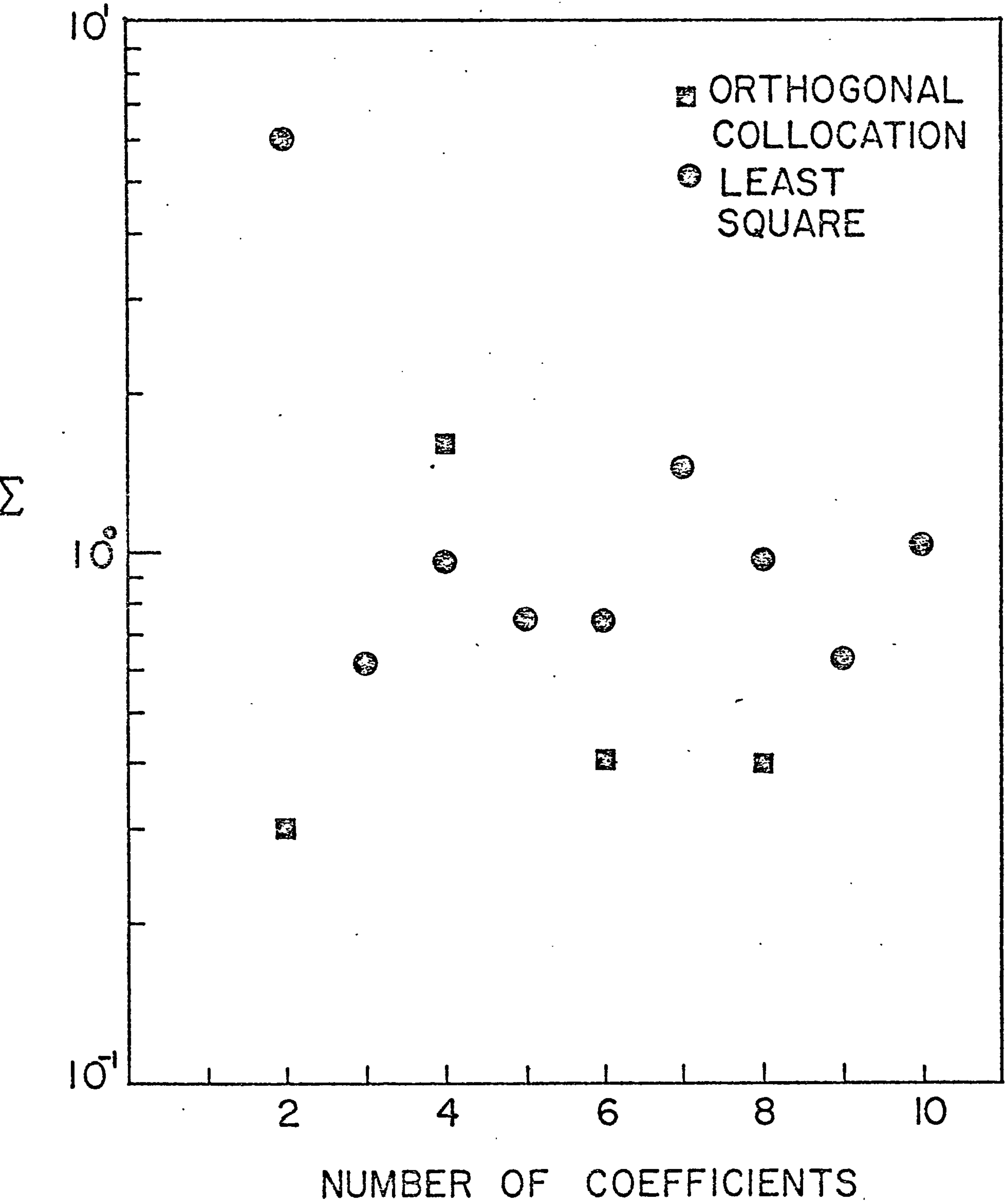

Figure 4-5 Comparison of the Orthogonal Collocation Method with the Least Square Method.

Figure 4-6 The Resulting Shape and Internal Flow Pattern of the Drop under Condition of $\omega_R/\omega_0 R_0$ =1.7(t= $\omega_0 \bar{t}$, $\bar{t}$ is the dimensional time)

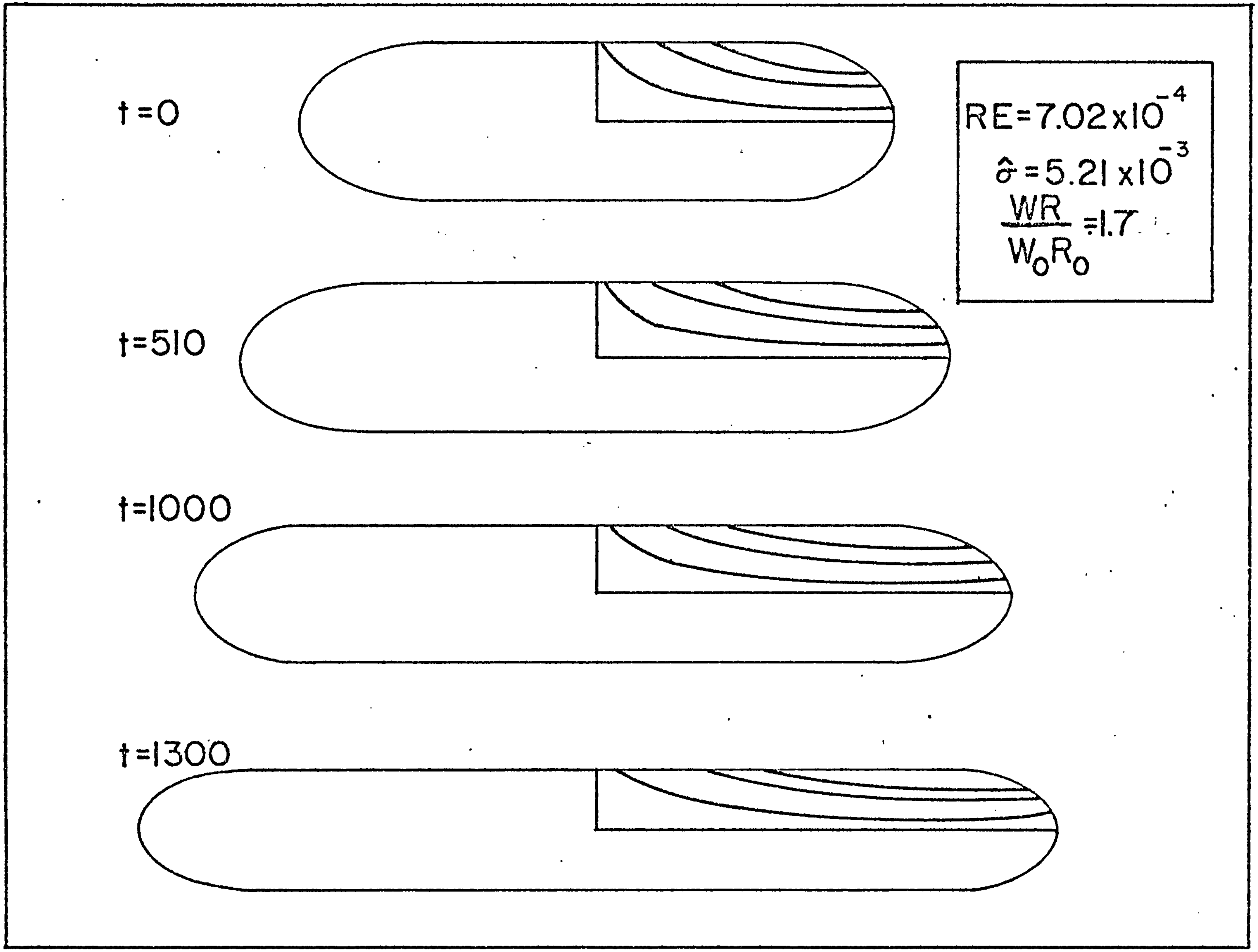

Figure 4-7 The Resulting Shape and Internal Flow Pattern of the Drop under Condition of $\omega R/\omega_0 R_0=2$ ($t=\omega_0\bar{t}$, $\bar{t}$ is the dimensional time)

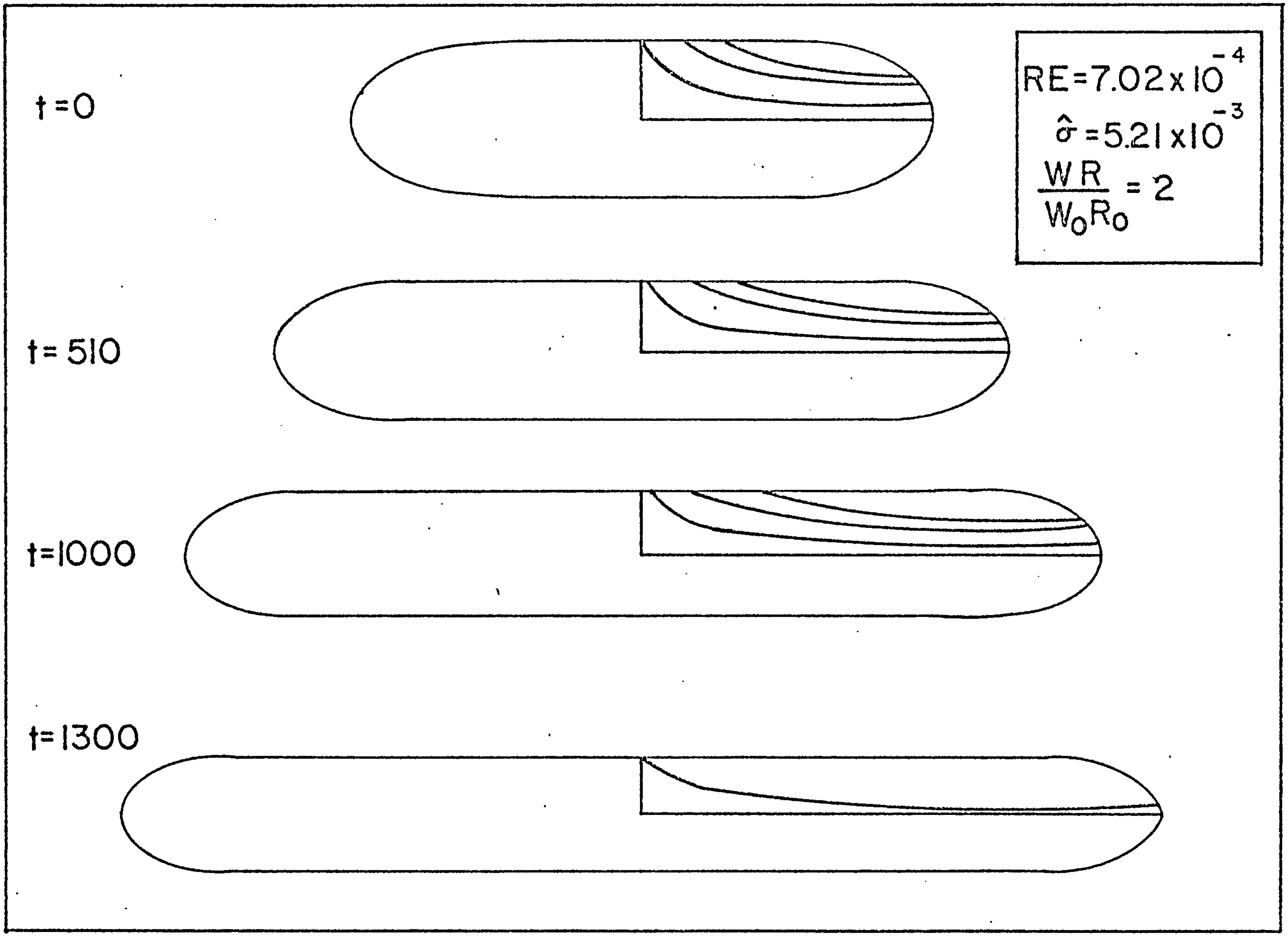

Figure 4-8 The Resulting Shape and Internal Flow Pattern of the Drop under condition of $\omega R/\omega_0 R_0 = 3$ ($t=\omega_0 \bar{t}$, $\bar{t}$ is the dimensional time)

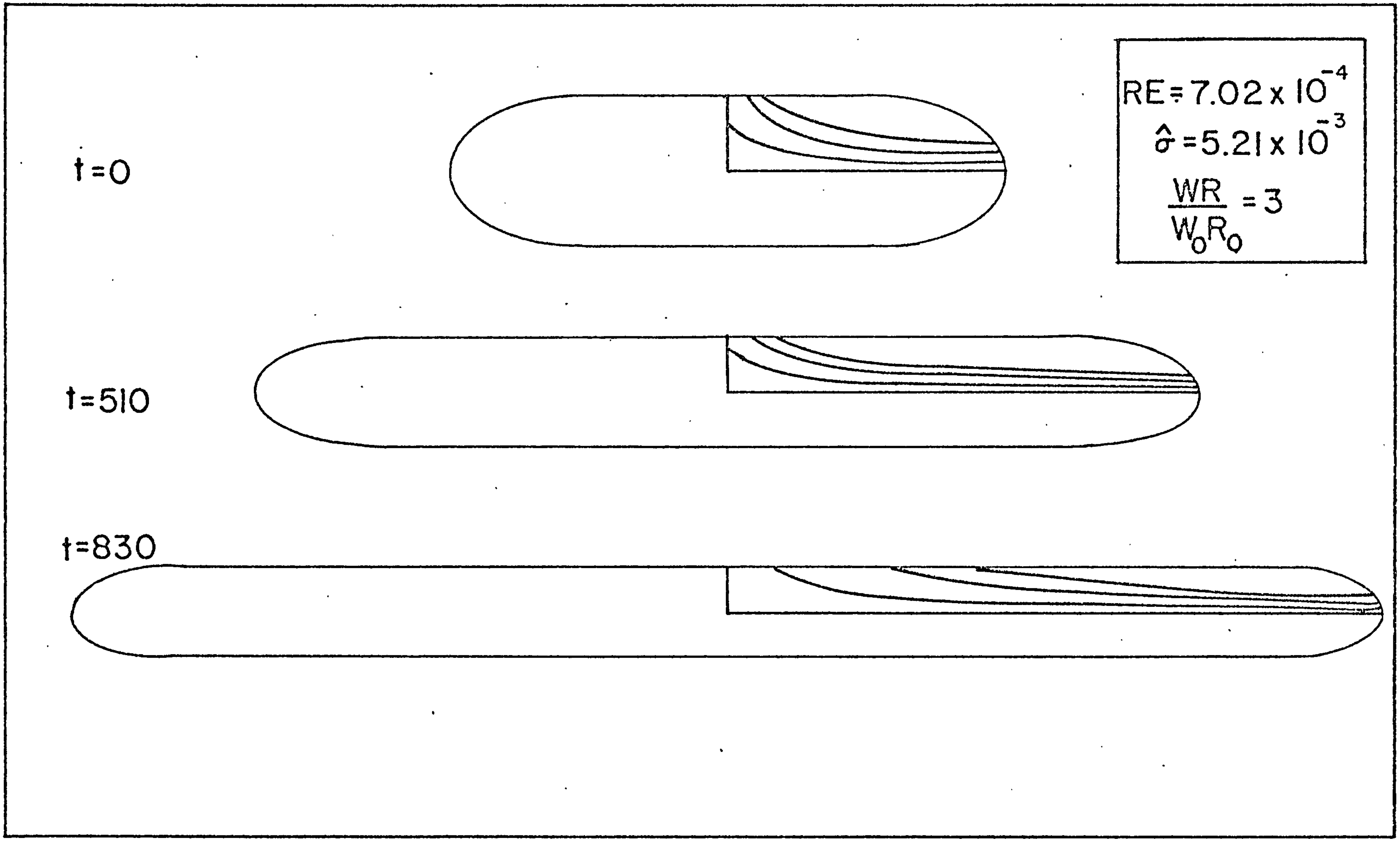

curvature K for three different values of $\frac{\omega R}{\omega_o R_o}$ is corrëlated as a function of the extensional strain $\bar{\gamma}(t)$ in Fig. 4-9. $\bar{\gamma}(t)$ is defined as $2 \log_e \frac{R_c(0)}{R_c(t)}$ in this case and R_c is the drop radius at $\theta = 90^\circ$. It is interesting to note that in Fig. 4-9 the curves of K versus $\bar{\gamma}$ for three different values of $\frac{\omega R}{\omega_o R_o}$ fall on the same line. This is in agreement with the trend predicted both by Equation (4-2-38) and (4-2-10) that K is only function of $\bar{\gamma}$.

4-2-3. Comparison with the Experimental Results

Equations (4-2-10), (4-2-38) and the numerical simulations in Section 4-2-2 give various predictions of K as a function of the extensional strain $\bar{\gamma}$. It is important to know which of those predictions gives a close estimate of K while a liquid drop is experimentally extended. To this end, experiments are carried out in which a Newtonian drop with known viscosity μ (and hence, extensional viscosity $\bar{\eta}$) is extended at constant extension rate in the drop elongation apparatus. With the experimental data of the instantaneous rotational speed ω and drop diameter, Equation (2-4-14) is used to calculate K as a function of the extensional strain $\bar{\gamma}$ which in this case is equal to $\dot{\bar{\gamma}}t$. The experimental results of K versus $\bar{\gamma}$ for various extension rate experiments are shown in Fig. 4-9 along with the predictions of Equations (4-2-10), (4-2-38) and the numerical simulations. As a comparison, it appears that in spite of the experimental scatter,

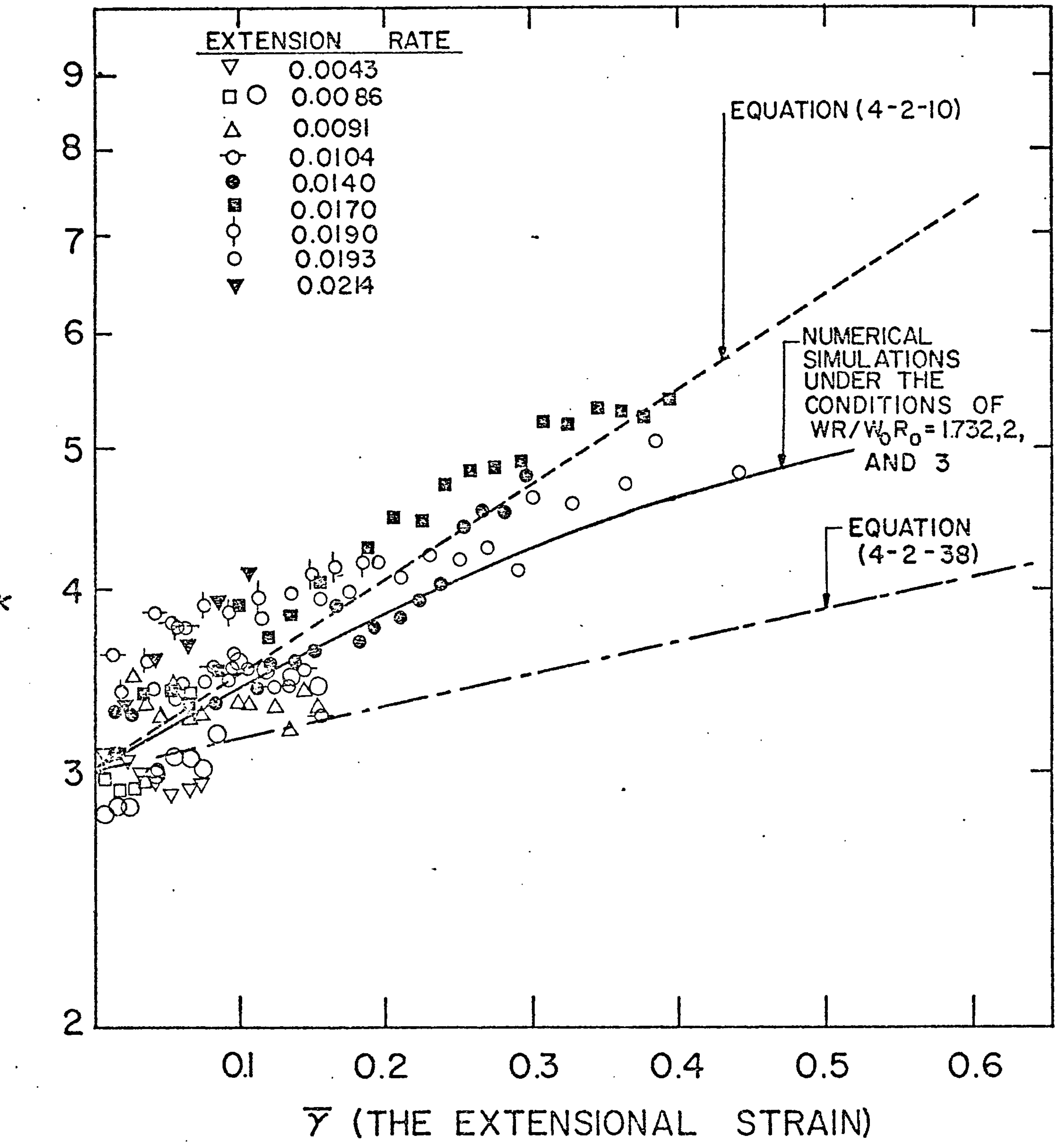

Figure 4-9 Comparison of the Experimental Data of K vs. $\overline{\gamma}$ with the Predictions from Equations (4-2-10), (4-2-38), and Numerical Simulations

Equation (4-2-10) which resulted from an anlysis based on the assumption that the liquid particles near the end of the drop surface experience extensional flow can describe the data of reasonably well. Therefore, for all the experiments performed in the present work, Equation (2-4-14) is used along with Equation (4-2-10).

4-3. Optimal Operating Range Subject to Operational Constraints

While a drop is extended in the drop elongation apparatus, the maximum possible extension rate which can be achieved is dependent on several factors. These are

(1) The buoyancy force which causes the drop to move off of the axis of rotation.

(2) The fluid properties such as density difference $\Delta\rho$, interfacial tension σ, etc.

(3) The time period of the experiment.

(4) The maximum speed of the drive motor ω_{max}.

In this section, an analysis in which the maximum extension rate is related to these four factors is described.

A necessary condition in the experiment is that the ratio of the centrifugal force to the buoyancy force must be greater than one. In that case, the drop will stay on the axis of rotation. Thus,

$$\frac{\frac{\Delta\rho\omega_0^2 R_0^2}{2} 4\pi R_0 L}{2\Delta\rho\pi R_0^2 L g} \geq 1$$

or

$$\omega_0^2 R_0 \geq 1000 \qquad (4\text{-}3\text{-}1)$$

where ω_0 and R_0 are the initial drop rotational speed and radius respectively.

Since the drop elongation is initiated from a long equilibrium configuration, it follows from Princen et. al.(11) that

$$\frac{\Delta\rho\omega_o^2 R_o^3}{2\sigma} = 2 \qquad (4\text{-}3\text{-}2)$$

Substitution of Equation (4-3-1) into (4-3-2) yields

$$R_o \leq 0.06325\left(\frac{\sigma}{\Delta\rho}\right)^{1/2} \qquad (4\text{-}3\text{-}3)$$

Equation (4-3-3) indicates that the maximum possible starting radius in the drop elongation experiment is dependent solely on the physical properties of fluid systems involved. Combination of Equations (2-4-14) and (4-2-10) gives

$$\bar{\eta} = \frac{\sigma}{R\dot{\gamma}}\left(\frac{\Delta\rho\omega^2 R^3}{2\sigma} + 1 - 3e^{\frac{3}{2}\dot{\gamma}t}\right) \qquad (4\text{-}3\text{-}4)$$

where $\bar{\eta}$ is taken as 3μ.

The time dependent response of the drop radius in a constant extension rate experiment is

$$R = R_o e^{-\frac{1}{2}\dot{\gamma}t} \qquad (4\text{-}3\text{-}5)$$

Taking t=T, $R_o = R_{o_{max}}$, and $\omega = \omega_{max}$, Equation (4-3-4) becomes

$$\dot{\gamma}_{max} = \frac{\sigma}{\bar{\eta}}\left(\frac{\Delta\rho\,\omega_{max}^2 R_{o_{max}}^2}{2\sigma} e^{-\dot{\gamma}_{max}T} + \frac{1}{R_{o_{max}}} e^{-\frac{\dot{\gamma}_{max}T}{2}} - \frac{3}{R_{o_{max}}} e^{2\dot{\gamma}_{max}T}\right) \qquad (4\text{-}3\text{-}6)$$

Substituting Equation (4-3-3) into Equation (4-3-6), it follows that

$$\dot{\gamma}_{max} = \frac{\sigma}{\bar{\eta}}\left(0.002\,\omega_{max}^2 e^{-\dot{\gamma}_{max}T} + 15.8\left(\frac{\Delta\rho}{\sigma}\right)^{1/2} e^{-\frac{\dot{\gamma}_{max}}{2}T} - 47.43\left(\frac{\Delta\rho}{\sigma}\right)^{1/2} e^{2\dot{\gamma}_{max}T}\right) \qquad (4\text{-}3\text{-}7)$$

The effects of each of the variables $\bar{\eta}$, σ, ω_{max}, T, and $\Delta\rho$ in Equation (4-3-7) on $\dot{\gamma}_{max}$ were investigated by changing one of those variables and calculating the resulting $\dot{\gamma}_{max}$ from

Equation (4-3-7) while the other four variables were held constant. It was found that the maximum possible extension rate $\dot{\gamma}_{max}$ will increase by increasing σ and ω_{max} or decreasing $\Delta\rho$, $\bar{\eta}$, and T.

It appears that for the purpose of enlarging the operating range of extension rate, the only physically feasible way is to increase ω_{max} in the drop elongation apparatus.

The maximum extension rates for the fluid systems used in the present work are listed in Table 4-1.

4-4. Experimental Difficulties

Several experimental difficulties in using the drop elongation apparatus are discussed in this section, particularly those associated with the response of the feedback control system.

An unwanted response of the feedback controller is created both by the continuous decay in the light intensity of the collimated light source and by the noise signal inherently existing in the voltage signal generated from the photomultiplier tube. The decay in the light intensity of the collimated light source is the general characteristics of the light bulb used and can not be avoided. But its effect on the response of the controller is decreased to a minimum by readjusting the light intensity to the original level through increasing the voltages imposed on the photomultiplier tube between experiments. The noise

Table 4-1 Maximum Possible Extension Rate for Fluid Systems Used

ω_{max} = 3000 RPM , T = 10 seconds

Fluid Systems	Density Difference $\Delta\rho$ (g/cm^3)	Interfacial Tension σ (dyne/cm)	Maximum Possible Extension Rate (sec^{-1})
Cannon ASTM Standard oil in glycerol-water solution	0.307	21	0.07
PIB* in glycerol -water solution	0.329	11	0.051
PAA** in PS-TCE***	0.433	9	0.0365

PIB* - 10% polyisobutylene in Decahydronaphthalene(Decalin)

PAA**- 2.8% polyacrylamide (Separan AP 30) in 50:50 glycerol-water

PS-TCE***- 4% polystyrene in tetrachloroethylene level in the voltage signal from the photomultiplier tube can be eliminated by using a lowpass filter of low cutoff frequency. However, the use of such a filter imposes a significant time delay on the response of the feedback control system, and is to be avoided if possible. In the present work a notch filter which filters part of the noise signal out and imposes no time lag is used. Additional difficulties associated with the response of the servo controller are the adjustment of the controller gain and the axial movement of the liquid drop in the rotating cylinder. It is clear that the value of the controller gain is very critical to the drop response. If the gain is too large, it will cause the whole rotating system to oscillate because of the noise existing in the signal of the photomultiplier tube, and if the gain is too small, very little agreement between the response of the drop and the signal from the functional generator is achieved. As a compromise, moderate values in the controller gain are selected for the different fluid systems used and experiments performed.

The reasons for leaving the drop injection system in place during the experiments has already been discussed in Section 3-3. However, the existence of the drop injection tube inside the rotating cylinder creates an unsymmetric flow field during the rotation of the cylinder and hence, results an axial movement of the drop. If the drop shape is not a cylinder with uniform radius, a false response of the feedback control system will result from the axial movement of the drop. Nevertheless, this effect can be diminished if the drop elongation is initiated from an equilibrium configuration with large L/D (L and D are the drop length and diameter respectively).

Under the conditions suggested above, all of the experiments mentioned in Section 4-1 except the superimposed oscillatory are performed in the drop elongation apparatus with a Newtonian silicone oil. It is found experimentally that the stress relaxation and recoil experiments can not be carried out successfully. The reasons for the failure of those experiments are described as follows.

In a stress relaxation experiment, the steady extension needs to cease abruptly after the drop is extended at constant extension rate for a period of time. However, due to the time lag which the system takes in transmitting the speed of rotation to the response of the drop, and the type of controller used by which the speed of rotation is proportional to the difference between S_D the diameter signal and the signal (S_F) from the function generator, the steady extension is impossible to stop instantaneously and thus a poor stress relaxation experiment is achieved.

The difficulties with the recoil experiment is quite different from those for the stress relaxation experiment. After the drop is extended either at constant extension rate or at constant extensional stress over quite a period of time, the system is braked to a rotational speed just sufficient to hold the drop along the axis of rotation and the resulting contraction of the drop is measured as a function of time. The reason for the difficulty of this experiment is that during the time that the system is braked from a high rotational speed to a low rotational speed, the drop experiences both radial vibration and axial movement. Under such conditions, very poor results are obtained.

It is concluded then that unless certain revisions of the servo controller and the collimated light source are made, the present drop elongation apparatus can be used in the stress growth and creep experiments only. The results of the Newtonian silicone oil in the creep and stress growth experiments are described in next chapter.

CHAPTER V

OBSERVED RESPONSE OF NEWTONIAN FLUID IN VARIOUS EXPERIMENT

Because of the experimental difficulties and limitations as discussed in Section 3-4, only stress growth and creep experiments were carried out in the drop elongation apparatus. A silicone fluid was used as the drop phase in these experiments. Results for this fluid serve primarily to validate both the experimental techniques and the mode of analysis, since this fluid is Newtonian in the range of deformation rates studied and its behavior can be predicted.

5-1. Fluids

A glycerol-water solution was used as the continuous phase and a viscosity standard silicone oil (Cannon ASTM Visc. no. N190000) was used as the disperse phase. The material properties are summarized in Table 5-1. The viscosity of the silicone oil was measured on the Weissenberg Rheogoniometer with the temperature controlled at 25°C. The Newtonian behavior of the silicone fluid reflected by a constant shear viscosity is clearly evident in Fig. 5-1. It should be noted that as the shear rate $\dot{\gamma}$ is greater than 4 sec^{-1}, small first normal stress difference $-(\tau_{xx}-\tau_{yy})$ was exhibited by the silicone oil as shown in Fig. 5-1. This small elastic effect was also found in the properties of silicone oil used by Leider (73). The viscosity

Table 5-1 Properties of the Materials Used in the Newtonian Studies at 25 °C.

Continuous Phase	Disperse Phase	Density Continuous Phase (g/cm^3)	Density Disperse Phase (g/cm^3)	Interfacial Tension (dyne/cm)	Zero Shear Viscosity Continuous Phase (poise)	Zero Shear Viscosity Disperse Phase (poise)
Glycerol-water solution	Cannon ASTM Standard oil (visc. no. N190000)	1.21	0.915	21.0* 20.6**	1.01	5750

* - Rotating Drop Method
**- Pendant Drop Method

Figure 5-1 Viscosity and Normal Stress Difference Data for Cannon ASTM Viscosity Standard Oil at 25°C

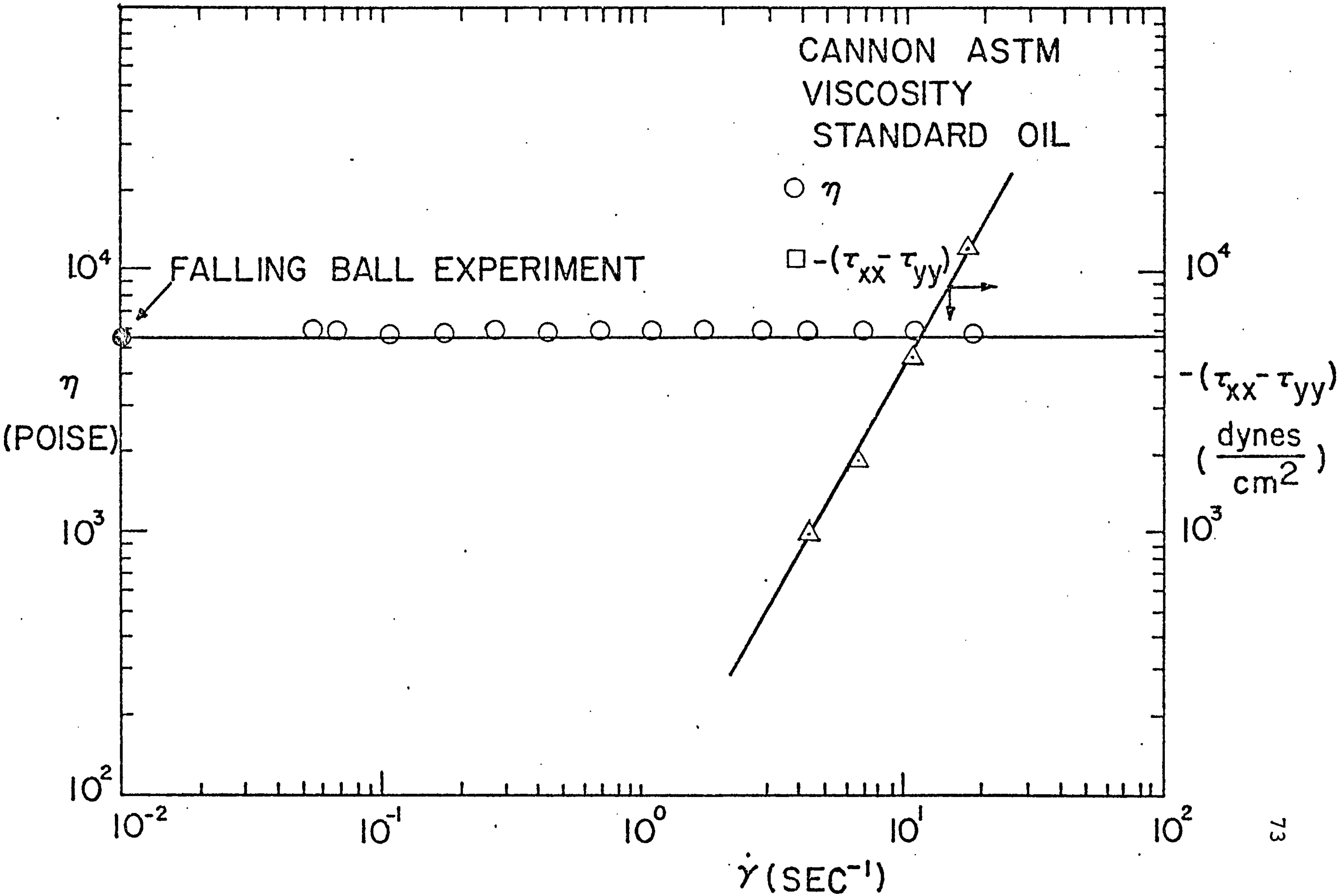

data checked very well with data obtained from separate measurements using the falling ball method (79). The interfacial tension was measured by the rotating drop method (11,69). However, the pendant drop method (74) was also used to measure the interfacial tension and the data were in good agreement with that from the rotating drop method. The densities of the fluid systems were obtained by weighing the samples in a 10 c.c. pycnometer on an electrical balance.

5-2. Stress Growth Experiment

5-2-1. Experimental Procedures

The stress growth experiment with the drop elongation apparatus was carried out as follows:

The cylinder was filled with the continuous phase fluid (glycerol-water solution). A liquid drop (about 6.5 cm^3) of the disperse phase was introduced by pressing the piston in the injection tube while the whole system (drop + continuous phase + glass cylinder) rotated at a low speed. The L-shaped steel wire was used to sever the liquid drop from the injection tube. The system was then turned on at speed ω_0 and the drop was allowed to reach its equilibrium shape. The temperature in the constant temperature chamber was controlled at 25°C. The rotational speed ω_0 was selected so that the speed ω_0 and its corresponding equilibrium drop diameter D ($=2R_0$) satisfy Equations (4-3-1) and (4-3-3).

$$\omega_o R_o \geq 1000 \tag{4-3-1}$$

$$R_o \leq 0.06325 \left(\frac{\sigma}{\Delta\rho}\right)^{1/2} \tag{4-3-3}$$

The photomultiplier tube, the quadratic inverter and a logarithmic amplifier were connected in series.

While the photomultiplier tube received the light passing through the drop and the rotating cylinder, the logarithmic amplifier generated an output voltage signal equal to $(10 \log_{10} S_D)$, where S_D was the output signal of the quadratic inverter and was quantitatively proportional to the drop diameter D. In addition, the quadratic inverter and the tachometer were connected to a multiplier. By this arrangement, the multiplier generated an output signal which was a measure of the extensional stress. Since, in the stress growth experiment, the drop needs to be extended at a constant extension rate which requires the output signal from the logarithmic amplifier to vary linearly with time. Therefore, after the drop reached its equilibrium shape, the output signal from the logarithmic amplifier was fed back into the comparator along with a linear signal from the function generator. The slope of the linear signal produced by the function generator was prescribed according to the desired extension rate. With this feedback loop, the drop was able to be extended under the condition of constant extension rate. Typical sequences of drop elongation are shown in Fig.5-2. Throughout the course of the experiments, the output signals of the logarithmic amplifier and the multiplier were recorded as a function of time.

Figure 5-2 Sequences of Drop Elongation

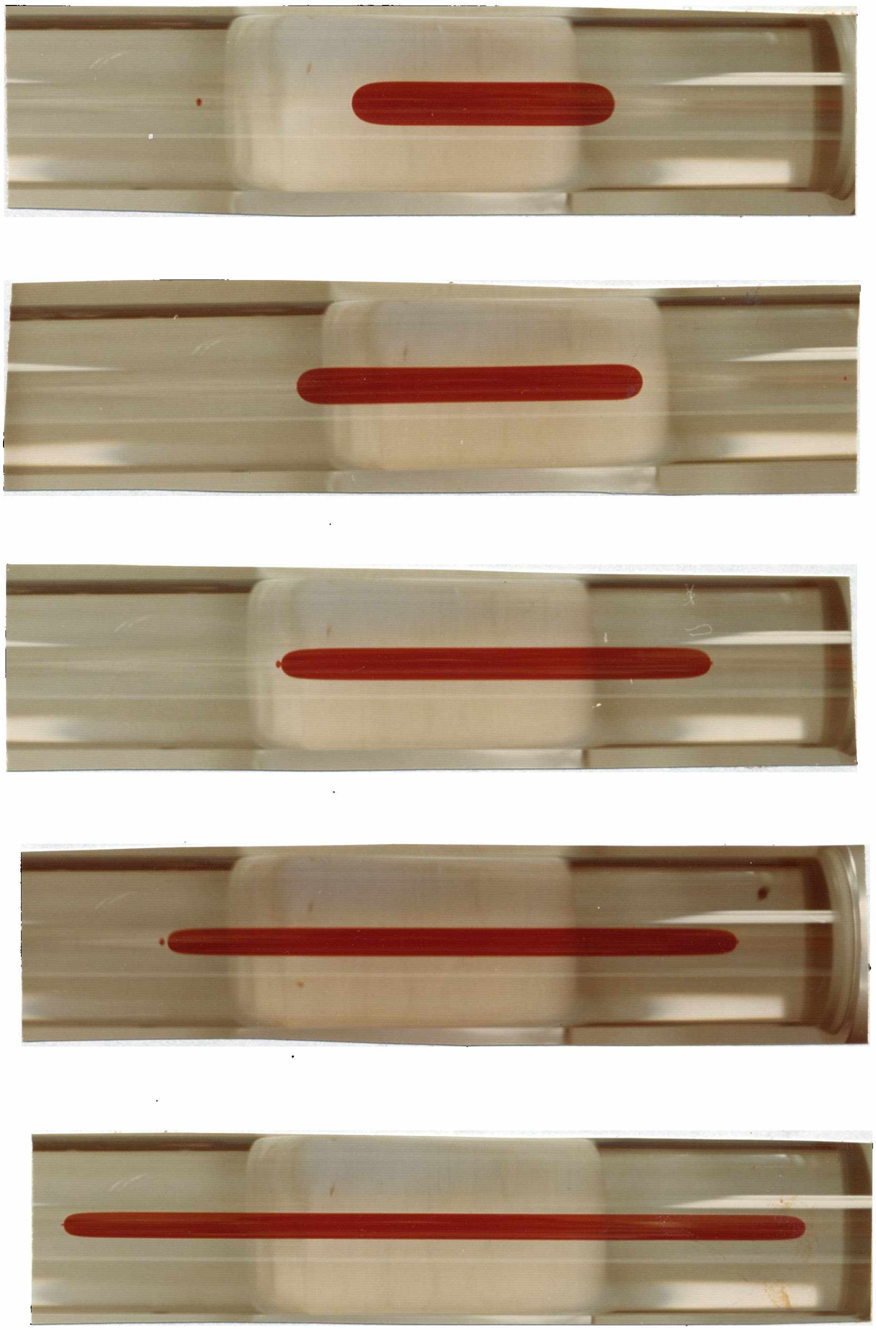

5-2-2. Experimental Results

From the calibrations described in Section 3-5-1 , the following relations were obtained.

$$D = 0.676 \; S_V \tag{5-2-1}$$

$$S_D = 3.45 \; S_V \tag{5-2-2}$$

and
$$\omega = 41.88 \; \omega_T \tag{5-2-3}$$

where D is the actual drop diameter (cm), S_V is the visual drop diameter observed from a cathetometer, ω_T is the output signal (volts) from the tachometer and ω is the actual rotational speed (radian/sec). Combination of Equation (5-2-1) and (5-2-2) yields

$$S_D = 5.1 \; D \tag{5-2-4}$$

Fig. 5-3. shows the curves of S_V versus D and S_D versus D obtained from the calibrations mentioned in Section 3-5-1. For the purpose of checking the accuracy of the calibration S_D versus D, stress growth experiments were performed. The drop was extended at a constant extension rate. The resulting responses in drop diameter were filmed by a Beaulieu R-16 movie camera and also measured with the light sensing assembly. The output signal S_D from the quadratic inverter was recorded as a function of time. The drop diameters during the experiment were then obtained both from the film and the signal S_D. In the latter regard, Equation (5-2-4) was used. Based on those data of drop diameter, the extensional strain $\bar{\gamma}$ can be calculated according to the following equation:

$$\bar{\gamma} = 2 \log_e \frac{D(0)}{D(t)} \tag{5-2-5}$$

where D(0) and D(t) are the drop diameters at time=0, and t

Figure 5-3 Calibration Curves for the Output Signal S_D from the Quadratic Inverter vs. Drop Diameter - Silicone Oil

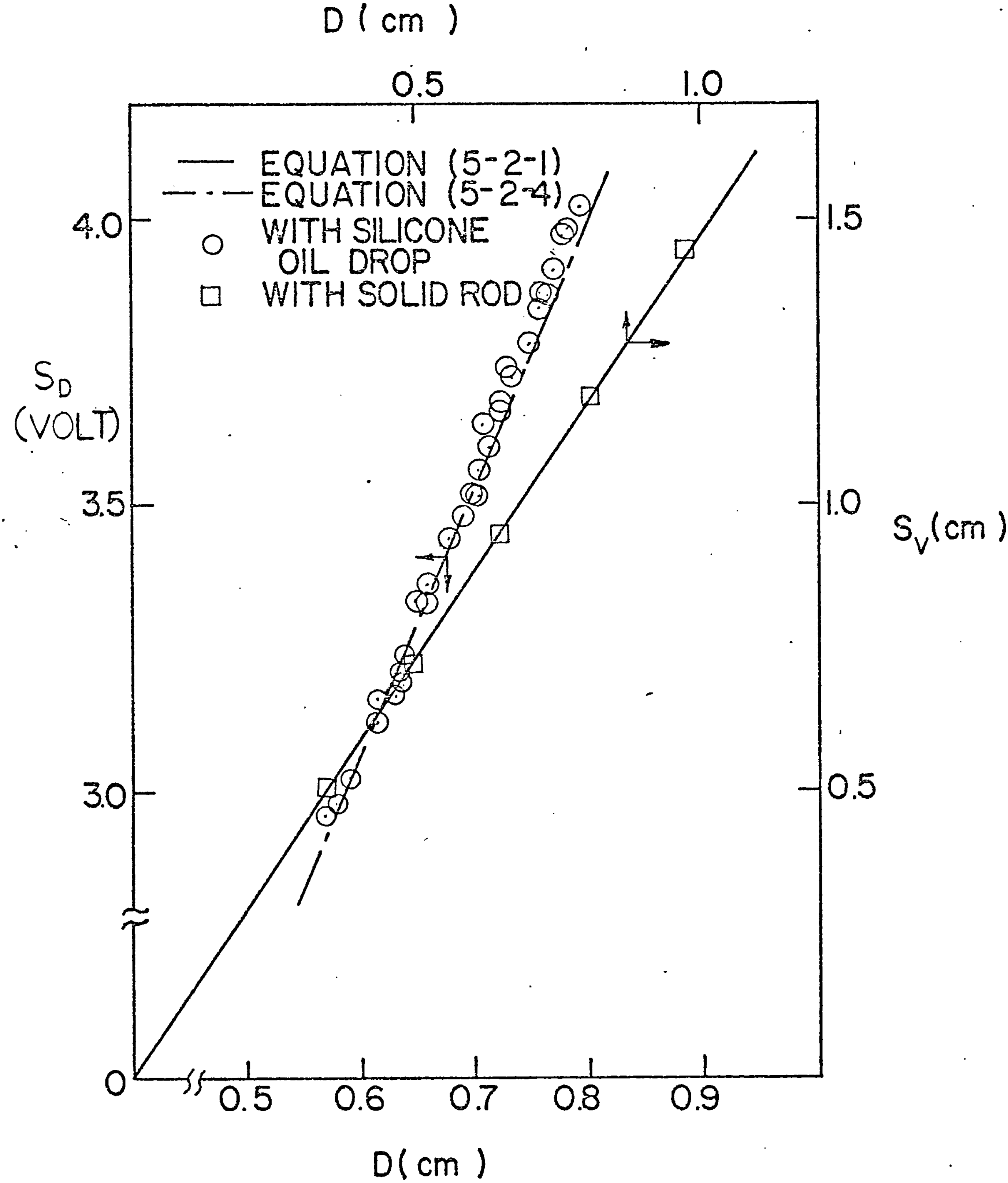

respectively. The values of the extensional strain obtained both from the signal S_D and the film for two stress growth experiments are compared in Fig. 5-4. In general, the extensional strains obtained from the signal S_D for two stress growth experiments are in good agreement with those obtained from the movie films. It should be worthwhile to note that the extension rates for those two stress growth experiments are constant as expected. Typical experimentally recorded signals from the logarithmic amplifier and the multiplier in the stress growth experiment are shown in Fig. 5-5. The output signals of the logarithmic amplifier and the multiplier are equal to $(10 \log_{10} S_D)$ and $\left(\frac{\omega_T S_D}{10}\right)$ respectively. Because of the noise generated by the photomultiplier tube, the output signal from the logarithmic amplifier wiggles. As discussed in Section 4-4, that elimination of the noise will impose a time lag on the response of the feedback system, some noise was allowed to exist as a compromise.

After the drop was extended at a constant extension rate, the output signal $\left(\frac{\omega_T S_D}{10}\right)$ of the multiplier immediately experienced an approximate "step change" and then increased slowly as shown in Fig. 5-5. This slow increase after the "step change" in $\left(\frac{\omega_T S_D}{10}\right)$ is due to the balancing of the interfacial tension effect $3e^{1.5\bar{\gamma}}$ since $\bar{\gamma}$ increased with respect to time.

Using Equations (5-2-3) and (5-2-4), D and ωD were calculated from those recorded signals of $(10 \log_{10} S_D)$ and $\left(\frac{\omega_T S_D}{10}\right)$.

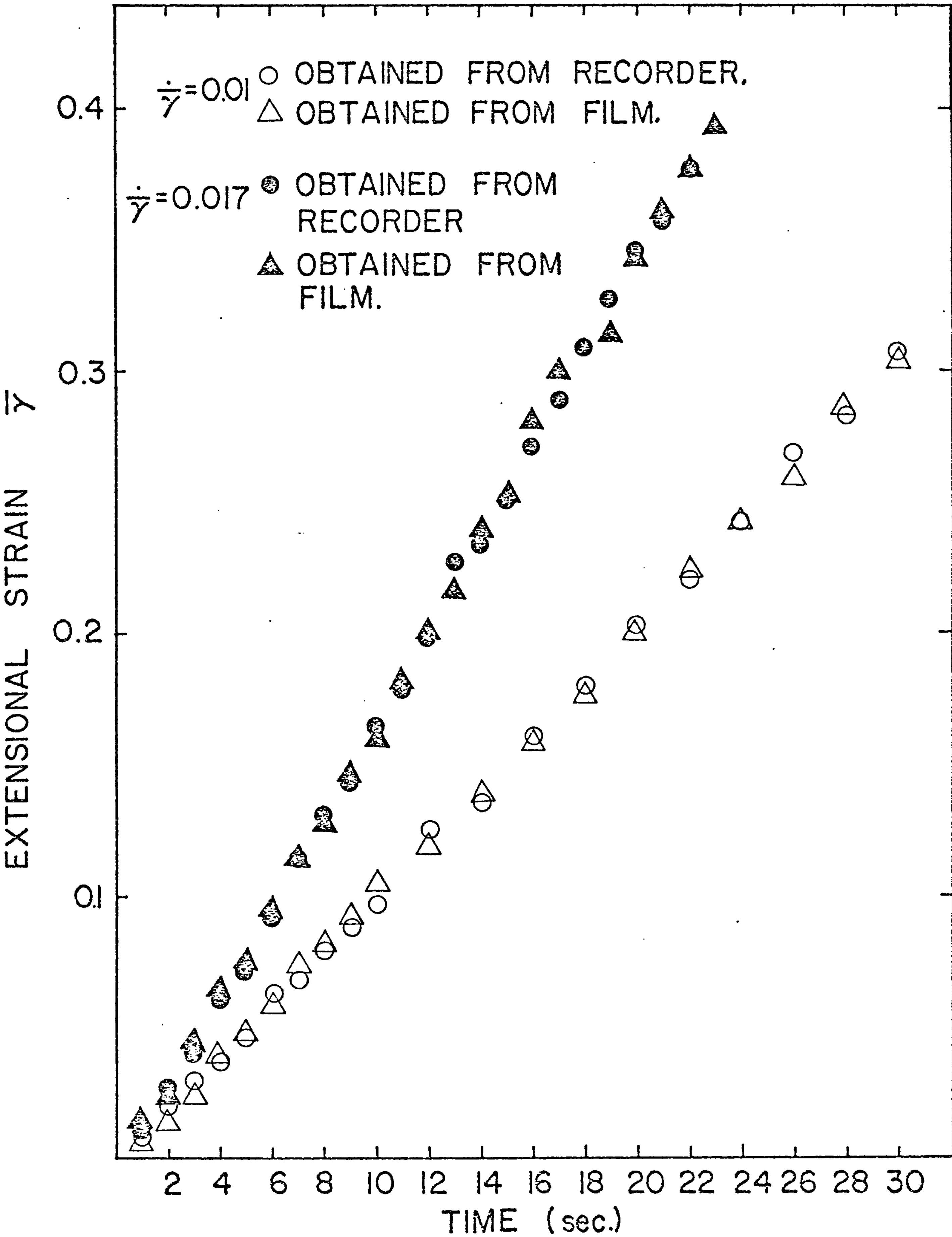

Figure 5-4 Comparison of the Extensional Strain Obtained from the Recorder with that Obtained from Movie Films

From the multiplier

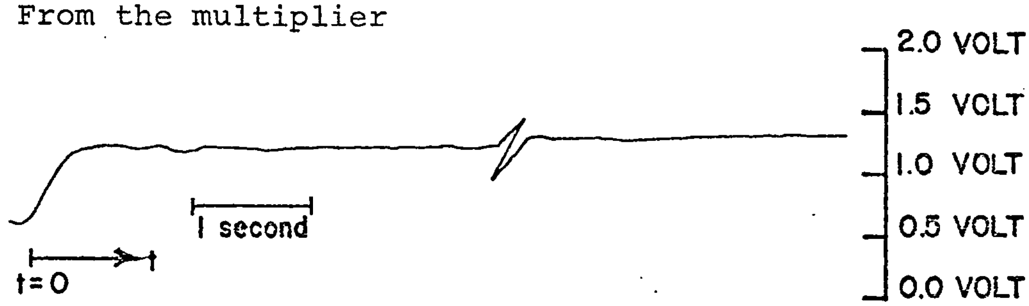

From the logarithmic amplifier

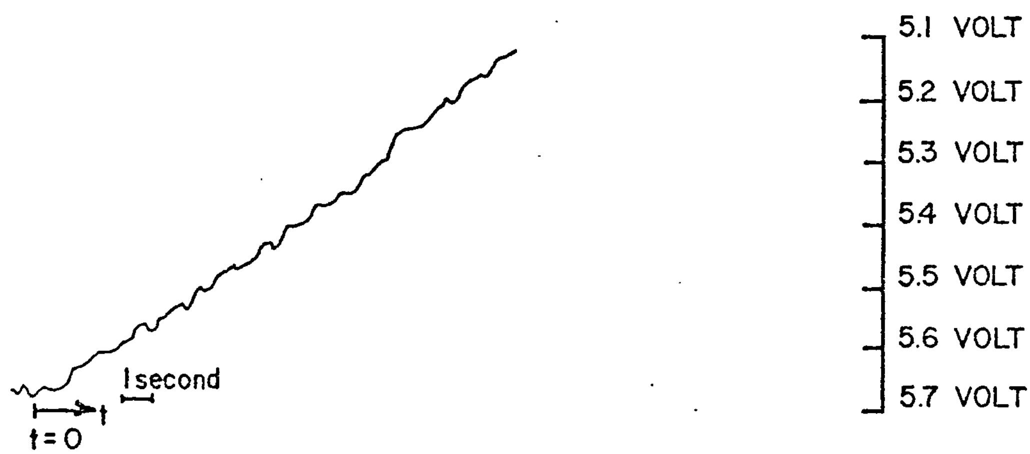

Figure 5-5 The Output Signals from the Logarithmic Amplifier and the Multiplier in the Stress Growth Experiment with Cannon ASTM Viscosity Standard Oil

With the data of drop diameter D, the extensional strain γ and the dimensionless curvature K were obtained from Equation (5-2-5) and (4-2-10) respectively. Then from the data of ωD and K, coupled with the physical properties of the fluid systems used, the extensional stress ($\Pi_{zz} - \Pi_{rr}$) was determined by the use of Equation (2-4-13). The experimental extension rate $\dot{\gamma}$ was calculated according to the following equation:

$$\dot{\gamma} = 0.4606\, J \qquad (5\text{-}2\text{-}6)$$

where J is the slope of the output signal from the logarithmic amplifier with respect to time.

An apparent extensional viscosity $\bar{\eta}^+$ is defined as the ratio of instantaneous extensional stress $(\Pi_{zz}(t) - \Pi_{rr}(t))$ to the extension rate $\dot{\gamma}$.

$$\bar{\eta}^+ = \frac{\Pi_{zz}(t) - \Pi_{rr}(t)}{\dot{\gamma}} \qquad (5\text{-}2\text{-}7)$$

In Fig. 5-6, $\bar{\eta}^+$ is plotted versus t for different stress growth experiments. The steady extensional viscosity $\bar{\eta}$ was obtained as the value of $\bar{\eta}^+$ when $\bar{\eta}^+$ was independent of time. As shown in Fig. 5-6, in all the stress growth experiments, the steady extensional viscosities were reached in a time period on the order of one second. Because the silicone oil is a Newtonian fluid as indicated in Fig. 5-1, the steady extensional viscosity should be reached immediately after the extension rate was imposed. In this connection, numerous efforts have been devoted to shortening the response time of the servo controller. However,

Figure 5-6 Instantaneous Extensional Viscosity Data for the Stress Growth Experiments with Cannon ASTM Standard Oil

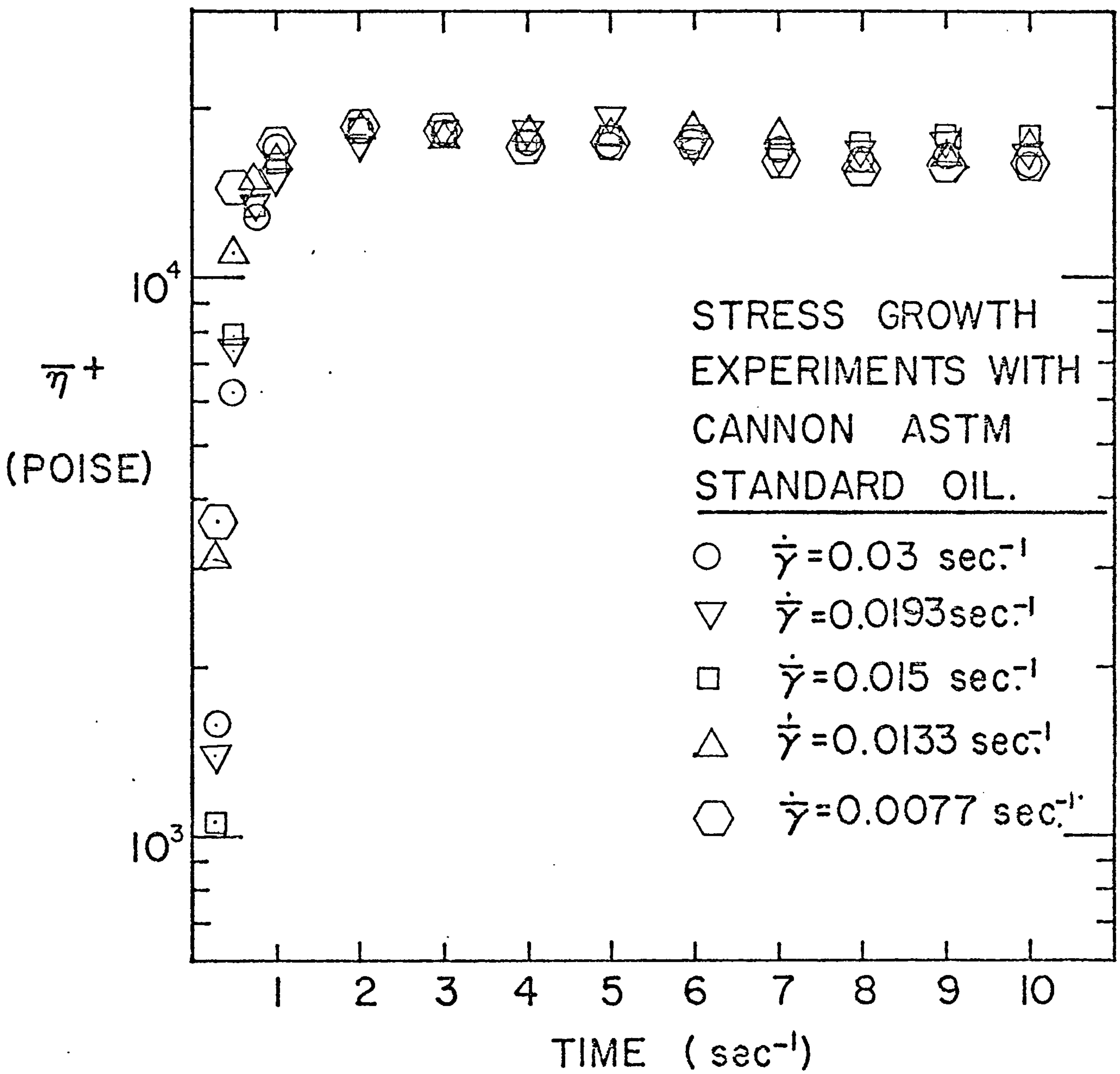

considering the inertial effects present and the questionable validity of rigid body assumption in the initial period of drop elongation, operating with a response time of about one second was found to be "optimal" for the apparatus used.

The steady extensional viscosities obtained from several stress growth experiments are plotted versus $\dot{\gamma}$ in Fig. 5-7. Subject to the constraints discussed in Section 4-3, the maximum possible extension rate used is 0.03 sec^{-1}. As shown in Fig. 5-7, the agreement between the experimental data of the extensional viscosity and the Trouton's Law is within 10%.

5-3. Creep Experiment

In a creep experiment, $(\Pi_{zz}-\Pi_{rr})$ needs to be held constant throughout the course of experiment. Experimentally, this requires the generation of a signal which is proportional to $(\Pi_{zz}-\Pi_{rr})$ and to feed such a signal back into the comparator along with a constant signal from the function generator. According to Equation (2-4-13), to generate a signal which is proportional to $(\Pi_{zz}-\Pi_{rr})$ requires the knowledges of the instantaneous rotational speed ω, drop diameter D and $K(3e^{3/2\gamma})$. The knowledges of instantaneous ω and D can be obtained handily from the output signals of the tachometer and the quadratic inverter. However, to obtain a signal like $3e^{3\gamma/2}$ requires a more sophisticated electronic device, particularly, a device which can perform the function of division, logarithm and anti-

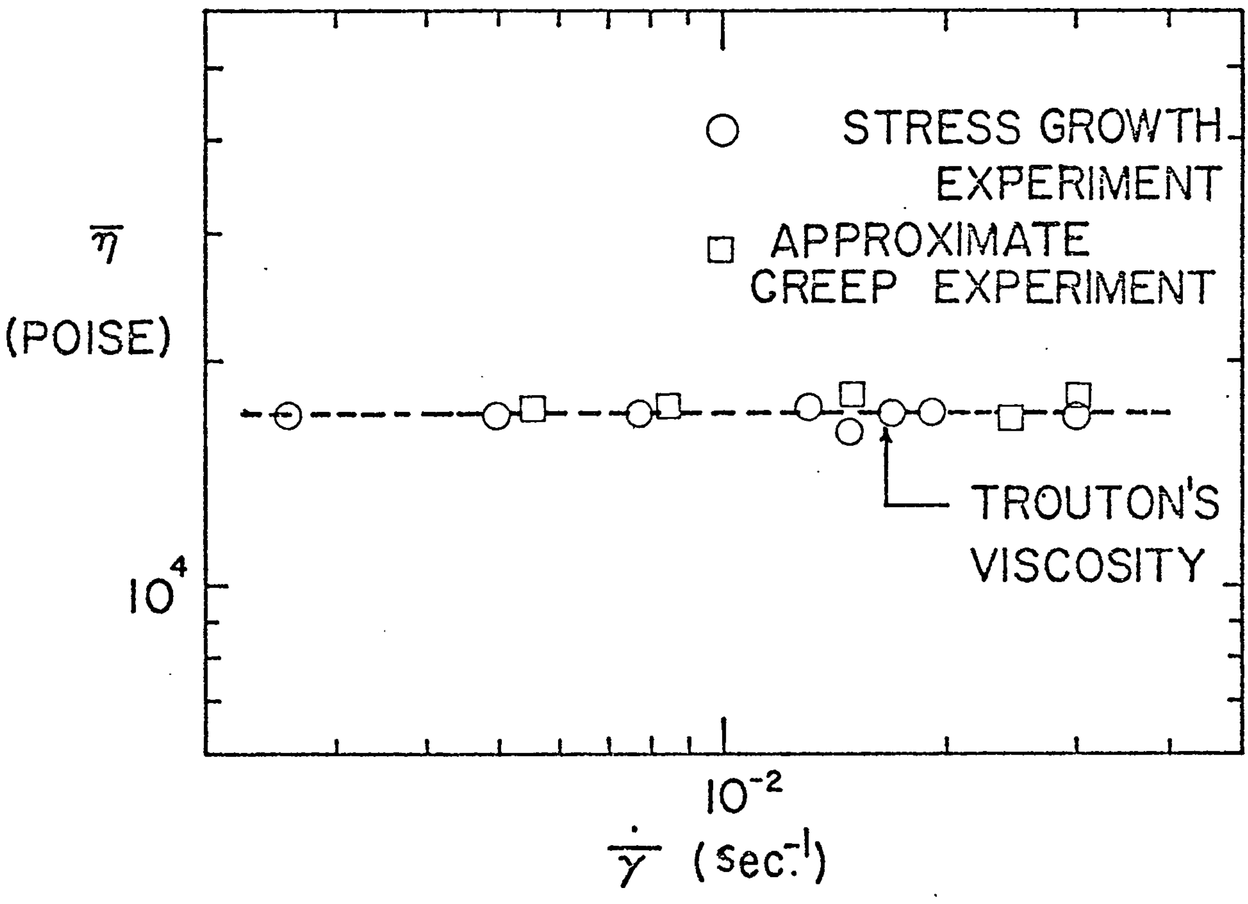

Figure 5-7 Steady Extensional Viscosity Data for Cannon ASTM Standard Oil at 25°C

logarithm together.

Considering the difficulty of finding an electronic device for generating the signal $\left(3e^{3\gamma/2}\right)$, it would appear that an exact creep experiment is not possible if Equation (2-4-13) is used for $\left(\Pi_{zz}-\Pi_{rr}\right)$. To this end, only approximate creep experiments in which (ωD) was held fixed were carried out in the present work. It is believed that an approximate constant extensional stress can be obtained when (ωD) is sufficiently large so that the percentage of variation in the extensional stress due to the interfacial tension effect is small. The experimental procedures for such an approximate creep experiment are described in the following section.

5-3-1. Experimental Procedures

The experimental procedures of the approximate creep experiment are very similar to those of the stress growth experiment. A drop (about 6.5 cm^3) of the silicone oil was introduced into the glass cylinder filled with continuous phase fluid.

The quadratic inverter and the tachometer were connected to a multiplier. Initially, the rotating cylinder system was turned on at a speed ω and the drop was allowed to reach its equilibrium shape. The temperature was controlled at 25°C.

After t=0, the signal from the multiplier was fed back into the comparator along with a prescribed constant signal from the function generator, the drop was then extended under the condition of $(\dot{\omega}D)$ = constant. In this experiment, the quadratic inverter was connected to a logarithmic amplifier. Both the signals from the logarithmic amplifier and the multiplier were recorded as a function of time throughout the course of experiment.

5-3-2. Experimental Results

Typical recorded signals of the logarithmic amplifier and the multiplier are shown in Fig. 5-8. Similar to those of the stress growth experiment, the output signal from the logarithmic amplifier wiggles because of the noise existing in the signal generated from the photomultiplier tube. The percentage of the amplitude of oscillation is about 1.5%. A linear portion of the signal from the logarithmic amplifier versus time was observed approximately one second after the voltage signal of the multiplier was controlled to change from 0.6 volt to 1.325 volt (96.8 dyne/cm^2 to 472 dyne/cm^2). This one second delay is probably due to the inertial effects being important in the initial period of drop elongation.

With the recorded signals from the logarithmic amplifier and the multiplier, the corresponding extensional strain $\bar{\gamma}$, the resulting stress ($\Pi_{zz} - \Pi_{rr}$) and the extension rate $\dot{\bar{\gamma}}$ were obtained using the same procedures described in the stress growth experiment. The time-dependent response of the extensional stress ($\Pi_{zz} - \Pi_{rr}$) and the extensional strain $\bar{\gamma}$ are shown in Fig. 5-9. Because of the inertial effects being important in the initial few seconds and the approximate

APPROXIMATE CREEP EXPERIMENT

From the multiplier

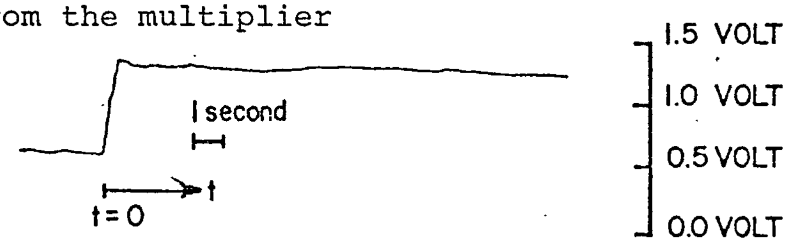

From the logarithmic amplifier

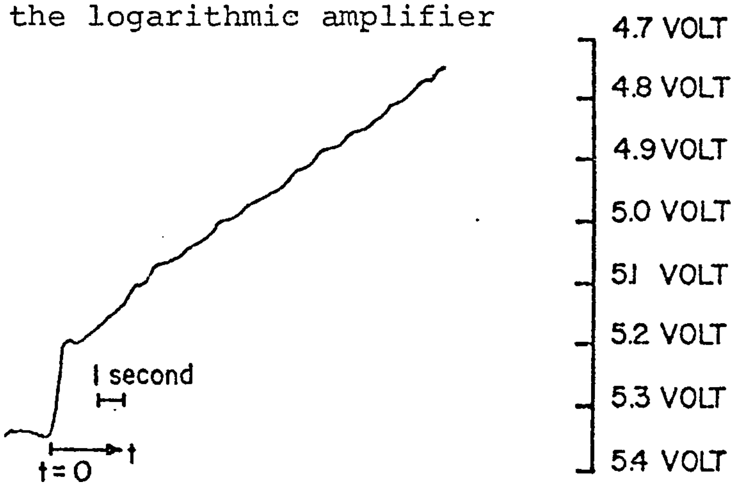

Figure 5-8 The Output Signals from the Logarithmic Amplifier and the Multiplier in the Approximate Creep Experiment with Cannon ASTM Viscosity Standard Oil

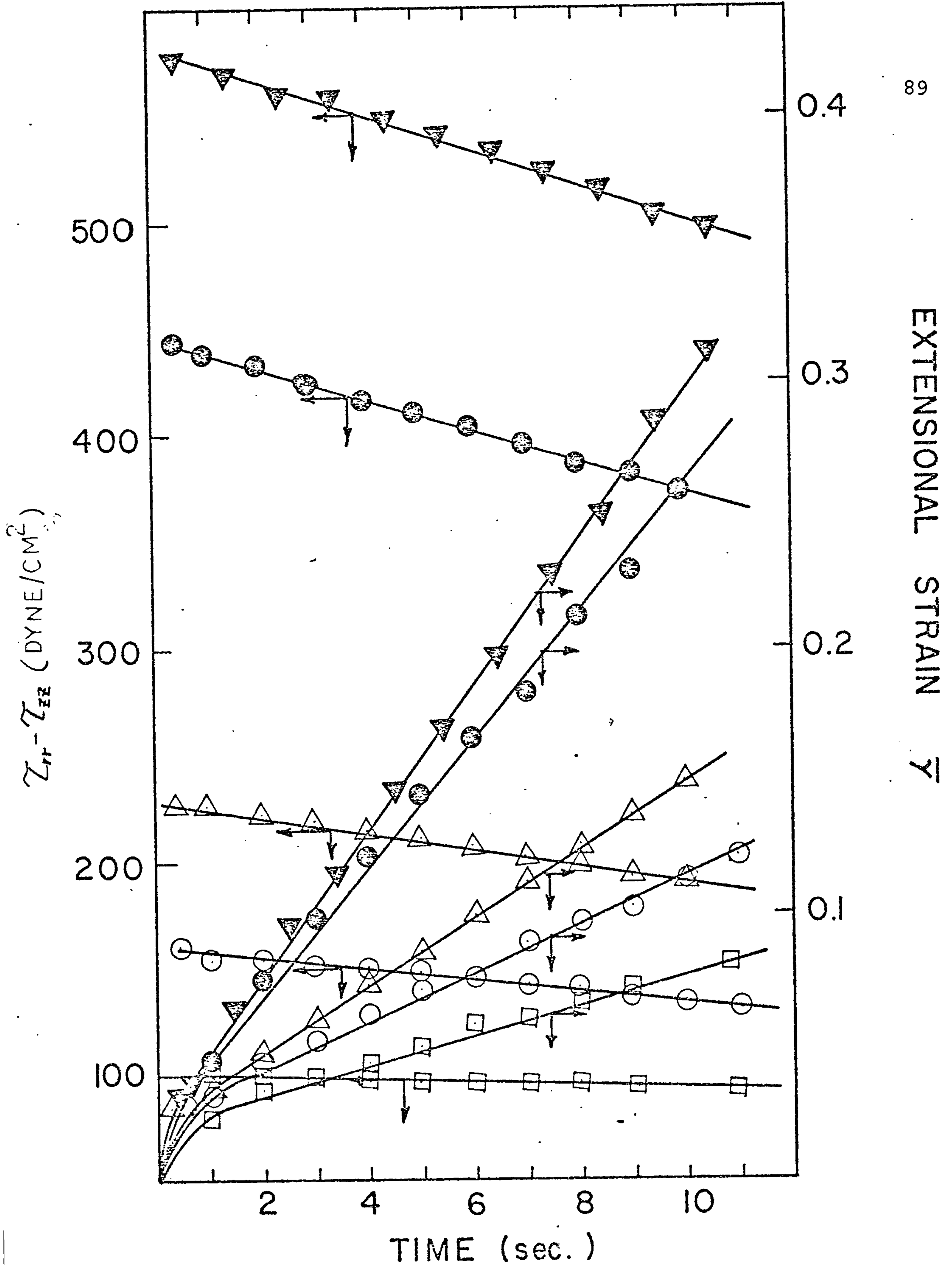

Figure 5-9 Strain and Corresponding Stress vs. Time for Approximate Creep Experiments (ω D=constant) with Cannon ASTM Viscosity Standard Oil

nature of the creep experiment performed, one notes an initial nonlinear portion followed by linear behavior in the curves of the extensional strain $\bar{\gamma}$ versus time. In general, the linear behavior of the extensional strain $\bar{\gamma}$ versus time is reached in a time period less than one second.

As shown in Fig. 5-9, due to the variation in $\frac{\sigma}{R}(1-3e^{\frac{3}{2}\bar{\gamma}})$ throughout the course of experiment, the resulting extensional stress in the constant (ωD) experiment is only approximately constant. The percentage of the maximum variation in the extensional stress is 17%. The instantaneous viscosity $\bar{\eta}^{+}$ was calculated according to Equation (5-2-7). The extension rate was taken as the slope of the linear portion in the curve of the extensional strain versus time. The results of $\bar{\eta}^{+}$ for several constant (ωD) experiments are shown in Fig. 5-10. Because the extensional stress in constant (ωD) experiment decreased with respect to time, $\bar{\eta}^{+}$ decreased throughout the course of experiment. The steady extensional viscosity was taken as the average value of $\bar{\eta}^{+}$ after the first second of the approximate creep experiment. As shown in Fig. 5-7, the results of the extensional viscosity satisfy the Trouton's law within 10%.

5-4. Comments on the Drop Elongation Apparatus

From the experimental experiences in testing the drop elongation apparatus, several conclusions about the versatilities

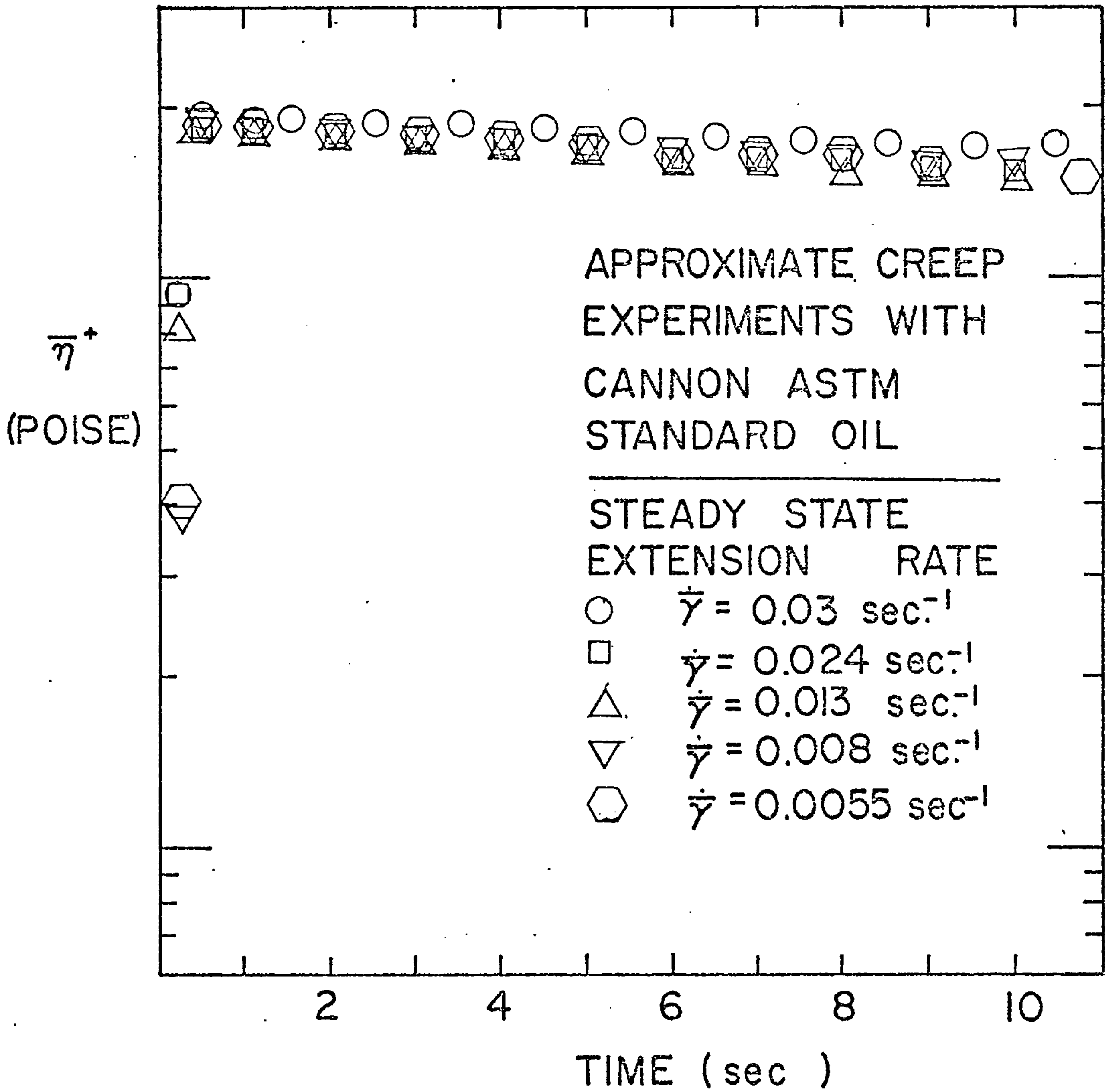

Figure 5-10 Instantaneous Extensional Viscosity Data for the Approximate Creep Experiments with Cannon ASTM Viscosity Standard Oil

of the present drop elongation apparatus can be drawn.

(1) Because of the experimental difficulties described in Section 4-4, only stress growth and creep experiments are possible with the apparatus.

(2) Due to the difficulties of generating an instantaneous curvature signal $(3e^{\frac{3}{2}\bar{\gamma}})$, only approximate creep experiment in which (ωD) is held constant can be carried out.

(3) The prescribed response of (ωD) in approximate creep experiment and D in the stress growth experiment were reached in a time period less than one second using the present control system. As a comparison, the behavior of (ωD) in approximate creep experiment was better controlled than that of D in the stress growth experiment.

(4) The results for the extensional viscosity obtained both from approximate creep experiments and the stress growth experiments are in good agreement with Trouton's Law. This, again, validates the analysis in Section 2-4.

Additional experiments such as the drop diameter decreasing linearly with time ($-\frac{dD}{dt}$ = constant), the rotational speed ω of the system following a prescribed manner, $\omega(t)$, etc. are also possible with the drop elongation apparatus. However, the extension rate and the extensional stress are both functions of time in those experiments. The use of such data in evaluating viscoelastic theories involves tedius numerical calculations and is to be avoided if possible. Hence, unless some revisions are made on the drop elongation apparatus; particularly, the control system, the present apparatus can be used in the stress growth and approximate creep experiments only.

CHAPTER VI

EXTENSIONAL FLOW MEASUREMENTS ON VISCOELASTIC POLYMER SOLUTIONS

6-1. Fluids

Table 6-1 shows the properties of the fluid systems used in the extensional flow studies. A 10% polyisobutylene in Decalin (PIB) and a 2.8% polyacrylamide (marketed by Dow Chemical Co. as Separan AP 30) in 1:1 mixture by weight of glycerol-water solutions (PAA) were used as the drop phases. The polyisobutylene was manufactured by Exxon Chemical Co. under the trade name Vistanex MM L-100, and had a viscosity average molecular weight of 1.2×10^6 (Flory). The molecular weight of polyacrylamide is unknown. Glycerol-water solutions and a 4% by weight polystyrene in tetrachloroethylene were used as the continuous phases. The addition of polystyrene into tetrachloroethylene was for the purpose of increasing the viscosity of this continuous phase while maintaining the high density characteristics of tetrachloroethylene solvent. The resulting viscosity of 4% by weight polystyrene in tetrachloroethylene solutions at $25^\circ \pm 0.1^\circ$C was 1.27 poise which is required for validating the rigid body rotation assumption (8) made in Section 2-4. The densities of the fluids were measured by weighting the samples in a 10 c.c. pycnometer on an electrical balance. The interfacial tensions were obtained using the rotating drop method. (11).

Table 6-1 Properties of the Polymer Solutions Used in the Experimental Studies (at 25°C)

Continuous Phase	Disperse Phase	Density: Continuous Phase (g/cm^3)	Density: Disperse Phase (g/cm^3)	Interfacial Tension (dyne/cm)	Zero Shear Visc.: Continuous Phase (poise)	Zero Shear Visc.: Disperse Phase (poise)
Glycerol-water solution	10% poly-isobutylene in Decalin (PIB)	1.21	0.901	11	1.01	7000
4% polystyrene in tetra-chloroethylene	PAA*	1.573	1.137	7.5	1.27	9700

PAA*- 2.8% polyacrylamide(Separan AP 30) in 50:50 glycerol-water

6-2. Characterization

In order to characterize the rheological properties of the disperse phase fluids, viscosity, normal force, and small amplitude oscillatory measurements were performed using the Weissenberg Rheogoniometer with the temperture controlled at 25°C. The details of those measurements are described elsewhere (76). In the oscillatory testing, a simple harmonic input of shear rate, with a certain frequency, amplitude, and phase, produces a simple harmonic output of shear stress with the same frequency, but different amplitude and phase. The dynamic viscosity η' and dynamic rigidity G' (18), which characterize the material response under these conditions are obtained in terms of the amplitude ratio A and the phase difference Φ between the shear stress (output) and shear rate (input). The measurements of viscosity η and normal force $-(\tau_{xx}-\tau_{yy})$ at different shear rates $\dot{\gamma}$, and η' and G' at different frequencies ω provide the basis for evaluating the rheological parameters in various viscoelastic models.

The viscoelastic properties of the polymer solutions PIB and PAA were characterized both by the truncated Goddard expansion (13) and Bird-Carreau model (12). The truncated Goddard expansion is a special case of the corotating memory integral expansion developed by Goddard (82). For assuring there is no unwanted dependence on local rigid body rotation, this corotating rheological model is developed by using a reference frame which is moving with the fluid and rotating with the local angular velocity. By further assuming that the stress for any isotropic viscoelastic fluid at a particular particle depends only on the deformation history of that particle and not on that of adjacent particle, Goddard obtained the stress tensor as a memory integral expansion of the following form:

$$\underset{\sim}{\tau} = \int_{\infty}^{t} G_I(t-t')\dot{\underset{\sim}{\Gamma}}'dt' - \frac{1}{2}\int_{-\infty}^{t}\int_{\infty}^{t} G_{II}(t-t',t-t'')\left[\dot{\underset{\sim}{\Gamma}}'\cdot\dot{\underset{\sim}{\Gamma}}'' + \dot{\underset{\sim}{\Gamma}}''\cdot\dot{\underset{\sim}{\Gamma}}'\right]dt''dt'$$
$$-\frac{1}{2}\int_{-\infty}^{t}\int_{-\infty}^{t}\int_{\infty}^{t}\left\{2G_{III}(t-t',t-t'',t-t''')\left[\dot{\underset{\sim}{\Gamma}}'\dot{\underset{\sim}{\Gamma}}'':\dot{\underset{\sim}{\Gamma}}'''\right] + G_{IV}(t-t',t-t'',t-t''')\left[\dot{\underset{\sim}{\Gamma}}'\cdot\dot{\underset{\sim}{\Gamma}}''\cdot\dot{\Gamma}''' + \dot{\underset{\sim}{\Gamma}}'''\cdot\dot{\underset{\sim}{\Gamma}}''\cdot\dot{\underset{\sim}{\Gamma}}'\right]dt'''dt''dt' \qquad (6\text{-}2\text{-}1)$$

in which $\dot{\underset{\sim}{\Gamma}}' \equiv \dot{\underset{\sim}{\Gamma}}(t,t')$ and $\dot{\underset{\sim}{\Gamma}}$ is defined as the corotating rate of deformation tensor . The kernel function $G_I(t-t')$ is identical to the relaxation modulus in linear viscoelasticity (18,20) and can be obtained from the linear viscoelastic properties of the fluid. However, there has been no experimental program to determine G_{II}, G_{III}, and G_{IV}. To this end, based on the information available from kinetic theory (77), Bird et. al. (13) set G_{II}, G_{III}, and G_{IV} as

$$G_{II}(t-t',t-t'') = b\,g(t,t')\,G_I(t-t') \qquad (6\text{-}2\text{-}2)$$

$$G_{III}(t-t',t-t'',t-t''') = 0 \qquad (6\text{-}2\text{-}3)$$

$$G_{IV}(t-t',t-t'',t-t''') = \frac{c}{2}\left[g(t''',t',t'')G_I(t-t') + g(t',t'',t''')\,G_I(t-t')\right] \qquad (6\text{-}2\text{-}4)$$

where b and c are constant characteristics of the fluid, and $g(t',t'',t''')$ is defined as

$$g(t',t'',t''') = 1 \qquad \text{for } -\infty < t''' \le t'' \le t' \qquad (6\text{-}2\text{-}5)$$
$$= 0 \qquad \text{otherwise}$$

Combination of Equation (6-2-1) to (6-2-5) yields the truncated Goddard expansion

$$\underset{\sim}{\tau} = -\int_{-\infty}^{t} G_I(t-t')\dot{\underset{\sim}{\Gamma}}' dt' - \frac{b}{2}\int_{-\infty}^{t} G_I(t-t')\left[\int_{t'}^{t}(\dot{\underset{\sim}{\Gamma}}'\cdot\dot{\underset{\sim}{\Gamma}}'' + \dot{\underset{\sim}{\Gamma}}''\cdot\dot{\underset{\sim}{\Gamma}}')dt''\right]dt'$$
$$-\frac{c}{4}\int_{-\infty}^{t} G_I(t-t')\left[\int_{t'}^{t}\int_{t'}^{t} \dot{\underset{\sim}{\Gamma}}''\cdot\dot{\underset{\sim}{\Gamma}}'\cdot\dot{\underset{\sim}{\Gamma}}''' dt''' dt'' + \int_{t'}^{t}\int_{t'}^{t''} \dot{\underset{\sim}{\Gamma}}''\cdot\dot{\underset{\sim}{\Gamma}}'''\cdot\dot{\underset{\sim}{\Gamma}}' dt''' dt'' \right. \tag{6-2-6}$$
$$\left. + \int_{t'}^{t}\int_{t'}^{t'''} \dot{\underset{\sim}{\Gamma}}'\cdot\dot{\underset{\sim}{\Gamma}}'''\cdot\dot{\underset{\sim}{\Gamma}}'' dt'' dt'''\right] dt'$$

For steady state shearing flow and small amplitude oscillatory motion, Equation (6-2-6) gives

$$\eta = \int_0^\infty G_I(s)\left[\cos\dot{\gamma}s + \frac{1}{2}c\dot{\gamma}s\sin\dot{\gamma}s\right] ds \tag{6-2-7}$$

$$-(\tau_{xx}-\tau_{yy}) = 2\int_0^\infty G_I(s)\left[\dot{\gamma}\sin\dot{\gamma}s + \frac{c}{2}(\sin\dot{\gamma}s - \dot{\gamma}s\cos\dot{\gamma}s)\right]ds \tag{6-2-8}$$

$$\eta' = \int_0^\infty G_I(s)\cos\omega s\, ds \tag{6-2-9}$$

$$G' = \int_0^\infty G_I(s)\,\omega\sin\omega s\, ds \tag{6-2-10}$$

The constant b in the steady state shearing flow is approximately equal to

$$b = \frac{2\beta}{\theta} + 1 \tag{6-2-11}$$

where $\bar{\theta}$ and β are the first and second normal stress coefficients, respectively.

For the purpose of characterizing the polymer solutions used in the present work, $G_I(s)$ was selected as

$$G_I(s) = \sum_{i=1}^{5} a_i\lambda_i e^{-s/\lambda_i} \tag{6-2-12}$$

which is the form used by Chang and Lodge (50) and Bird et. al. (13).

Substituting Equation (6-2-12) into Equations (6-2-7) to (6-2-10), it follows that

$$\eta = \sum_{i=1}^{5}\frac{a_i\lambda_i^2}{(1+\lambda_i^2\dot{\gamma}^2)^2}\left(1+(1+c)\lambda_i^2\dot{\gamma}^2\right) \tag{6-2-13}$$

$$-(\tau_{xx}-\tau_{yy}) = \sum_{i=1}^{5} \frac{2a_i\lambda_i^3\dot{\gamma}^2}{(1+\lambda_i^2\dot{\gamma}^2)}\left(1+(1+c)\lambda_i^2\dot{\gamma}^2\right) \qquad (6\text{-}2\text{-}14)$$

$$\eta' = \sum_{i=1}^{5} \frac{a_i\lambda_i^2}{1+\lambda_i^2\omega^2} \qquad (6\text{-}2\text{-}15)$$

and

$$G' = \sum_{i=1}^{5} \frac{a_i\omega^2\lambda_i^3}{1+\lambda_i^2\omega^2} \qquad (6\text{-}2\text{-}16)$$

Equation (6-2-13) to (6-2-16) are the key equations for characterizing the viscometric flow properties of the drop phase fluids by the truncated Goddard expansion.

The Bird-Carreau model involves 5 parameters: a zero shear viscosity η_o, two time constant λ_1 and λ_2, and two slope parameters α_1 and α_2. The form of the constitutive equation in the Bird-Carreau theory is

$$\tau^{ij} = -\int_{-\infty}^{t} m(t-t', |\dot{\gamma}|)\left(\left(1+\frac{E}{2}\right)\bar{\Gamma}^{ij}(t') - \frac{E}{2} g^{ir}(x)\, g^{js}(x)\, \Gamma_{rs}(t')\right)dt' \qquad (6\text{-}2\text{-}17)$$

where

$$\bar{\Gamma}^{ij}(t') = -g^{ij}(x) + \left(\frac{\partial x^i}{\partial x'^m}\right)\left(\frac{\partial x^j}{\partial x'^n}\right) g^{mn}(x') \qquad (6\text{-}2\text{-}18)$$

$$\Gamma_{ij}(t') = g_{ij}(x) - \left(\frac{\partial x'^m}{\partial x^i}\right)\left(\frac{\partial x'^n}{\partial x^j}\right) g_{mn}(x') \qquad (6\text{-}2\text{-}19)$$

Here x and x' are the positions in space occupied by an element of fluid at times t and t' respectively, g_{ij} and g^{ij} are the respectively covariant and contravariant components of metric tensor. E is a constant defined as

$$E = 2\,\frac{\tau_{22}-\tau_{33}}{\tau_{11}-\tau_{22}} \qquad (6\text{-}2\text{-}20)$$

The memory function $m(t-t', |\dot{\gamma}(t')|)$ is

$$m(t-t', |\dot{\gamma}(t')|) = \sum_{p=1}^{\infty} \frac{\eta_p}{\lambda_{2p}^2}\, \frac{e^{-(t-t')/\lambda_{2p}}}{1+(\lambda_{1p}|\dot{\gamma}(t')|)^2} \qquad (6\text{-}2\text{-}21)$$

in which $|\dot{\gamma}|$ is equal to $\sqrt{\frac{1}{2}\sum_m\sum_n \dot{\gamma}_{mn}^2}$ and η_p, λ_{1p}, and λ_{2p} are defined in terms of the model parameters λ_1, λ_2, α_1, α_2, and η_o by:

$$\eta_p = \eta_o \frac{\lambda_{1p}}{\sum_{p=1}^{\infty}\lambda_{1p}}\ ; \quad \lambda_{1p} = \lambda_1\left(\frac{2}{p+1}\right)^{\alpha_1}\ ; \quad \lambda_{2p} = \lambda_2\left(\frac{2}{p+1}\right)^{\alpha_2} \qquad (6\text{-}2\text{-}22)$$

For steady state shearing flow and small amplitude oscillatory motion, the predictions of Bird-Carreau model for η, $-(\tau_{xx}-\tau_{yy})$, η', and G' are given elsewhere (12, 78).

$$\eta=\sum_{p=1}^{\infty}\frac{\eta_p}{1+(\lambda_{1p}\dot{\gamma})^2}\xrightarrow[\text{and use Equation (6-2-22)}]{\text{High }\dot{\gamma}}\frac{\pi\eta_0\,(2^{\alpha_1}\lambda_1\dot{\gamma})^{\frac{1-\alpha_1}{\alpha_1}}}{(Z(\alpha_1)-1)\,2\alpha_1\sin\left(\frac{1+\alpha_1}{2\alpha_1}\pi\right)} \qquad (6\text{-}2\text{-}23)$$

$$-(\tau_{xx}-\tau_{yy})=2\sum_{p=1}^{\infty}\frac{\eta_p\lambda_{2p}\dot{\gamma}^2}{1+(\lambda_{1p}\dot{\gamma})^2}\xrightarrow[\text{and use Equation (6-2-22)}]{\text{High }\dot{\gamma}}\frac{2^{\alpha_2+1}\lambda_2\pi\eta_0\dot{\gamma}^2\,(2^{\alpha_1}\lambda_1\dot{\gamma})^{\frac{1-\alpha_1-\alpha_2}{\alpha_1}}}{(Z(\alpha_1)-1)\,2\alpha_1\sin\left(\frac{1+\alpha_1-\alpha_2}{2\alpha_1}\pi\right)} \qquad (6\text{-}2\text{-}24)$$

$$\eta'=\sum_{p=1}^{\infty}\frac{\eta_p}{1+(\lambda_{1p}\omega)^2}\xrightarrow[\text{and use Equation (6-2-22)}]{\text{High }\omega}\frac{\pi\eta_0}{(Z(\alpha_1)-1)}\,\frac{(2^{\alpha_2}\lambda_2\omega)^{\frac{1-\alpha_1}{\alpha_2}}}{2\alpha_2\sin\left(\frac{1+2\alpha_2-\alpha_1}{2\alpha_2}\pi\right)} \qquad (6\text{-}2\text{-}25)$$

$$G'=\sum_{p=1}^{\infty}\frac{\eta_p\omega^2}{1+(\lambda_{1p}\omega)^2}\xrightarrow[\text{and use Equation (6-2-22)}]{\text{High }\omega}\frac{(2^{\alpha_2}\lambda_2\omega)^{\frac{1-\alpha_1-\alpha_2}{\alpha_2}}\cdot 2^{\alpha_2}\lambda_2\pi\eta_0\omega^2}{(Z(\alpha_1)-1)\cdot\left(2^{\alpha_2}\sin\left(\frac{1+\alpha_2-\alpha_1}{2\alpha_2}\pi\right)\right)} \qquad (6\text{-}2\text{-}26)$$

where $Z(\ \ )$ is the Riemann Zeta function.

With the experimental data of η, $-(\tau_{xx}-\tau_{yy})$, η', and G', Equation (6-2-13) to(6-2-16) and Equation (6-2-23) to (6-2-26) were used to evaluate the corresponding parameters in the truncated Goddard expansion and Bird-Carreau model. It should be noted that the shear rates obtainable on the Rheogoniometer were not sufficiently low to determine η_0. As a result, the zero shear viscosities of the polymer solutions were obtained by the falling ball technique (79). The parameters λ_1, λ_2, α_1, and α_2 in the Bird-Carreau model and c and a_i (i=1,...5) in the truncated Goddard expansion were then determined by a computer program commonly refered to as BSOLVE (80). This is a combined least squares and method of steepest descent analysis for determining parameters for nonlinear mathematical models.

Using BSOLVE, the η, $-(\tau_{xx}-\tau_{yy})$, η', and G' data were fitted simultaneously. Because the data of η and η' are relatively more accurate and reliable compared to the data of G' and $-(\tau_{xx}-\tau_{yy})$, the data of η, $-(\tau_{xx}-\tau_{yy})$, η', and G' were weighed according to the ratios 10:1:10:2 for both PIB and PAA.

In the case of determining the parameters in the truncated Goddard expansion, a set of values were specified for λ_i (i=1,...5). Then, the corresponding c and a_i (i=1..5) were obtained subject to the constraint

$$\sum_{i=1}^{5} a_i \lambda_i^2 = \eta_0 \qquad (6\text{-}2\text{-}27)$$

It is possible to determine all λ_i (i=1,...5), a_i (i=1,...5) and c by fitting the experimental data of η, $-(\tau_{xx}-\tau_{yy})$, η', and G'. However, the parameters λ_i (i=1,...5), a_i(i=1,...5), and c obtained from this kind of fit would be somewhat insensitive to the η, $-(\tau_{xx}-\tau_{yy})$, η', and G' data, i.e., many sets of parameter values would give approximately the same accuracy of fit. Hence the specification of λ_i values does not appear to be a serious limitation. It should be noted that the values for λ_i(i=1,...5) were picked in the same way as used by Chang and Lodge (50).

The parameters in the Bird-Carreau model and truncated Goddard expansion for PIB and PAA are listed in Table 6-2. The values of $\frac{\alpha_2}{\alpha_1}$ and $\frac{\lambda_1}{\lambda_2}$ are in good agreement with those obtained by Carreau et. al. (78). The experimental data of η, $-(\tau_{xx}-\tau_{yy})$, η', and G' along with the corresponding model predictions were plotted in Fig. 6-1 for PIB and Fig. 6-2 for PAA. Except for the $-(\tau_{xx}-\tau_{yy})$ and G' data, it seems that both models describe the experimental data quite well. Since the data of $-(\tau_{xx}-\tau_{yy})$ and G' were placed low weight in the fitting, it is not a surprise that both models describe the $-(\tau_{xx}-\tau_{yy})$ and G' data

Table 6-2 Model Parameters Determined with Viscometric Flow Data

Solutions	Bird-Carreau Model							Truncated Goddard Expansion										
	η_0	λ_1	λ_2	α_1	α_2	λ_1/λ_2	α_2/α_1	λ_1	λ_2	λ_3	λ_4	λ_5	a_1	a_2	a_3	a_4	a_5	c
PIB*	7000	12.2	12.4	1.35	1.1	0.98	0.8	10	1	0.1	0.01	0.001	31	1990	112000	6.1×10^6	1.0×10^8	1.22
PAA**	9700	47.4	70.7	3.45	2.98	0.7	0.86	50	5	0.5	0.05	0.005	3.4	41	7000	13000	3.9×10^5	2.28

PIB* - 10 % polyisobutylene in Decalin

PAA** - 2.8% polyacrylamide in 1:1 mixture by weight of glycerol-water solutions

Figure 6-1 Viscosity, Normal Stress Difference, Dynamic Viscosity, and Dynamic Rigity for PIB

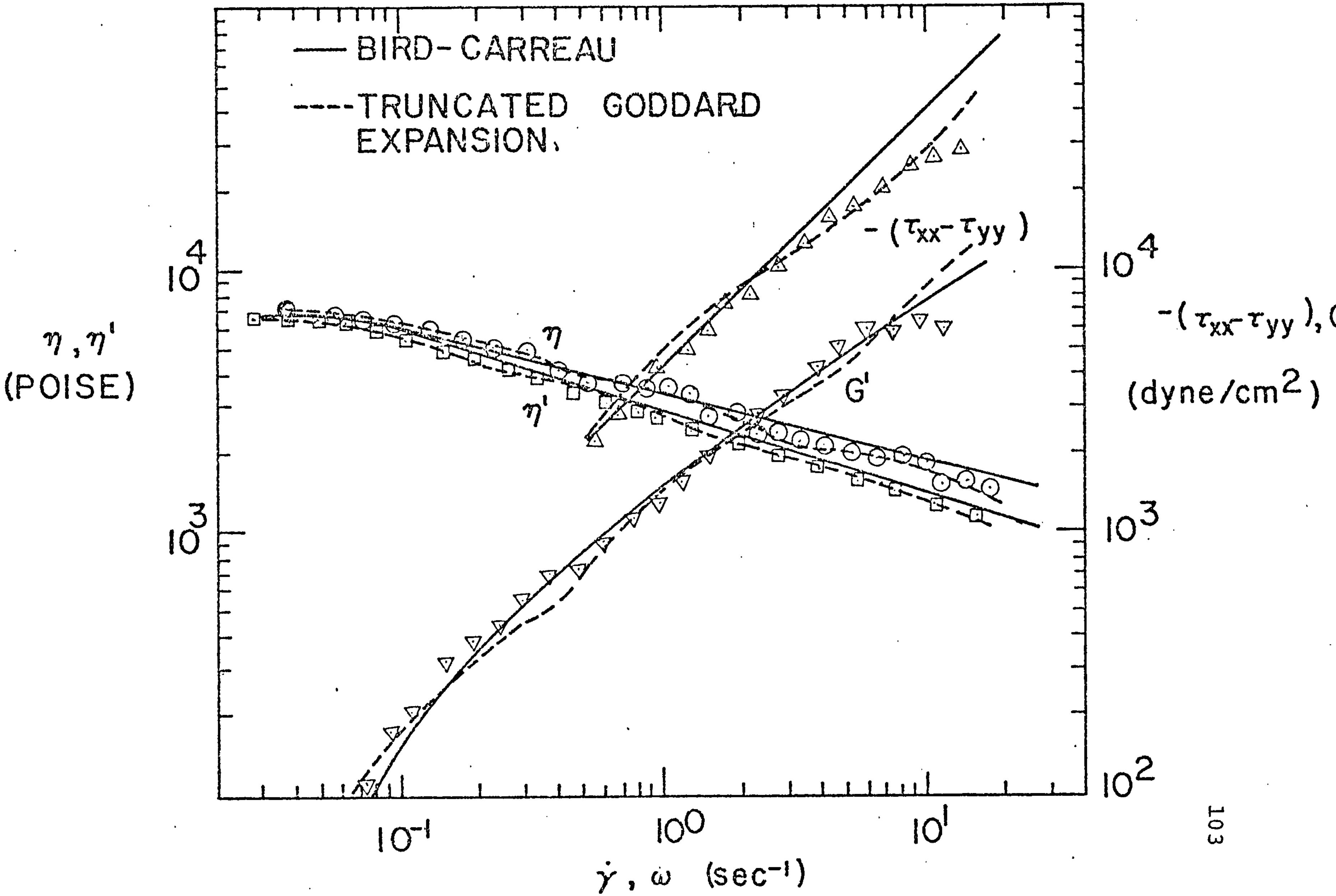

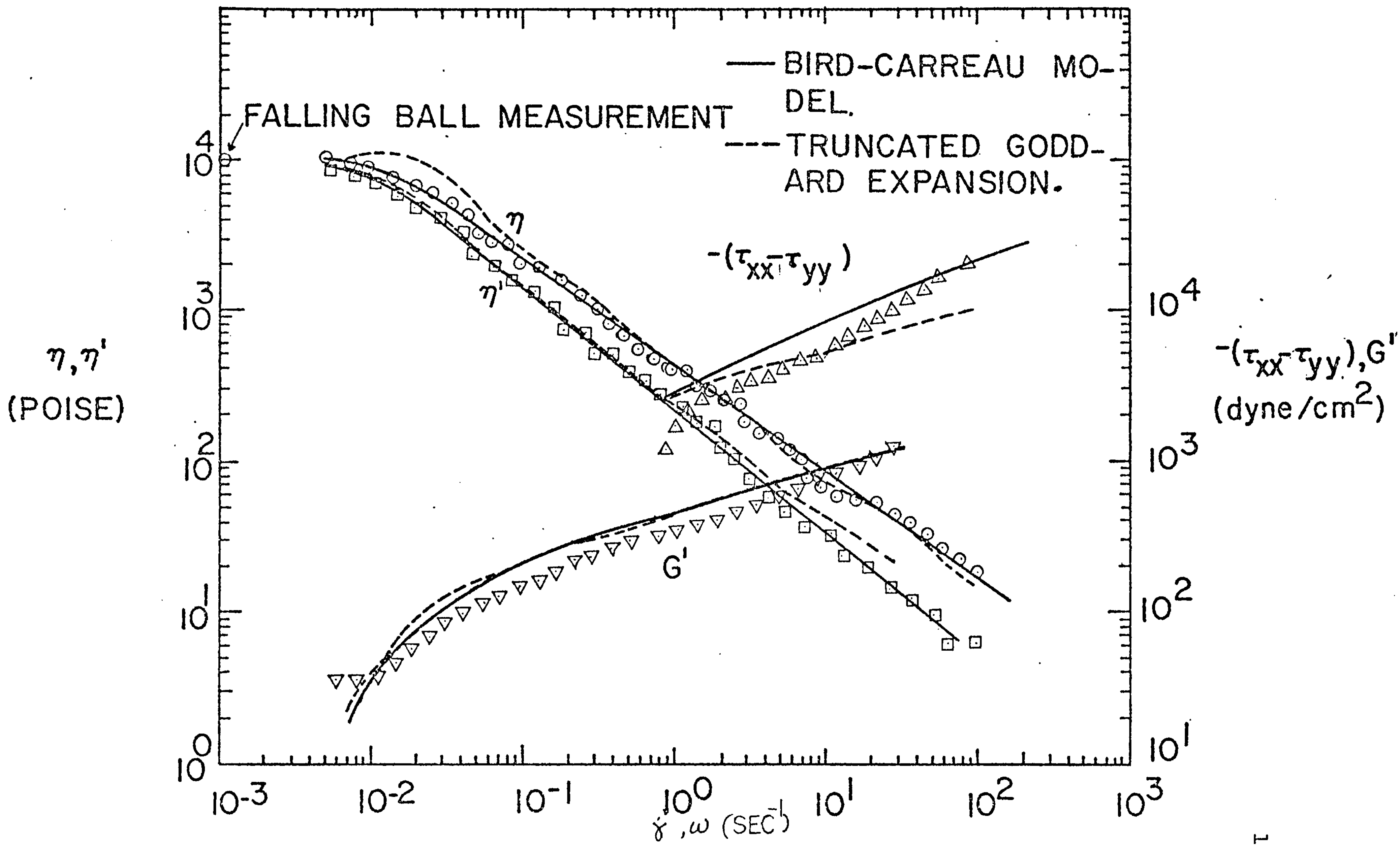

Figure 6-2 Viscosity, Normal Stress Difference, Dynamic Viscosity, and Dynamic Rigidity for PAA

poorly as shown in Figs. 6-1 and 6-2. A better agreement between the data of $-(\tau_{xx}-\tau_{yy})$ and G' and the corresponding model predictions can be achieved by placing more weight on the $-(\tau_{xx}-\tau_{yy})$ and G' data in the computer fitting. However, such a fitting would result a poor fit of the η and η' data, and hence was avoided in the present work.

As shown in Fig. 6-1 and 6-2, the predictions of η, $-(\tau_{xx}-\tau_{yy})$, η', and G' from the truncated Goddard expansion oscillate. The oscillatory behavior in the predictions of the truncated Goddard expansion is due to the truncated characteristic in the form used for G_I.

6-3. Experiments Conducted

Both PIB and PAA were tested in the stress growth and approximate creep experiments. The experimental procedures of the stress growth and approximate creep experiments with PIB and PAA are the same as those for silicone oil described in Section 5-2 and 5-3.

A fluid drop of interest (PIB and PAA) was introduced into the rotating glass cylinder filled with the corresponding continuous phase (glycerol-water solutions for PIB and 4% by weight polystyrene in tetrachloroethylene solutions for PAA). The system was then activated to a speed ω and the drop was allowed to reach its equilibrium shape. The temperature inside the chamber was controlled at 25 °C.

In the case of stress growth experiment, the output signal ($10 \log_{10} S_D$) of the logarithmic amplifier was instantaneously fed back into the comparator along with a linear signal from the function generator. For the case of approximate creep experiment, the output signal $\left(\frac{\omega_T S_D}{10}\right)$ from the multiplier was fed back to the comparator along with a constant signal from the function generator. For both stress growth and approximate creep experiments, the signals from the multiplier and the logarithmic amplifier were recorded as a function of time throughout the course of experiment.

It should be noted that in order to minimize effects of changes in material properties of PIB and PAA, both the viscometric and extensional flow experiments for each of the polymer solutions PIB and PAA were conducted within a two week period.

6-4. Experimental Results

6-4-1. Observed Behavior

Fig. 6-3 to Fig. 6-6 show typical experimentally recorded signals of the logarithmic amplifier and multiplier for PAA and PIB in both stress growth and approximate creep experiments. Due to the same reasons explained in the silicone oil case, the noise generated in the photomultiplier tube caused the signal of the logarithmic amplifier to wiggle throughout the period of experiments. The percentage of the amplitude of oscillation to the changes due to drop elongation is 3% for PIB and 4% for PAA.

STRESS GROWTH EXPERIMENT

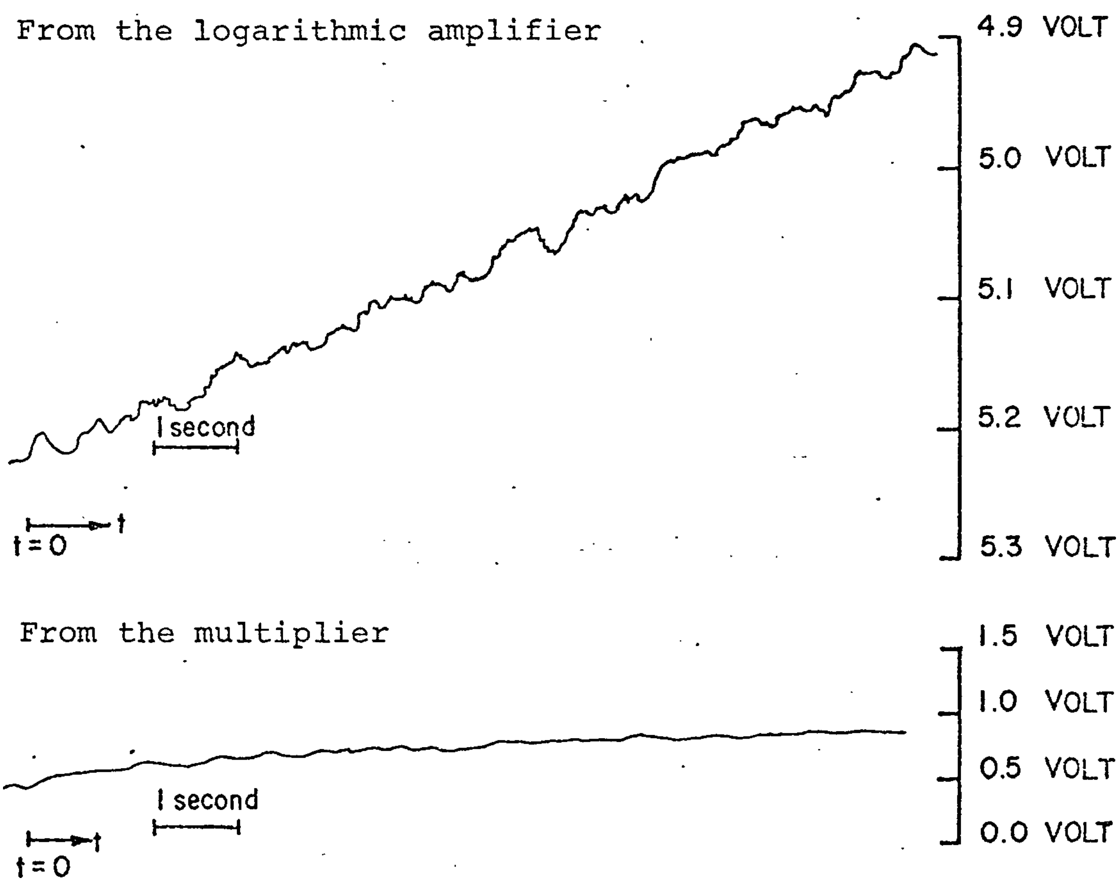

Figure 6-3 The output Signals from the Logarithmic Amplifier and the Multiplier in the Stress Growth Experiment with PAA

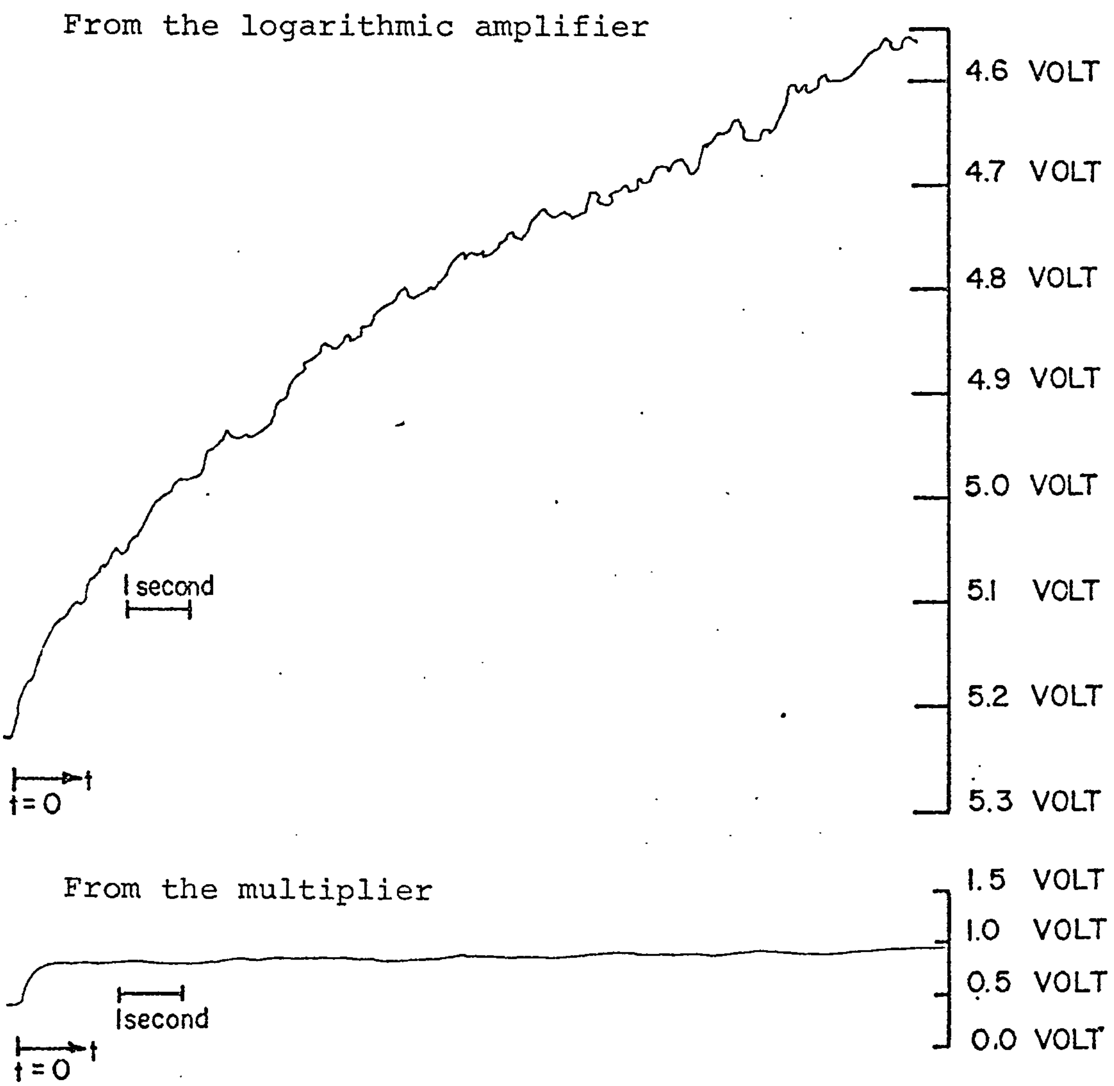

Figure 6-4 The Output Signals from the Logarithmic Amplifier and the Multiplier in the Approximate Creep Experiment with PAA

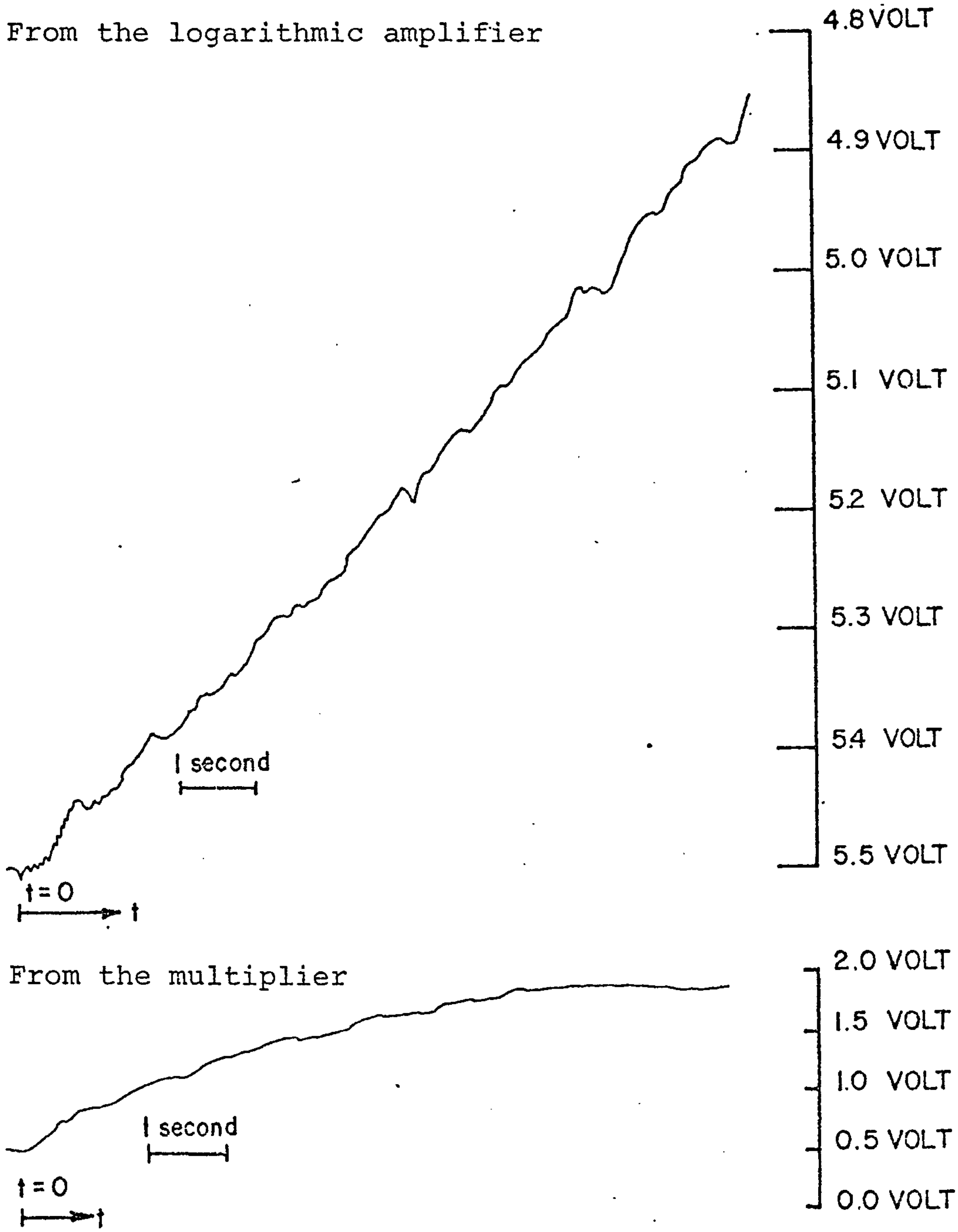

Figure 6-5 The Output Signals from the Logarithmic Amplifier and the Multiplier in the Stress Growth Experiment with PIB

From the logarithmic amplifier

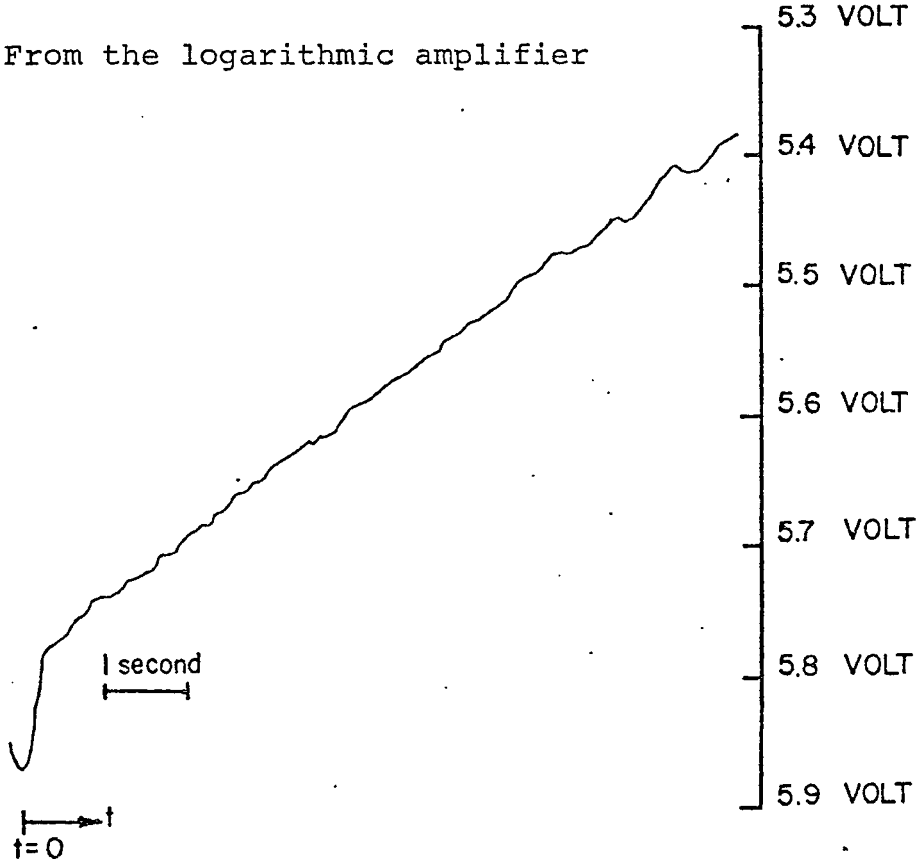

From the multiplier

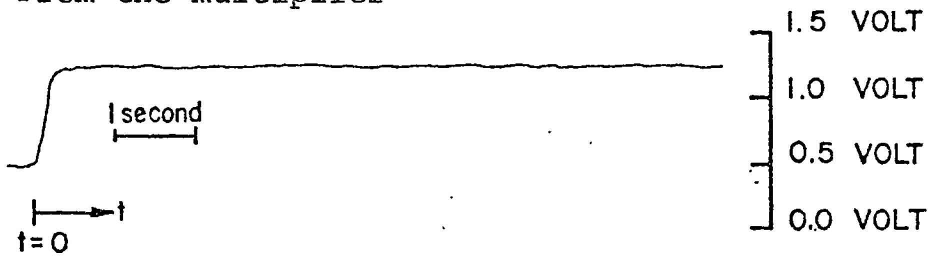

Figure 6-6 The Output Signals from the Logarithmic Amplifier and the Multiplier in the Approximate Creep Experiment with PIB

The calibration curves of S_D vs D and S_V vs D for PAA and PIB are shown in Fig. 6-7 and 6-8 respectively. Using the linear relation between S_D and D, the signals from the logarithmic amplifier and multiplier were converted to D and (ωD).

Based on the data of D and (ωD), the extensional strain $\bar{\gamma}$, the dimensionless curvature K and the extensional stress $(\Pi_{zz}-\Pi_{rr})$ were calculated from the respective Equations (5-2-5), (4-2-10) and (2-4-13). The extension rate $\dot{\bar{\gamma}}$ in both stress growth and approximate creep experiments was obtained from the slope of the recorded logarithmic amplifier signal according to Equation (5-2-6). Then, $\bar{\eta}^+$ was calculated from Equation (5-2-7).

The data of $\bar{\eta}^+$ for PAA and PIB in the stress growth experiment are shown in Fig. 6-9 and 6-10 respectively while the experimental results of the extensional stress and the corresponding extensional strain in the approximate creep experiment are plotted in Fig. 6-11 for PAA and Fig. 6-12 for PIB. As indicated in Table 6-2, PAA has a larger relaxation time λ_2 in the Bird-Carreau model than PIB. Hence, in the stress growth experiment, the steady extensional viscosity for PIB was reached within a shorter period of time (about 10 seconds) than that for PAA (about 16 seconds) at the same extension rate. Also, as shown in Fig. 6-11 and 6-12 for the approximate creep experiment, the extensional strain of PIB reaches steady state (strain rate is constant or strain increases linearly with time) earlier than does PAA at the same imposed stress level.

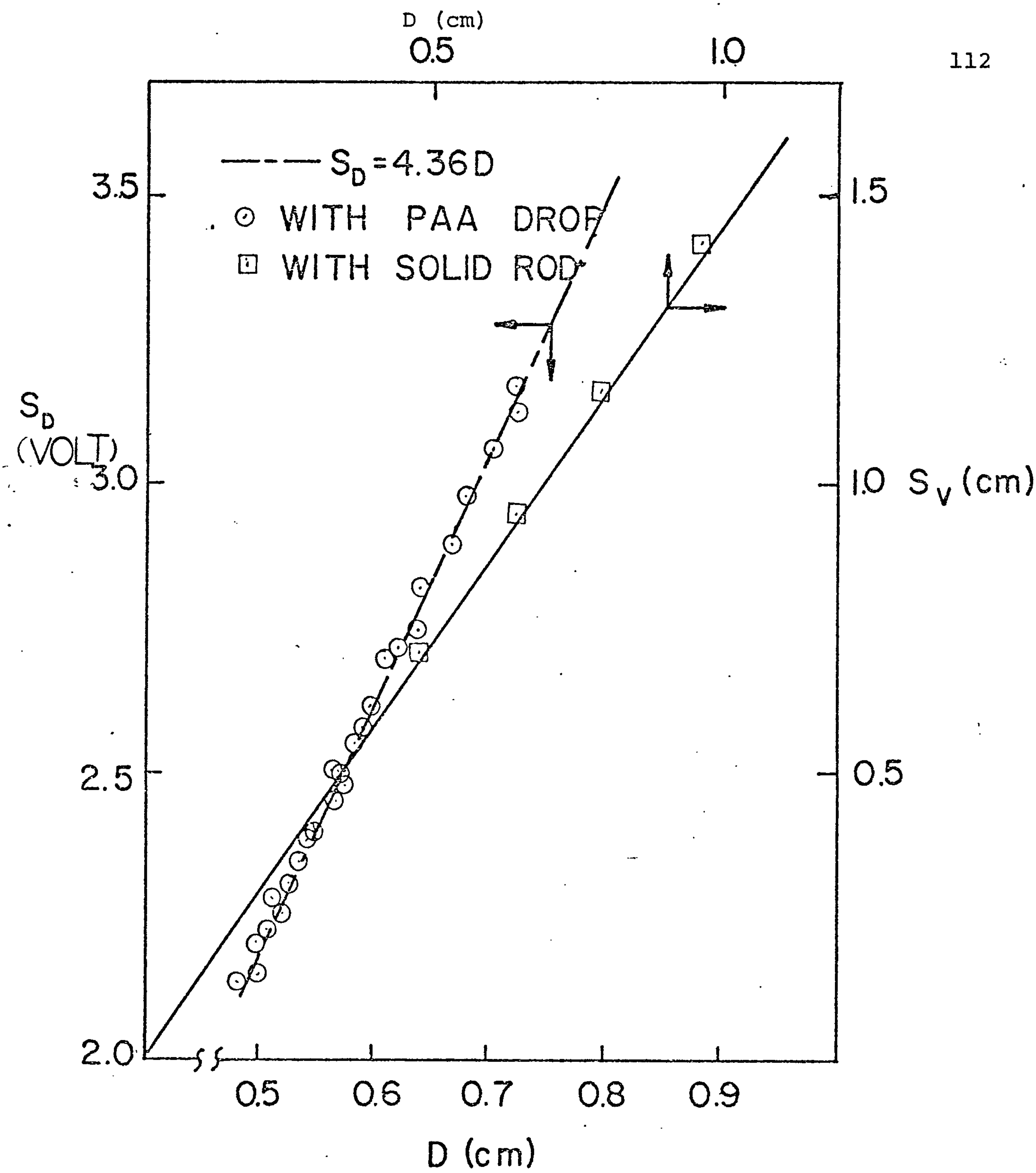

Figure 6-7 Calibration Curves for the Output Signal S_D from the Quadratic Inverter vs. Drop Diameter -PAA

Figure 6-8 Calibration Curves for the Output Signal S_D from the Quadratic Inverter vs. Drop Diameter- PIB

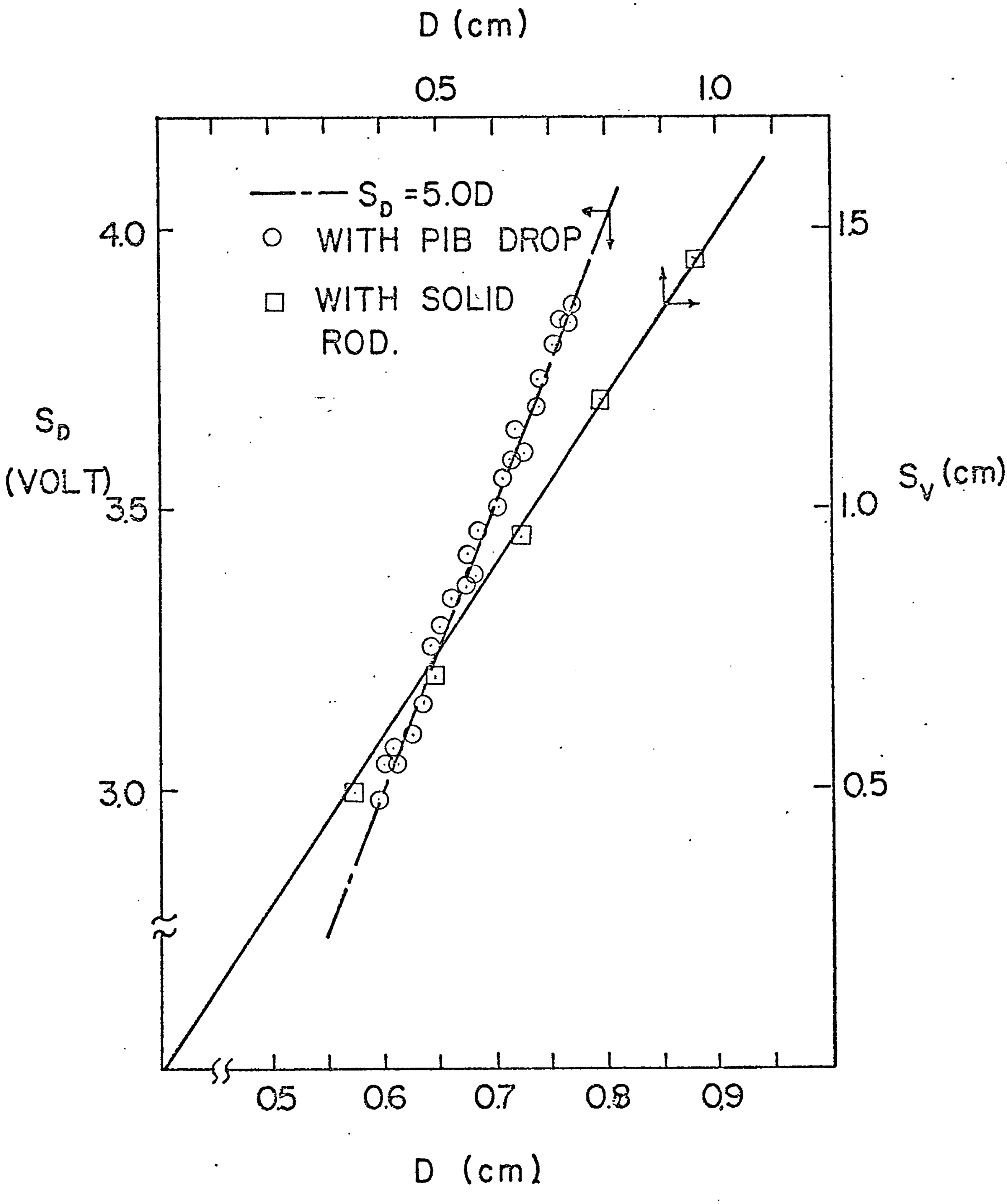

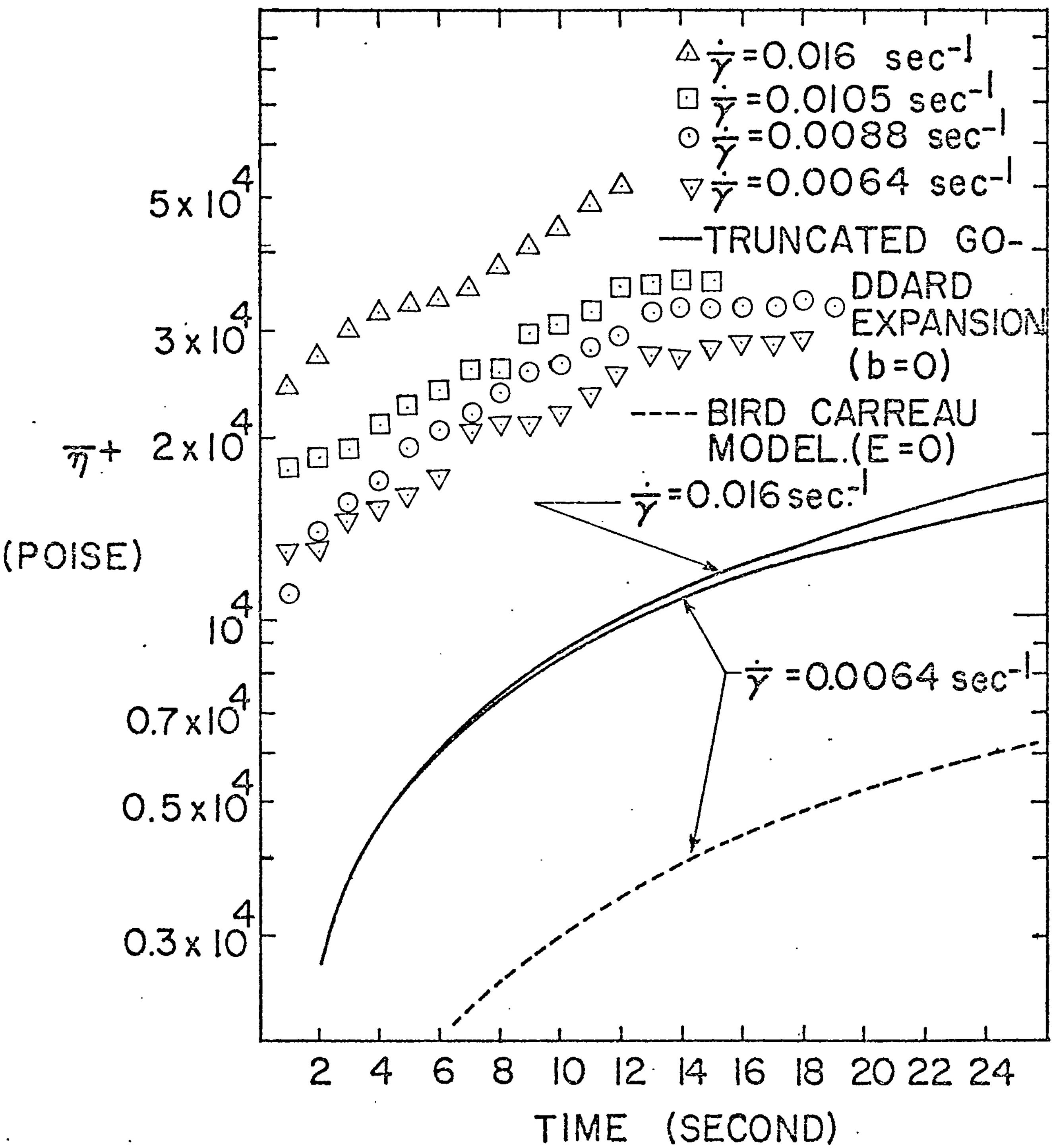

Figure 6-9 Comparison of the Instantaneous Extensional Viscosity Data of PAA with the Model Predictions; Model Parameters Determined from Viscometric Flow Data

Figure 6-10 Comparison of the Instantaneous Extensional Viscosity Data of PIB with the Model Predictions; Model Parameters Determined from Viscometric Flow Data

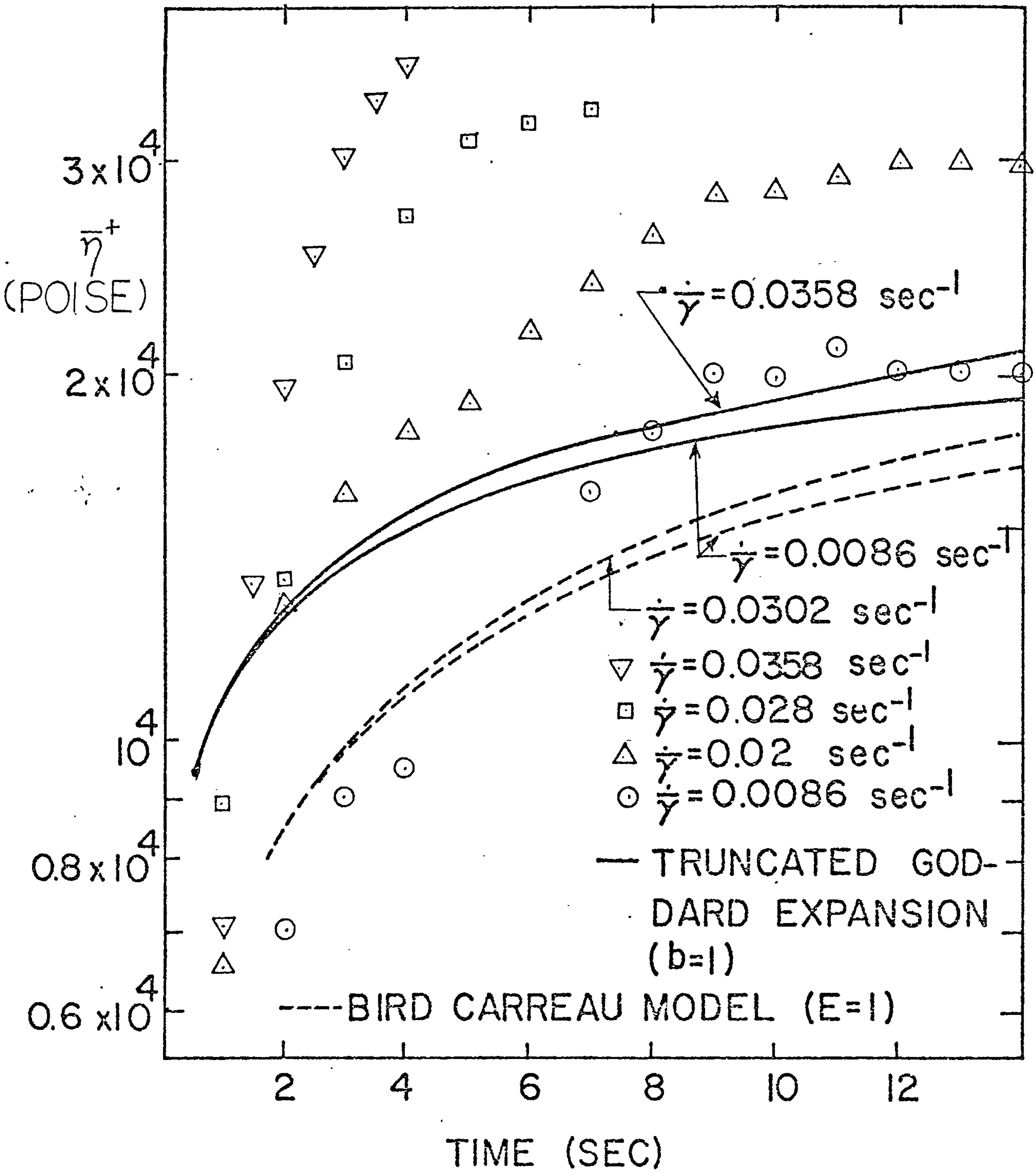

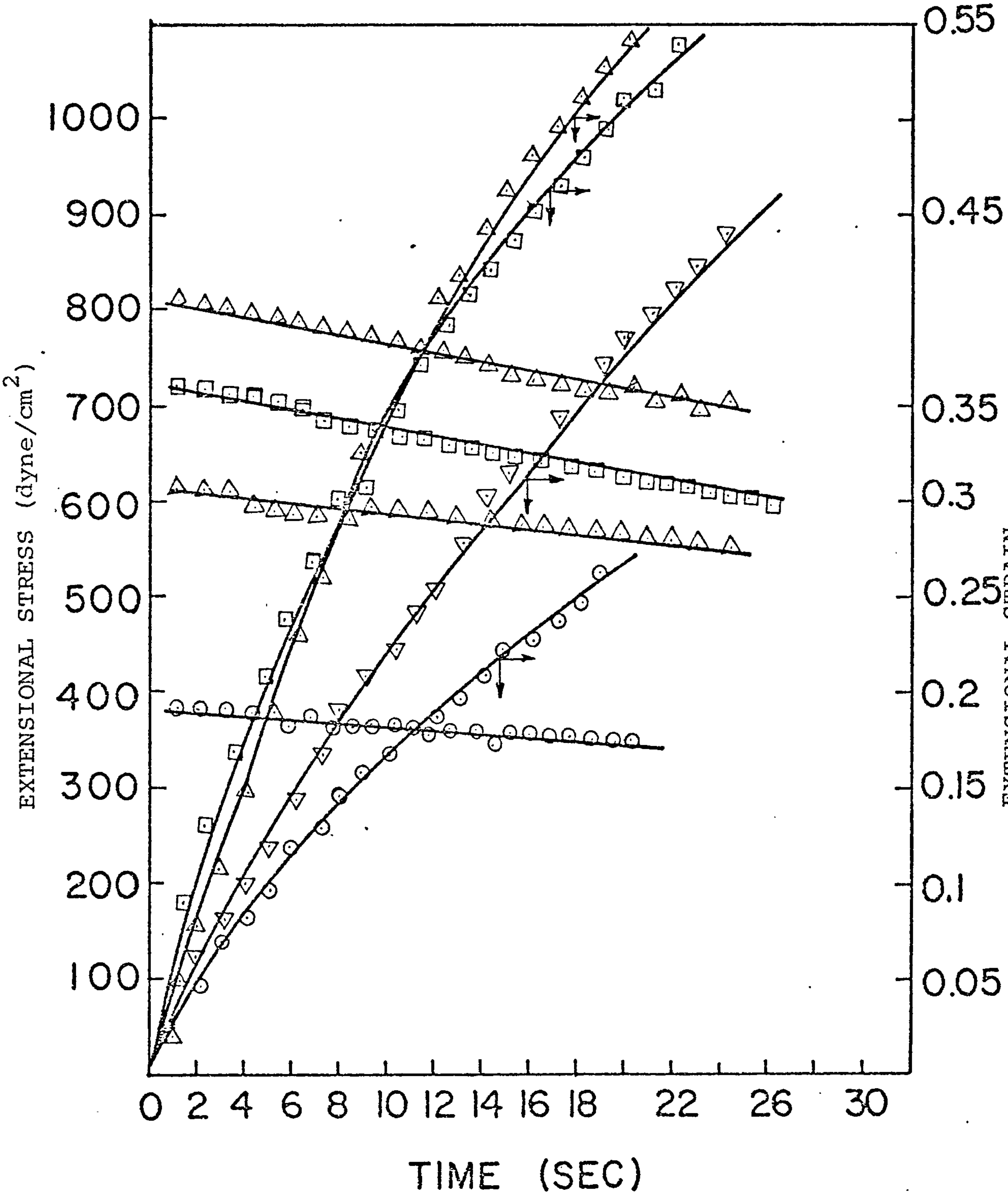

Figure 6-11 Strain and Corresponding Stress vs. Time for Approximate Creep Experiments with PAA

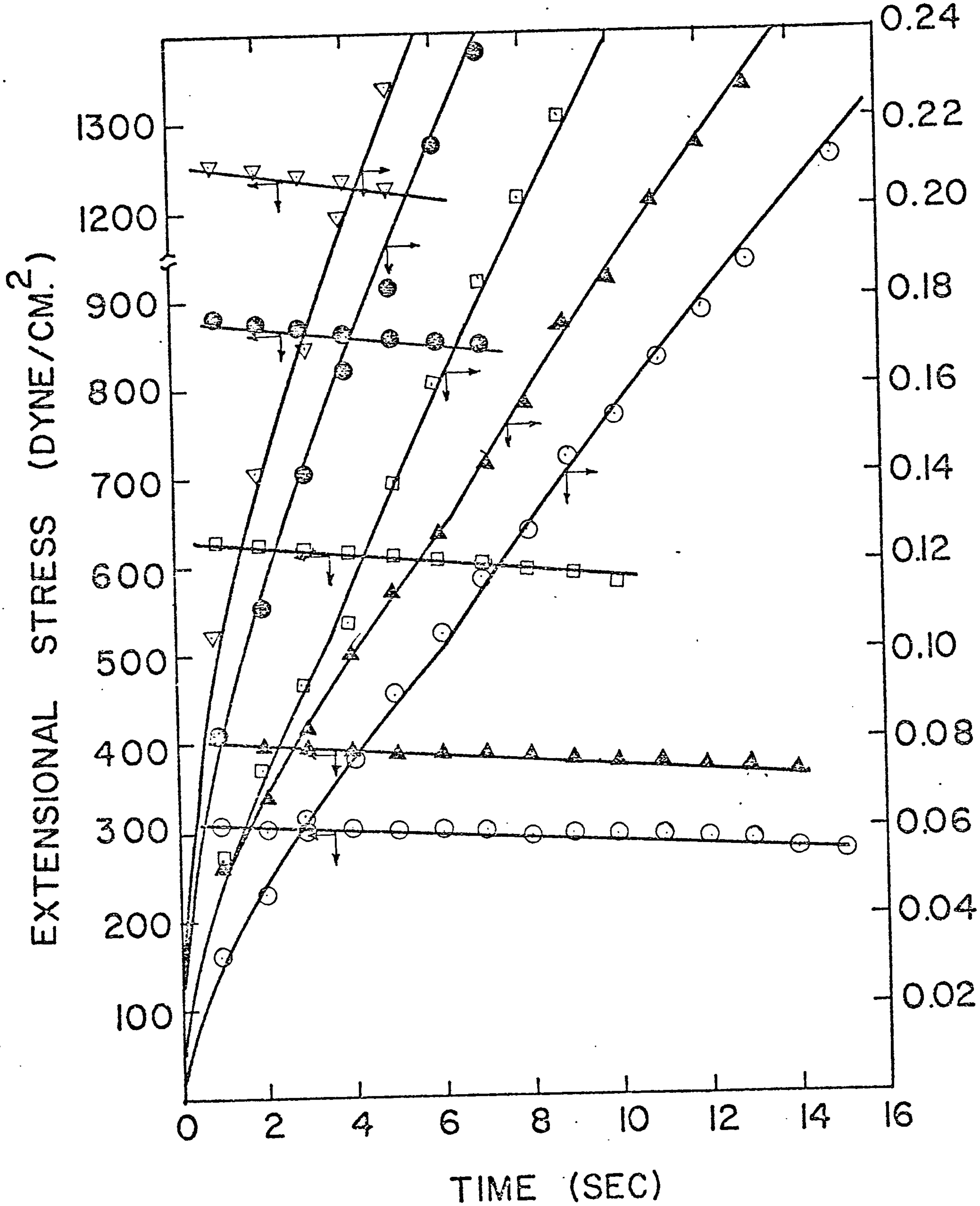

Figure 6-12 Strain and Corresponding Stress vs. Time for Approximate Creep Experiments with PIB

The experimental range of extension rate covered in the stress growth experiment were from 0.008 sec^{-1} to 0.035 sec^{-1} for PIB and from 0.006 sec^{-1} to o.o16 sec^{-1} for PAA. At extension rates smaller than 0.035 sec^{-1} for PIB and 0.016 sec^{-1} for PAA, the steady extensional viscosities were reached within the course of the experiments (about 15 seconds). However, due to the limitation imposed on maximum speed of the drive motor, the steady extensional viscosities were not reached for extension rates $\geq$ 0.035 sec^{-1} for PIB and $\geq$ 0.016 sec^{-1} for PAA. In the case of approximate creep experiment, the maximum possible extensional stress employed were 800 $dyne/cm^2$ and 1200 $dyne/cm^2$ for PIB and PAA respectively. Again, the values of this maximum possible extensional stress were limited by the operating constraints discussed in Section 4-3. Since the creep experiment conducted was approximate in nature, as shown in Figs. 6-11 and 6-12 the extensional stress was approximately constant and the percentage of maximum variation in stress is 10% for PIB and 12.5% for PAA.

Steady extensional viscosities obtained from both stress growth and approximate creep experiments are plotted versus the extension rates in Fig. 6-13 and 6-14. In the latter regard, an extensional stress, which is defined as the average between the stress at t=0 and the stress at the end of the experiment was used. As shown in Figs. 6-13 and 6-14, the steady extensional viscosity for bothPIB and PAA increase with increasing extension rate. In addition, at low extension rates ($\dot{\bar{\gamma}} <$ 0.001 sec^{-1} for PIB, $\dot{\bar{\gamma}} <$ 0.006 sec^{-1} for PAA) the steady extensional viscosity obtained is in

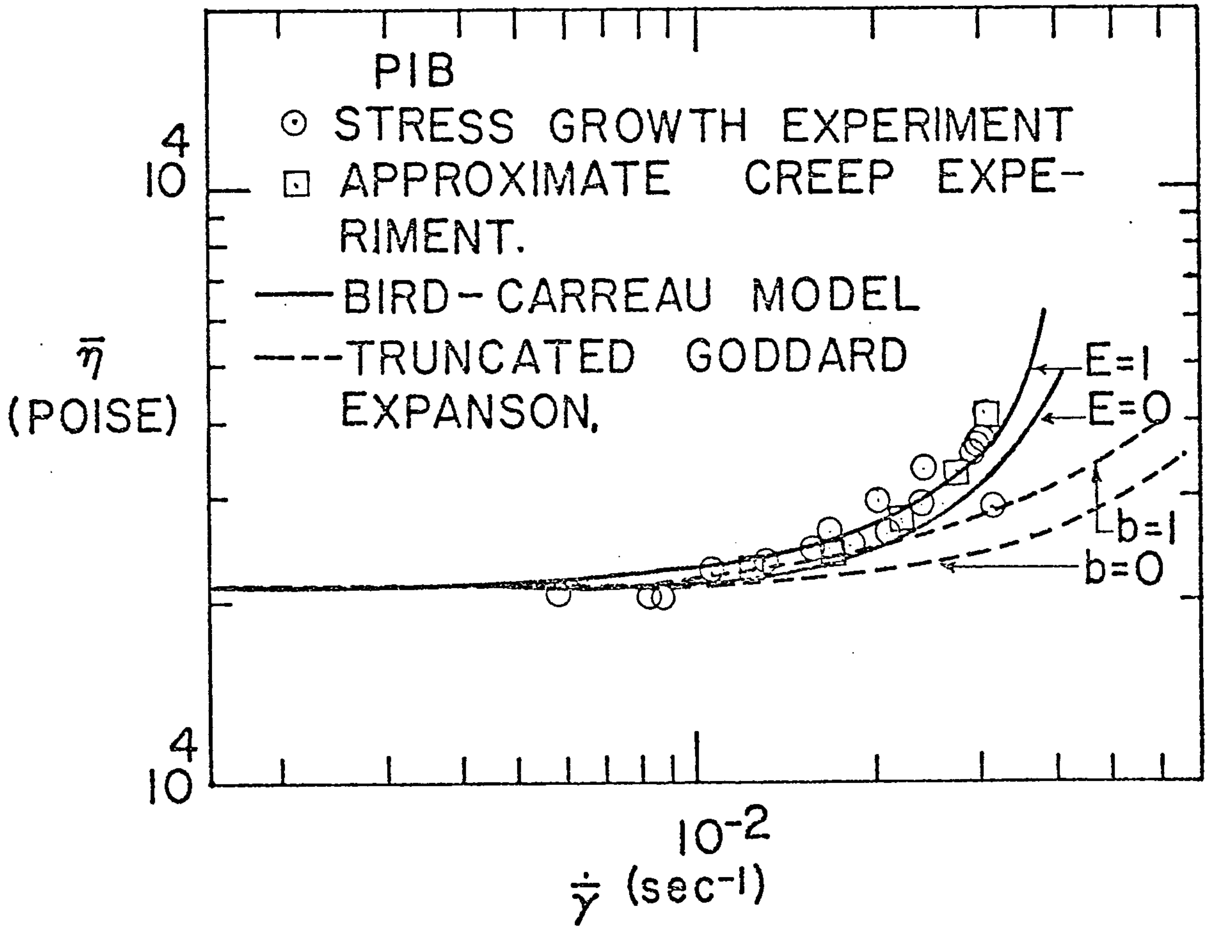

Figure 6-13 Comparison of the Steady Extensional Viscosity Data of PIB with the Model Predictions; Model Parameters Determined from Viscometric Flow Data

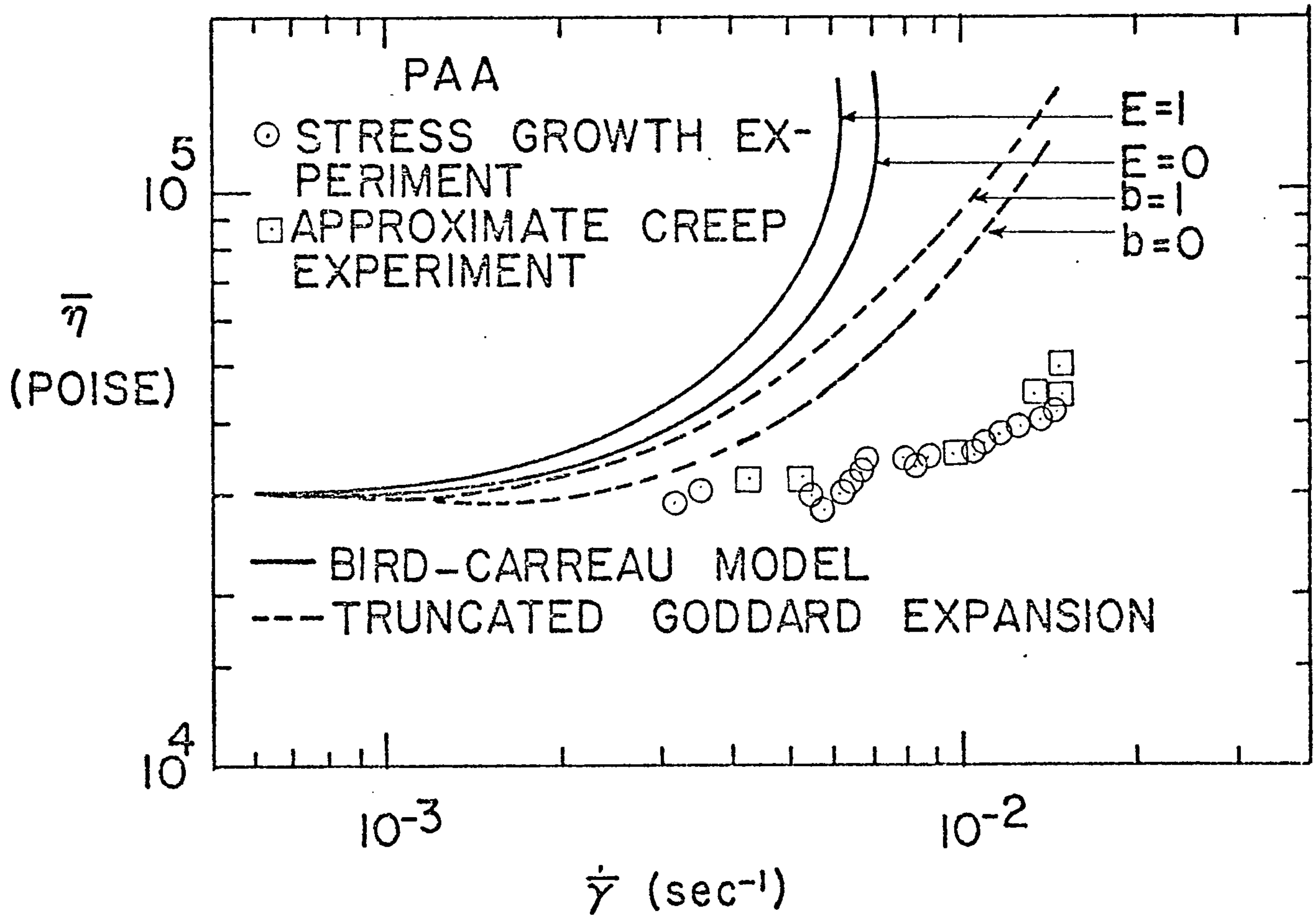

Figure 6-14 Comparison of the Steady Extensional Viscosity Data of PAA with the Model Predictions; Model Parameters Determined from Viscometric Flow Data

good agreement with Trouton's Law. It is important to note that the steady extensional viscosity obtained from two different experiments: stress growth and approximate creep fall on the same line (see Fig. 6-13 and 6-14). This provides a good check on the consistency of the experiments performed in the present drop elongation apparatus.

6-4-2. Comparison With Theories

The extensional viscosity data shown in Fig. 6-13 and 6-14 indicate that the extensional viscosities for two visco-elastic fluids PIB and PAA increase with increasing extension rate. Thus models which predict that the extensional viscosity decrease with increasing extension rate were discriminated. In the present work, the extensional flow data obtained were used to evaluate two viscoelastic models which have the capabilities of predicting the extensional viscosity increasing with increasing extension rate. These are the truncated Goddard expansion and Bird-Carreau model.

According to the previously described truncated Goddard expansion, the corotating rate of deformation tensors $\dot{\underset{\sim}{\Gamma}}(t, t')$, $\dot{\Gamma}''$, and $\dot{\Gamma}'''$ for uniaxial extensional flow, i.e.,

$$V_z = z\dot{\gamma} \quad , V_r = -\frac{\dot{\gamma}}{2} r , \tag{6-4-1}$$

take the forms:

$$\dot{\underset{\sim}{\Gamma}}(t,t') = \begin{pmatrix} \dot{\Gamma}_{zz} & \dot{\Gamma}_{zr} & \dot{\Gamma}_{z\theta} \\ \dot{\Gamma}_{rz} & \dot{\Gamma}_{rr} & \dot{\Gamma}_{r\theta} \\ \dot{\Gamma}_{\theta z} & \dot{\Gamma}_{\theta r} & \dot{\Gamma}_{\theta\theta} \end{pmatrix} = \begin{pmatrix} 2\dot{\gamma} & 0 & 0 \\ 0 & -\dot{\gamma} & 0 \\ 0 & 0 & -\dot{\gamma} \end{pmatrix} \tag{6-4-2}$$

$$\equiv \dot{\underset{\sim}{\Gamma}}' = \dot{\underset{\sim}{\Gamma}}'' = \dot{\underset{\sim}{\Gamma}}'''$$

where $\dot{\gamma}$ is a constant extension rate defined by $\dot{\gamma}=-\frac{2}{D}\frac{dD}{dt}$, and D is the drop diameter. The imposed past history of extension rate $\dot{\gamma}$ in the stress growth experiment is

$$\begin{aligned} \text{at} \quad t \le 0 \quad & \dot{\gamma} = 0 \\ t > 0 \quad & \dot{\gamma} = \text{constant} \end{aligned} \tag{6-4-3}$$

Combination of Equation (6-2-6), (6-4-2) and (6-4-3) yields

$$\Pi_{zz}-\Pi_{rr} = 3\int_0^t G_I(s)\dot{\gamma}s\,ds + 3b\dot{\gamma}^2\int_0^t sG_I(s)ds + \frac{9}{2}c\dot{\gamma}^3\int_0^t s^2G_I(s)ds \tag{6-4-4}$$

or

$$\bar{\eta}^+(t,\dot{\gamma}) = 3\int_0^t G_I(s)ds + 3b\dot{\gamma}\int_0^t sG_I(s) + \frac{9}{2}c\dot{\gamma}^2\int_0^t s^2G_I(s)ds \tag{6-4-5}$$

If $G_I(s)$ is selected as

$$G_I(s) = \sum_{i=1}^{5} a_i\lambda_i e^{-s/\lambda_i} \tag{6-2-12}$$

Equation (6-4-5) becomes

$$\begin{aligned} \bar{\eta}^+(t,\dot{\gamma}) = {} & 3\sum_{i=1}^{5} a_i\lambda_i^2(1-e^{-t/\lambda_i}) + 3b\dot{\gamma}\sum_{i=1}^{5} a_i\lambda_i\left[\lambda_i^2(1-e^{-t/\lambda_i})\right. \\ & \left.-\lambda_i t e^{-t/\lambda_i}\right] + \frac{9}{2}c\dot{\gamma}^2\sum_{i=1}^{5} a_i\lambda_i\left[2\lambda_i^3(1-e^{-t/\lambda_i}) - 2\lambda_i t e^{-t/\lambda_i}\right. \\ & \left.-\lambda_i t^2 e^{-t/\lambda_i}\right] \end{aligned} \tag{6-4-6}$$

when $t \to \infty$, the steady extensional viscosity is obtained

$$\bar{\eta}(\dot{\gamma}) = 3\sum_{i=1}^{5} a_i\lambda_i^2 + 3b\dot{\gamma}\sum_{i=1}^{5} a_i\lambda_i^3 + 9\dot{\gamma}^2c\sum_{i=1}^{5} a_i\lambda_i^4 \tag{6-4-7}$$

Equations (6-4-6) and (6-4-7) are the key equations in the truncated Goddard model to describe the extensional flow behavior of polymer solutions.

For the Bird-Carreau model, the strain tensor $\bar{\Gamma}^{ij}$ (defined in Equation (6-2-18)), Γ_{ij} (defined in Equation (6-2-19)), and the memory function m (defined in Equation (6-2-21)) for extensional flow with the viscosity flow field given in Equation (6-4-1) take the forms

$$\bar{\Gamma}^{ij}(t') = \begin{pmatrix} \bar{\Gamma}^{zz}(t') & \bar{\Gamma}^{zr} & \bar{\Gamma}^{z\theta} \\ \bar{\Gamma}^{rz}(t') & \bar{\Gamma}^{rr} & \bar{\Gamma}^{r\theta} \\ \bar{\Gamma}^{\theta z}(t') & \bar{\Gamma}^{\theta r} & \bar{\Gamma}^{\theta\theta} \end{pmatrix} = \begin{pmatrix} e^{2\dot{\gamma}(t-t')}-1 & 0 & 0 \\ 0 & e^{-\dot{\gamma}(t-t')}-1 & 0 \\ 0 & 0 & e^{-\dot{\gamma}(t-t')}-1 \end{pmatrix} \tag{6-4-8}$$

$$T_{ij}(t') = \begin{pmatrix} T_{zz}(t') & T_{zr}(t') & T_{z\theta}(t') \\ T_{rz}(t') & T_{rr}(t') & T_{r\theta}(t') \\ T_{\theta z}(t') & T_{\theta r}(t') & T_{\theta\theta}(t') \end{pmatrix} = \begin{pmatrix} 1-e^{-2\dot{\gamma}(t-t')} & 0 & 0 \\ 0 & 1-e^{\dot{\gamma}(t-t')} & 0 \\ 0 & 0 & 1-e^{\dot{\gamma}(t-t')} \end{pmatrix} \quad (6\text{-}4\text{-}9)$$

and

$$m(t-t', \dot{\gamma}) = \sum_{p=1}^{\infty} \frac{\eta_p}{\lambda_{2p}^2} \frac{e^{-(t-t')/\lambda_{2p}}}{1+3\lambda_{1p}^2\dot{\gamma}^2} \quad (6\text{-}4\text{-}10)$$

By combining Equations (6-2-17), (6-4-8), (6-4-9) and (6-4-10), the apparent extensional viscosity $\bar{\eta}^+(t,\dot{\gamma})$ is obtained as

$$\bar{\eta}^+(t,\dot{\gamma}) = -\sum_{p=1}^{\infty} \frac{\eta_p}{\lambda_{2p}\dot{\gamma}(1+3\dot{\gamma}^2\lambda_{1p}^2)} \left\{ \left(1+\frac{E}{2}\right)\left[\frac{1-e^{-t(\frac{1}{\lambda_{2p}}+\dot{\gamma})}}{1+\lambda_{2p}\dot{\gamma}} - \frac{1-e^{-t(\frac{1}{\lambda_{2p}}-2\dot{\gamma})}}{1-2\dot{\gamma}\lambda_{2p}}\right] - \frac{E}{2}\left[\frac{1-e^{-t(\frac{1}{\lambda_{2p}}+2\dot{\gamma})}}{1+2\dot{\gamma}\lambda_{2p}} - \frac{1-e^{-t(\frac{1}{\lambda_{2p}}-\dot{\gamma})}}{1-\lambda_{2p}\dot{\gamma}}\right]\right\} \quad (6\text{-}4\text{-}11)$$

Again, as $t \to \infty$, the steady extensional viscosity is obtained

$$\bar{\eta}(\dot{\gamma}) = \sum_{p=1}^{\infty} \frac{3\eta_p}{1+3\dot{\gamma}^2\lambda_{1p}^2}\left[\frac{1+\frac{E}{2}}{(1+\lambda_{2p}\dot{\gamma})(1-2\dot{\gamma}\lambda_{2p})} - \frac{\frac{E}{2}}{(1+2\dot{\gamma}\lambda_{2p})(1-\lambda_{2p}\dot{\gamma})}\right] \quad (6\text{-}4\text{-}12)$$

where η_p , λ_{1p} , and λ_{2p} are defined by Equation (6-2-22).

Since both viscometric and extensional flow data of PIB and PAA were available in the present work, the model parameters in both Bird-Carreau model and truncated Goddard expansion were determined in two different ways: by using the viscometric data only and by using both viscometric and extensional flow data. The procedures of determining the model parameters using the viscometric data were described in Section 6-2. The model parameters obtained from a computer fitting of the η ,$-(\tau_{xx}-\tau_{yy})$, η', and G' data are listed in Table 6-2. With these parameters, Equations (6-4-6) to (6-4-7) and Equations (6-4-11) to (6-4-12) give the predictions of $\bar{\eta}^+$ and $\bar{\eta}$ for the truncated Goddard expansion and Bird-Carreau model respectively.

Both E (in Equations(6-4-11) and (6-4-12)) and b (in Equations 6-4-6) and (6-4-7)) are arbitrarily given values between 0 and 1. Fig. 6-9 and Fig. 6-10 give the comparison of the $\bar{\eta}^{+}$ data and the model predictions while the $\bar{\eta}$ data and the corresponding predictions from both models are plotted in Figs. 6-13 and 6-14. For the case of determining the model parameters by using both viscometric and extensional flow data, the data of η , η' , and $\bar{\eta}$ were used. The data of $\bar{\eta}$ were given the same weight as the combination of the η and η' data. Then, the η, η' , and $\bar{\eta}$ data were fitted simultaneously using BSOLVE computer program. The parameters E in Equation (6-4-12) and b in Equation (6-4-7) were arbitrarily given a value between 0 and 1 in the computer fitting. The fitted model parameters in both truncated Goddard expansion and Bird-Carreau model are listed in Table 6-3. With the parameters in Table 6-3, the predictions of $\bar{\eta}^{+}$ from the truncated Goddard expansion and Bird-Carreau model were obtained from Equations (6-4-6) and (6-4-11) respectively. Figs. (6-15) to (6-20) give the comparison of the experimental data: η, η', and $\bar{\eta}$ and the corresponding model predictions, while the $\bar{\eta}^{+}$ data along with the predictions from both truncated Goddard expansion and Bird-Carreau model are shown in Figs. 6-21 and 6-22.

Several observations can be made about the results in Figs. 6-9 to 6-22.

(1) With the model parameters determined from the viscometric flow data, the Bird-Carreau model describes the $\bar{\eta}$ data

Table 6-3 Model Parameters Determined with Both Viscometric and Extensional Flow Data.

Solutions	Bird-Carreau Model							
	E	η_0	λ_1	λ_2	α_1	α_2	λ_1/λ_2	α_2/α_1
PIB*	1	7000	14.	14.6	1.24	0.83	0.96	0.67
	0	7000	10.	13.7	1.28	1.04	o.78	0.81
PAA**	1	9700	39.	24.6	3.68	2.67	1.6	0.73
	0	9700	40.	20.4	3.62	2.47	1.96	0.68

Solutions	Truncated Goodard Expansion											
	b	λ_1	λ_2	λ_3	λ_4	λ_5	a_1	a_2	a_3	a_4	a_5	c
PIB*	1	10	1	0.1	0.01	0.001	30	2500	67000	7.2×10^6	1.0×10^8	3.2
	0	10	1	0.1	0.01	0.001	32	2400	39000	9.1×10^6	1.0×10^8	4.4
PAA**	1	50	5	0.5	0.05	0.005	3	73	1080	16000	9.3×10^5	0.
	0	50	5	0.5	0.05	0.005	3.2	61	932	14000	8.1×10^5	0.5

PIB* - 10% polyisobutylene in Decalin

PAA** - 2.8% polyacrylamide in 1:1 mixture by weight of glycerol-water solutions

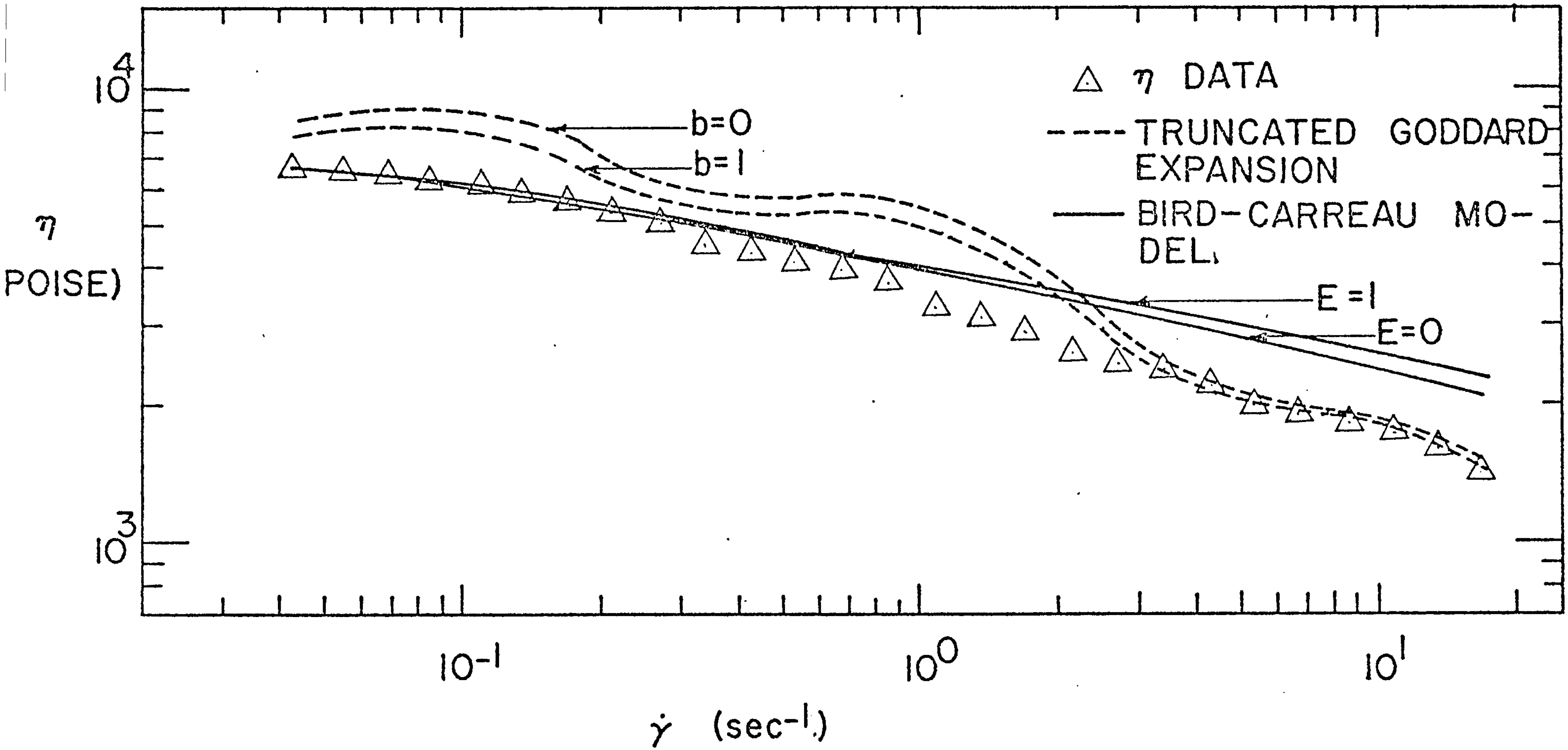

Figure 6-15 Comparison of the Shear Viscosity Data of PIB with the Model Predictions; Model Parameters Determined from Both Viscometric and Extensional Flow Data

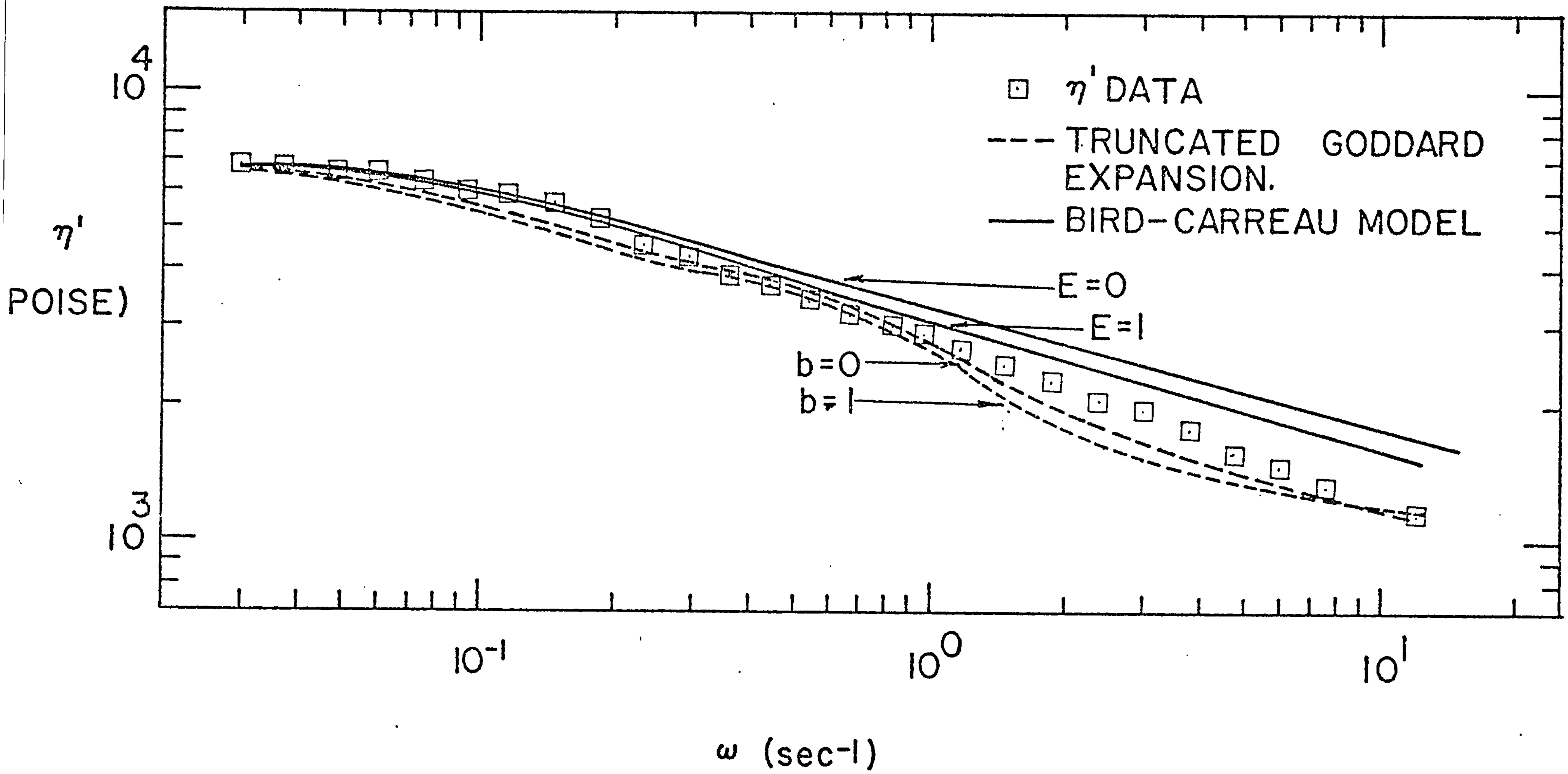

Figure 6-16 Comparison of the Dynamic Viscosity Data of PIB with the Model Predictions; Model Parameters Determined from Both Viscometric and Extensional Flow Data

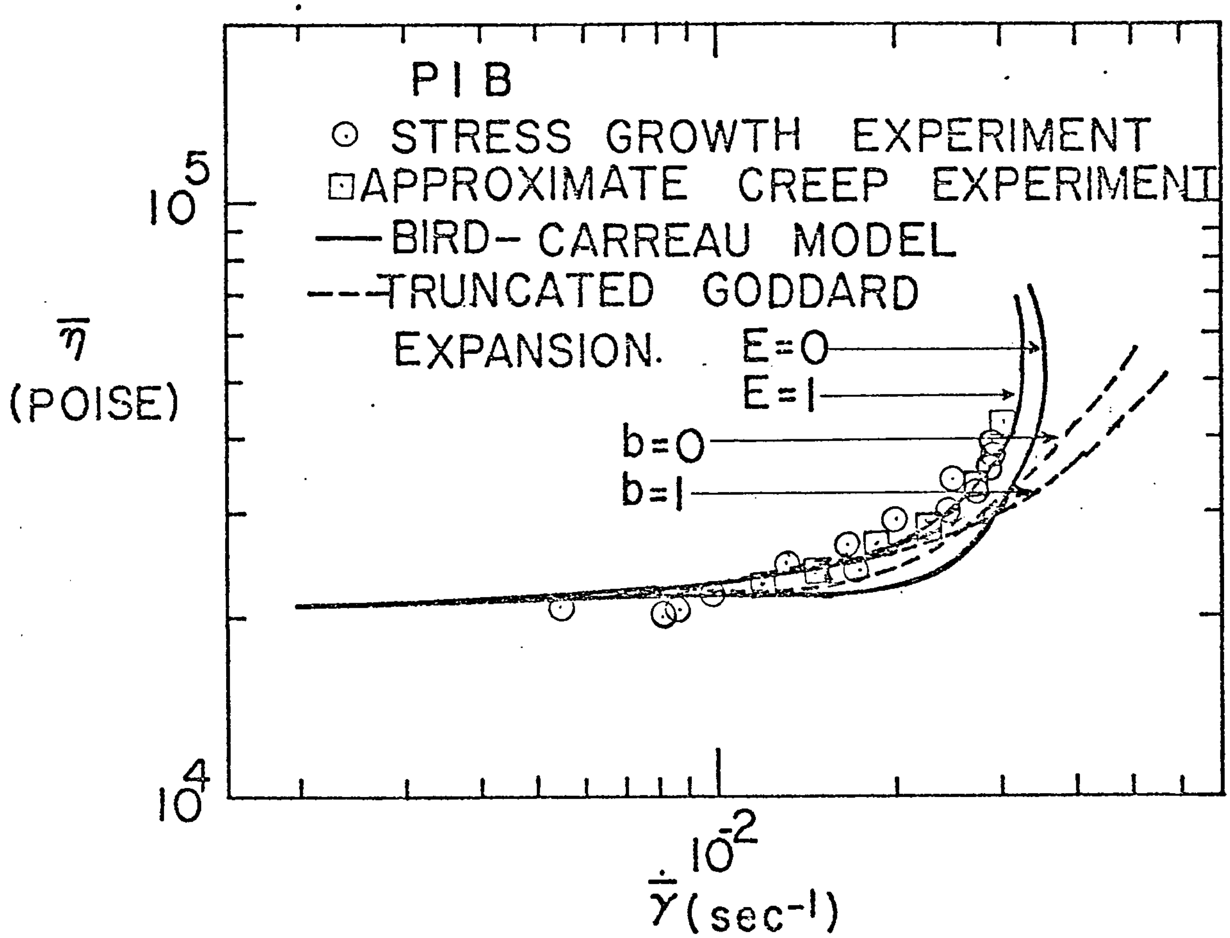

Figure 6-17 Comparison of the Steady Extensional Viscosity Data of PIB with the Model Predictions; Model Parameters Determined from Both Viscometric and Extensional Flow Data

Figure 6-18 Comparison of the Shear Viscosity Data of PAA with the Model Predictions; Model Parameters Determined from Both Viscometric and Extensional Flow Data

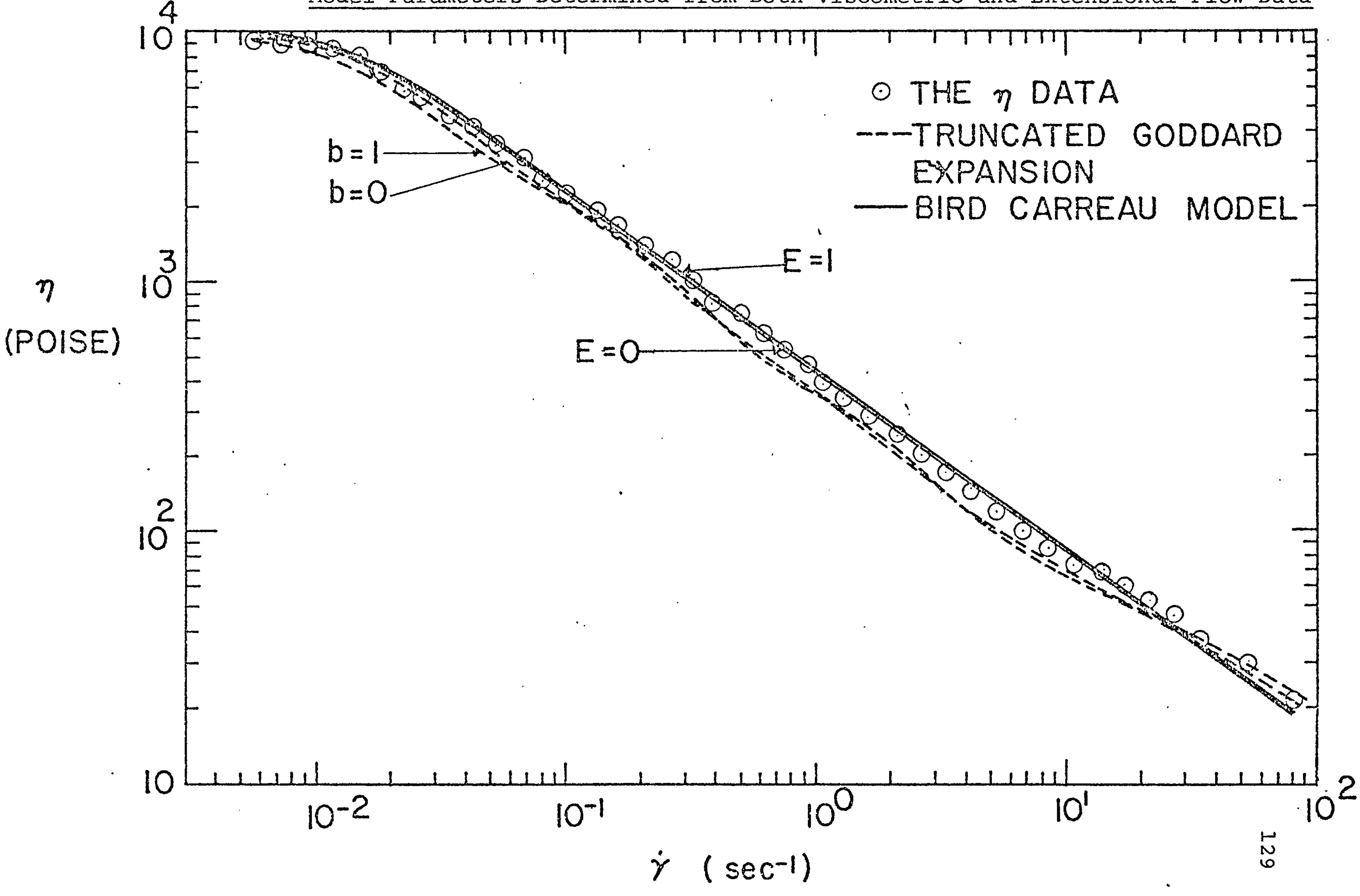

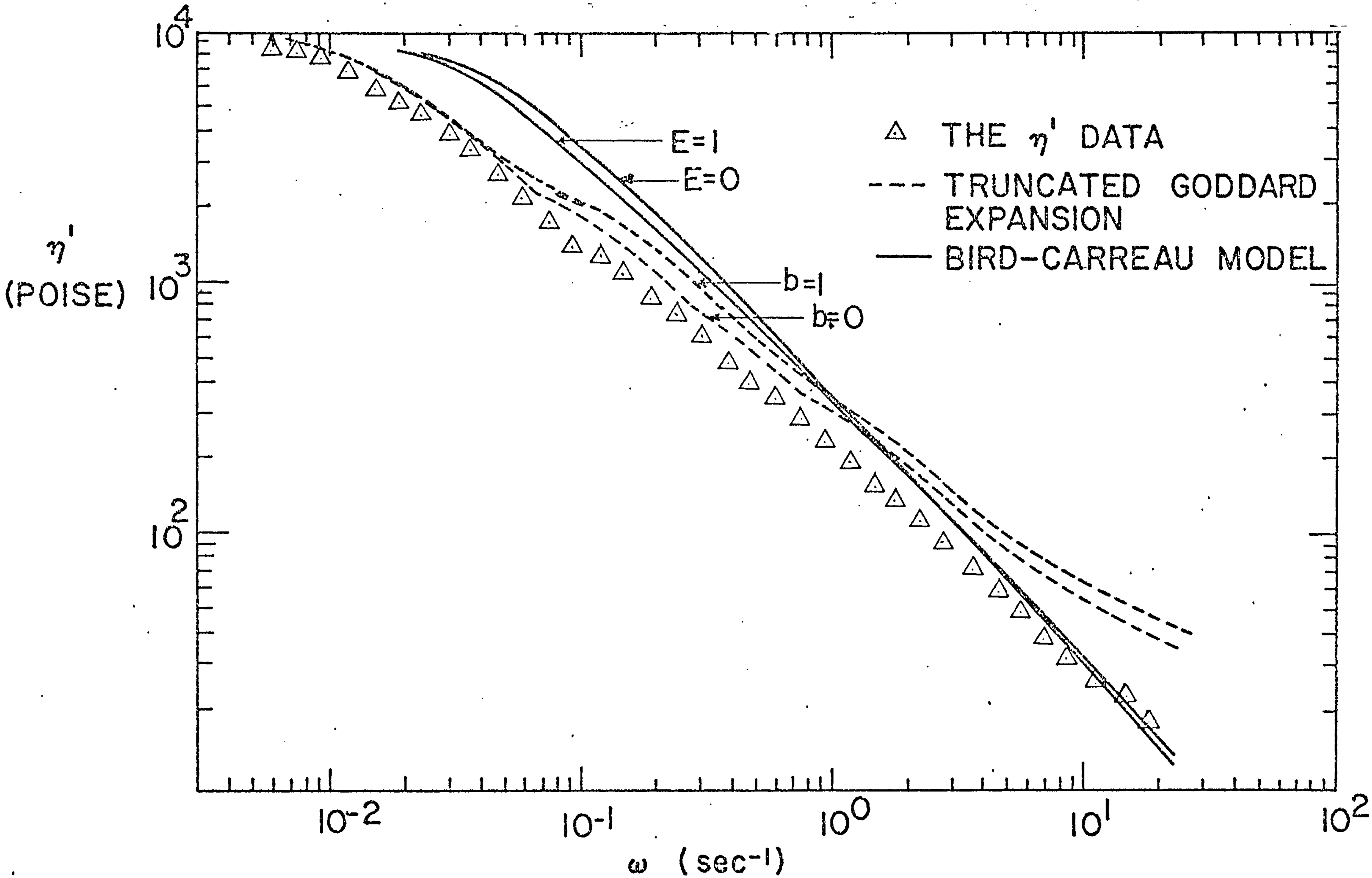

Figure 6-19 Comparison of the Dynamic Viscosity Data of PAA with the Model Predictions; Model Parameters Determined from Both Viscometric and Extensional Flow Data

Figure 6-20 Comparison of the Steady Extensional Viscosity Data of PAA with the Model Predictions; Model Parameters Determined from Both Viscometric and Extensional Flow Data

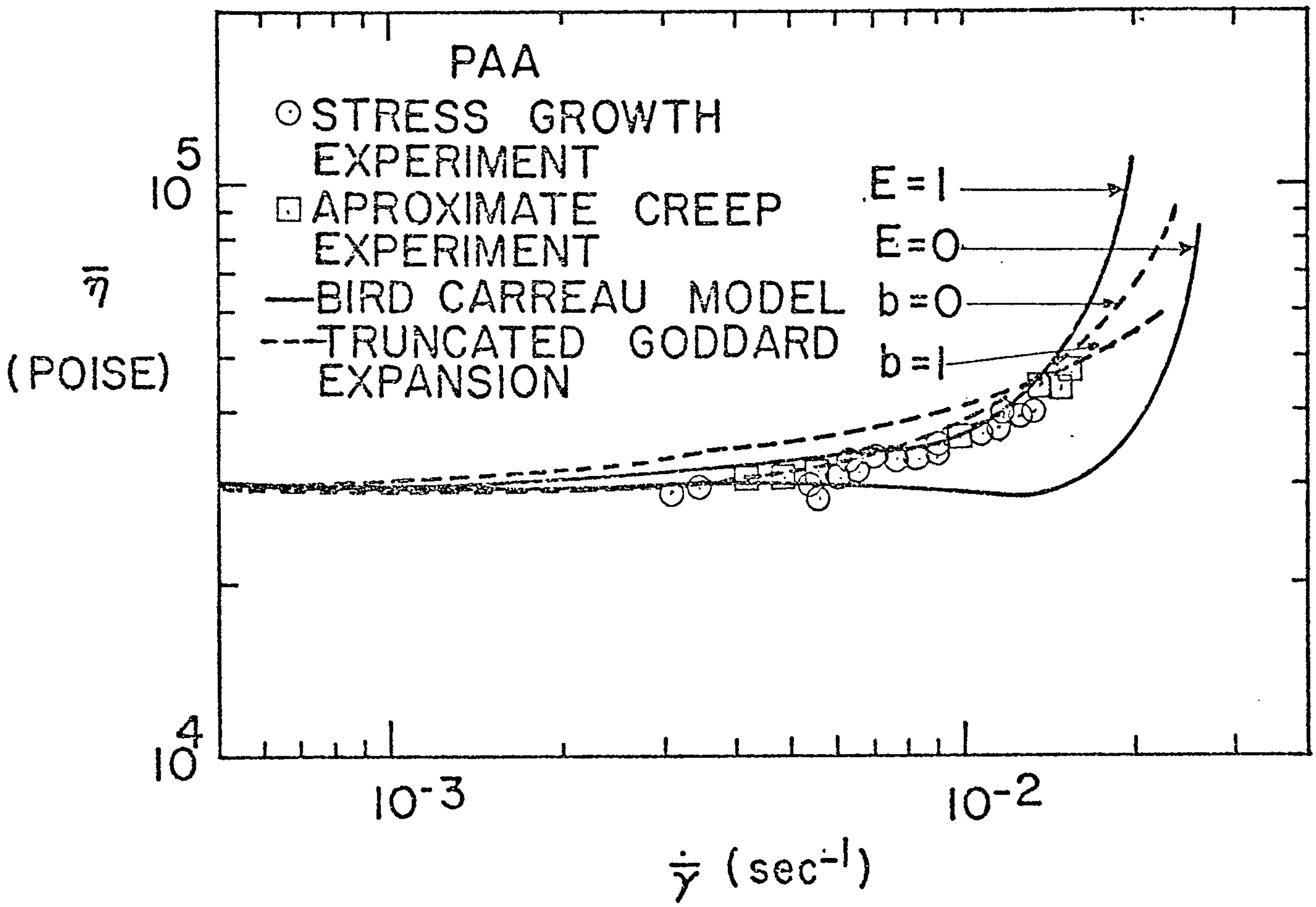

Figure 6-21 Comparison of the Instantaneous Extensional Viscosity Data of PAA with the Model Predictions; Model Parameters Determined from Both Viscometric and Extensional Flow Data

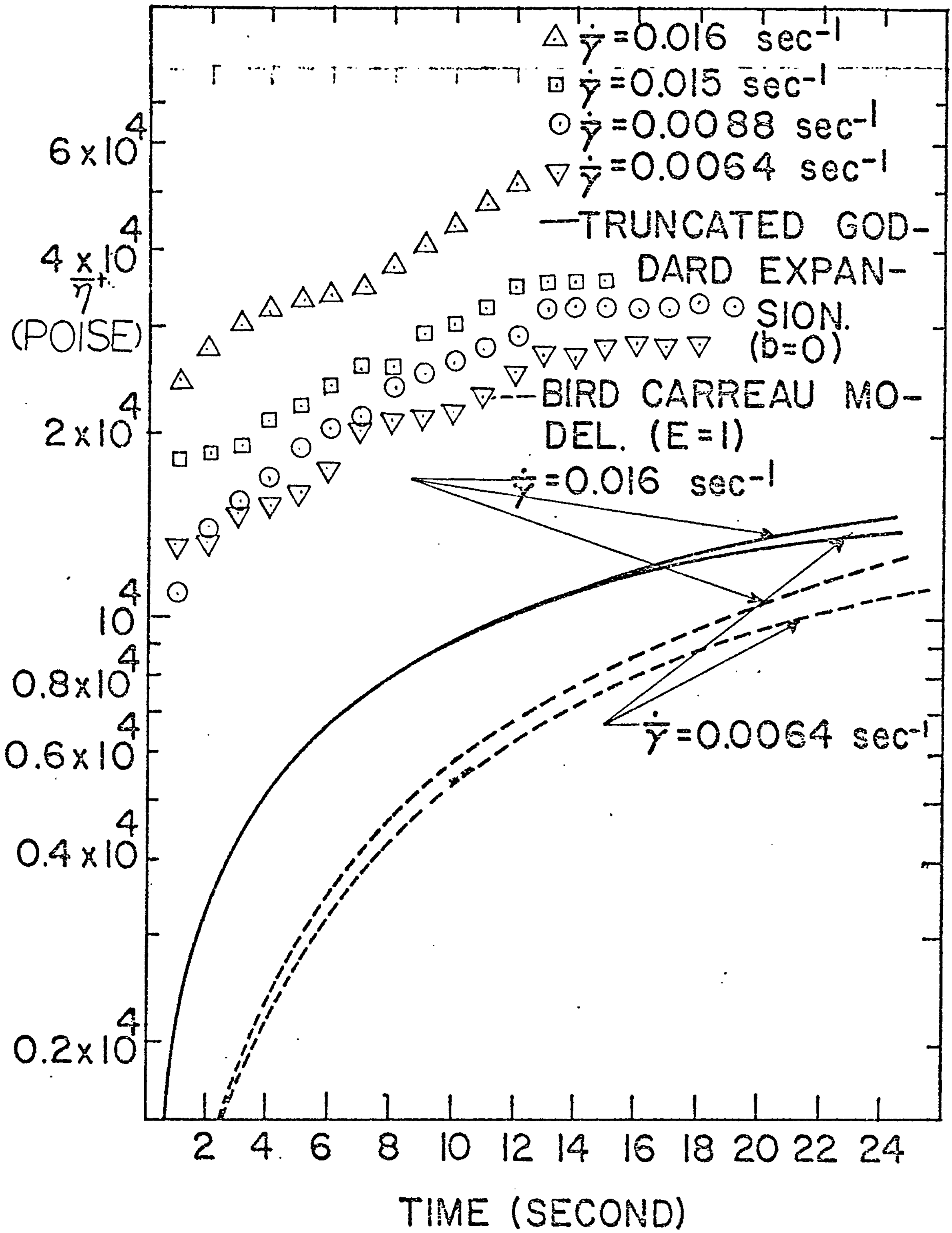

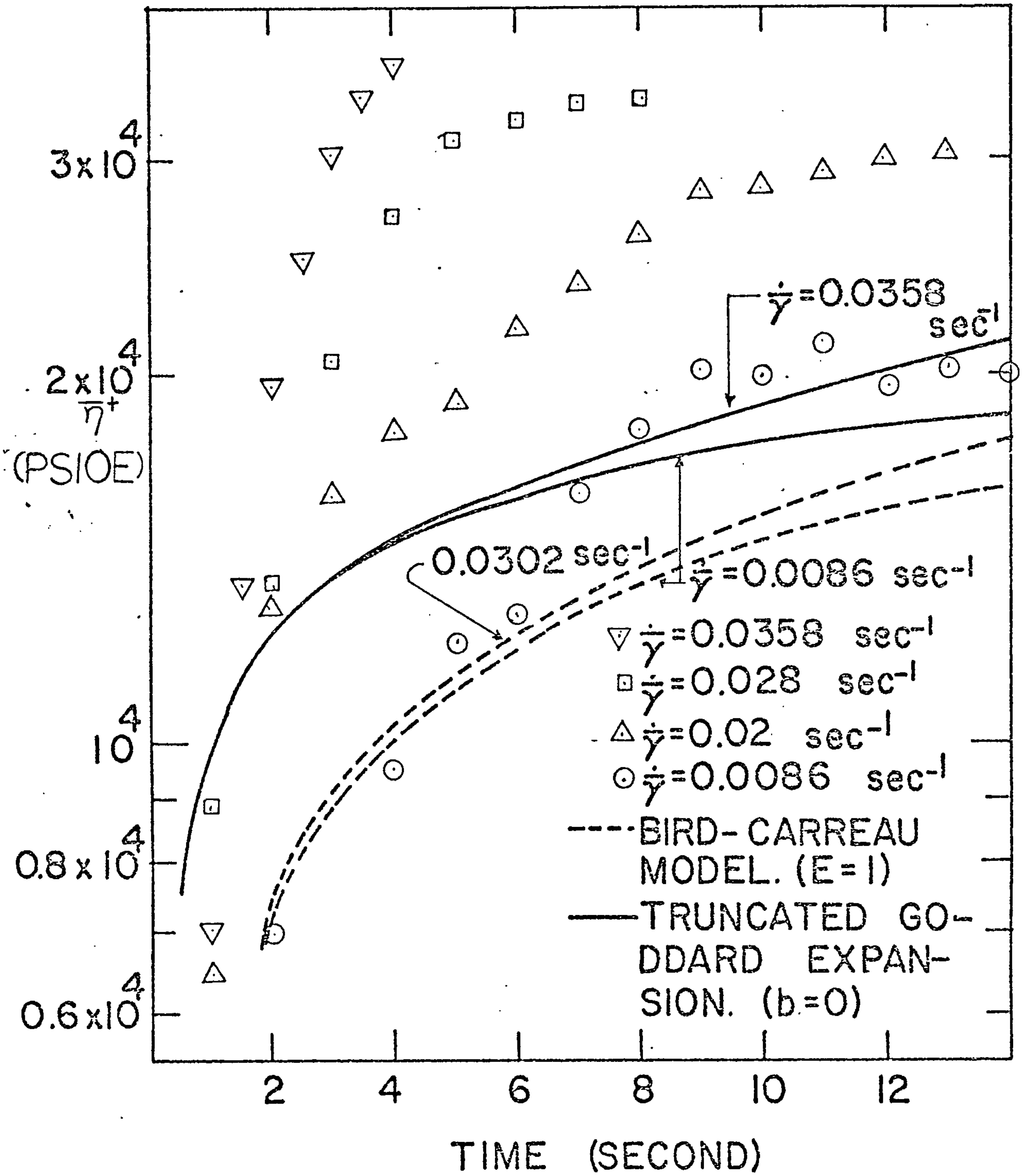

Figure 6-22 Comparison of the Instantaneous Extensional Viscosity Data of PIB with the Model Predictions; Model Parameters Determined from Both Viscometric and Extensional Flow Data

of PIB better than the truncated Goddard expansion as shown in Fig. 6-13. However, as it can be seen in Fig. 6-14, both models describe the $\bar{\eta}$ data of PAA only qualitatively and in fact, the truncated Goddard expansion predicts the $\bar{\eta}$ data quantitatively better than the Bird-Carreau model. It should be noted that according to the definitions of E (defined in Equation (6-2-20)) and b (defined in Equation (6-2-11)), both models predict qualitatively the same effect on the steady extensional viscosity due to the changes in the ratio of second to first normal stress difference in steady shearing flow. Also, from Fig. 6-13 and 6-14, we may conclude that b and E are not critical parameters in the respective truncated Goddard expansion and Bird-Carreau model.

(2) From Figs. 6-9, 6-10, 6-21, and 6-22, it appears that no matter how the model parameters were determined, the observed $\bar{\eta}^+$ immediately after the step change in extension rate was larger and more rapid than the predictions from both models. As a comparison, after a step change was made on the extension rate the predictions of $\bar{\eta}^+$ from the truncated Goddard expansion rose and approached the steady extensional viscosity much faster than the predictions from Bird-Carreau model. But, in general, both models describe the transient extensional flow $\bar{\eta}^+$ data poorly for both PIB and PAA.

(3) In the case of determining the model parameters with both viscometric and extensional flow data, the $\bar{\eta}$ data are

described pretty well by both models as shown in Fig. 6-17 and 6-20. This good agreement between the $\bar{\eta}$ data and model predictions shown in Fig. 6-17 and 6-20 is expected since the data is used in the process of determining the parameters in both Bird-Carreau model and truncated Goddard expansion. Similar to the predicted behavior of η and η' from the truncated Goddard expansion as shown in Fig.6-1 and Fig. 6-2, the predictions of η and η' from the truncated Goddard expansion in Figs. 6-15, 6-16, 6-18, and 6-19 show oscillatory behavior. As the reasons discussed in Section 6-2, the oscillation in the predictions of η and η' from the truncated Goddard expansion is due to the truncated characteristics of the form used for G_I. It should be noted that in order to obtain the model predictions of $\bar{\eta}$ vs $\dot{\bar{\gamma}}$, the values of E in the Bird-Carreau model and b in the truncated Goddard expansion are required in addition to the model parameters. Since b and E are not involved in the predicted equations of η, $-(\tau_{xx}-\tau_{yy})$, η', and G' in the respective truncated Goddard expansion and Bird-Carreau model, b and E thus were not obtainable in the case of fitting the model parameters with viscometric flow data. The model predictions of $\bar{\eta}$ shown in Figs. 6-13 and 6-14 were obtained from Equation (6-4-7) (or (6-4-12)) by arbitrarily assigning b (or E) a value between 0 and 1. However, in the case of fitting the model parameters with the η, η', and $\bar{\eta}$ data, the values of b and E were prescribed and the model parameters were then determined by using BSOLVE. Because of different fitting prcedures in the two cases discussed above, the effect of b on the resulting predictions of $\overline{\eta}$ from the truncated Goddard expansion in Figs. 6-13 and 6-14 is different from that in Figs. 6-17 and 6-20. However, the effect of E on $\overline{\eta}$ predicted by the Bird-Carreau model is the same for the two cases as it can be seen in Figs. 6-13, 6-14, 6-17, and 6-20. It should be noted that to date, few experimental data of second normal stress difference are available. Based on the existing second normal stress difference data (24,81), the values for b and E are ranging from 0 to 2 and -1 to 1 respectively. As it can be seen in Figs. 6-13 to 6-20, b (or E) is not a critical parameter in the truncated Goddard expansion (or Bird-Carreau model). Hence, assigning a value between 0 and 1 for b (or E) in the computer fitting does not seem to be a serious limitation.

In summarizing the above discussions, it appears that for the two polymer solutions tested in the present work, the Bird-Carreau model described both the viscometric and the steady extensional flow data quantitatively better than did the truncated Goddard expansion. It has been indicated(78) that the Bird-Carreau model can not describe the transient behavior in steady shearing flow. The present work shows that the Bird-Carreau model also describe transient extensional flow data poorly.

CHAPTER VII

CONCLUSIONS AND RECOMMENDATIONS

In the present work, an experimental apparatus employing a drop elongation motion to achieve extensional flow has been designed, constructed, and tested. With this instrument, the extensional flow behavior of one Newtonian fluid and two viscoelastic polymer solutions were studied. The extensional flow data obtained with the viscoelastic polymer solutions were compared with the predictions of two viscoelastic constitutive equations— the Bird-Carreau model and the truncated Goddard expansion. The major results are summarized as follows:

(1) For incorporating the interfacial effect into the analysis of the drop elongation technique, the knowledge of the drop shape, particularly the curvature at the end of the drop surface is required. Two analyses were made to obtain these information: an analytic approximation and a numerical analysis. In the former, the drop shape during extension were obtained by making the assumption that the fluid experience uniaxial extension flow. In the numerical analysis, the drop elongation phenomena in the approximate creep experiment was simulated by employing the orthogonal collocation method,

and hence the instantaneous drop shape was obtained. After comparing the experimental data of the curvature at the end of the drop shape with the corresponding predictions from all these analyses, the analysis based on the assumption that the fluid experiences uniaxial extensional flow was found to estimate the curvature at the end of the drop surface reasonably well.

(2) Tests with the Newtonian fluid verify the capabilities of the drop elongation apparatus. Both stress growth and approximate creep experiments can be performed in the drop elongation apparatus. With the present control system in the apparatus, the prescribed responses in the stress growth experiments and the approximate creep experiments were achieved in a time period less than one second. In general, the controlled response in the approximate creep experiments was better than that in the stress growth experiments. The results for the extensional viscosity obtained both from the stress growth and the approximate creep experiments are in good agreement with Trouton's law.

(3) Two viscoelastic polymer solutions: a 10% polyisobutylene in Decalin (PIB) and a 2.8% polyacrylamide

in 50:50 glycerol-water solution (PAA) were tested in both the Weissenberg Rheogoniometer and the drop elongation apparatus. In shear flow, both PIB and PAA exhibit significant shear-thinning and elastic effects. The elastic effects are noted by performing oscillatory experiments on the Rheogoniometer. With the drop elongation apparatus, both stress growth and approximate creep experiments were carried out. The steady extensional viscosity of PIB in the stress growth experiment is reached within a shorter period of time than that of PAA for the same steady state extension rate. Also, for the approximate creep experiment, the extensional strain of PIB reaches steady state (extension rate is constant or strain increases linearly with time) earlier than does PAA at the same imposed steady state stress level. The steady extensional viscosity for both polymer solutions was found to increase with increasing extension rate over a range of extension rates from 0.003 sec^{-1} to 0.016 sec^{-1} for PAA and from 0.003 sec^{-1} to 0.035 sec^{-1} for PIB.

(4) Both the truncated Goddard expansion and the Bird-Carreau model were used to characterize PIB and PAA in two different ways. In the first case, the parameters in both models were determined by simultantaneously fitting the steady and transient shear

data. The extensional flow data were then compared with the corresponding model predictions. In the second case, the model parameters were obtained by fitting both the shear and the extensional flow data, with the extensional and shear being weighted equally. With the model parameters determined from the viscometric flow data, the Bird-Carreau model predicted the steady extensional viscosity data of PIB better than the truncated Goddard expansion; both models predicted the steady extensional viscosity data of PAA poorly. When the model parameters were determined from both viscometric and steady extensional flow data, the viscometric and steady extensional flow data for both PIB and PAA were in better agreement with the corresponding predictions from the Bird-Carreau model than with the predictions from the truncated Goddard expansion. However, in spite of how the model parameters were determined, both models were found to predict the transient extensional flow data poorly. It was also found that in both the Bird-Carreau model and the truncated Goddard expansion, the predictions of the steady extensional viscosity are insensitive to the value of the ratio of second normal stress coefficient to the first normal stress coefficient.

These studies suggest a number of extensions and recommendations for the future work:

(1) It is strongly suggested that the size of the glass cylinder be scaled down and that air bearings be used. With a smaller glass cylinder and with air bearings, the maximum rotational speed of the glass cylinder can be increased and consequently, the operating range of the extension rates can be enlarged.

(2) Another suggestion for future research is to employ a more uniform light source (say a laser). This would reduce the noise generated in the photomultiplier tube and hence, the response of the control system could be improved.

(3) There is a definite need for making a more complete appraisal of some representative rheological models by use of both shear and extensional flow data. Such work can evaluate the usefulness of these models in predicting the flow behavior of polymeric materials, and also can provide a direction for the future development of the viscoelastic theories.

BIBLIOGRAPHY

1. Ballman,R.L., Rheol. Acta, 4, 137 (1965).
2. Cogswell, F.N., Plast. Inst. Trans. J., 109, April (1968).
3. Vingradov, G.V., B.V. Radushkevich, and V.D. Fikhman, J. Polymer Sci., A-2, 8, 1 (1970).
4. Metzner, A.B., and A.P. Metzner, Rheol. Acta, 9, 174 (1970).
5. Astarita, G., and L. Nicodemo, Chem. Eng. J., 1, 57 (1970).
6. Meißner, J., Rheol. Acta, 10, 230 (1971).
7. Weinberger, C.B., Ph.D. Thesis, University of Michigan, Ann Arbor, Michigan (1970).
8. Hsu, J.C., and R.W. Flumerfelt, paper accepted for publication, Trans. Soc. Rheol., (1975).
9. Vonnegut, B., Rev. Sci. Instr., 13, 6 (1942).
10. Princen, H.M., in Surface and Colloid Science, edited by E. Matijevic Wiley-Interscience, New York, 2, 72 (1969).
11. Princen, H.M., I.Y.Z. Zia, and S.G. Mason, J. Coll. Sci., 23, 99 (1967).
12. Bird, R.B., and P.J. Carreau, Chem. Eng. Sci., 23, 427 (1968).
13. Bird, R.B., O. Hassager, and S.I. Abdel-Khalik, AIChE J., 20, 1041 (1974).
14. Coleman, B.D., Proc. Roy. Soc., A-306, 449 (1968).
15. Coleman, B.D., and W. Noll, Phys. of Fluids, 5, 840 (1962).
16. Kanel, F.A., Ph.D. Dissertation, University of Delaware, Newark, Delaware (1972).
17. Slattery, J.C., Phys. of Fluids, 7, 1913 (1964).

18. Middleman, S., "Flow of High Polymers", Interscience, New York (1968).

19. Astarita, G., Ind. Eng. Chem. Fundamentals, 6, 257 (1967).

20. Lodge, A.S., "Elastic Liquids", Academic Press, Inc., New York (1964).

21. Lodge, A.S., Trans. Farad. Soc., 52, 120 (1956).

22. Macdonald, I.F., and R.B. Bird, J. Phys. Chem., 70, 2068 (1966).

23. Meister, B.J., Trans. Soc. Rheol., 15, 63 (1971).

24. Spriggs, T.W., Huppler, J.D., and R.B. Bird, Trans. Soc. Rheol., 10(1), 191 (1966).

25. Bird, R.B., and T.W. Spriggs, Phys. of Fluids, 8(7), 1390 (1965).

26. Fredrickson, A.G., Chem. Eng. Sci., 17, 155 (1962).

27. Walters, K., Quant. J. Mech. and Appl. Math, 15(1), 63, (1962).

28. Ward, A.F.H., and G.M. Jenkins, Rheol. Acta, 1, 110 (1958).

29. Tanner, R.I., AIChE J., 15, 2, 177(1969).

30. Tanner, R.I., and J.M. Simmons, Chem. Eng. Sci., 22, 1803 (1967).

31. Bogue, D.C., IEC Fund., 5(2), 253 (1966).

32. Bernstein, B., Kearsley, E.A., and L. Zapas, Trans. Soc. Rheol., 7, 391 (1963).

33. Yamamoto, M., J. Phys.Soc. Japan, 14, 313 (1959).

34. Tanner, R.I., Trans. Soc. Rheol., 12, 155 (1968).

35. Dealy, J.M., Polym. Eng. Sci., 11, 433 (1971).

36. Bird, R.B., M.W. Johnson, and J.F. Stevenson, Proc. 5th Int. Cong. Rheol., 4, 159, Univ. Park Press, Baltimore (1970).

37. Markovitz, H., and B.D. Coleman, Adv. Appl. Mech., 8, 69 (1964).

38. Roscoe, R., Brit. J. Appl. Phys., 16, 1467 (1965).

39. Carreau, P.J., Ph. D. Dissertation, University of Wisconsin (1968).

40. Middleman, S., Trans. Soc. Rheol., 13, 123 (1969).

41. Stevenson, J.F., and R.B. Bird, Trans. Soc. Rheol., 15, 135 (1971).

42. Trouton, F.T., Proc. Roy. Soc., A77, 427 (1906).

43. Radushkevich, B.V., V.D. Fikhman, and G.V. Vinogradov, Mekh. Polimerov, 2, 343 (1968).

44. Ibid., Dokl. Akad. Nauk, USSR, 180, 404 (1968).

45. Vinogradov, G.V., V.D. Fikhman, and B.V. Radushkevich, and A. Ya. Malkin, J. Poly. Sci. A-2, 8, 657 (1970).

46. Stevenson, J.F., AIChE J., 18, 540 (1972).

47. Meissner, J., Rheol. Acta, 8, 78 (1969).

48. Meissner, J., Rheol. Acta, 10, 230 (1971).

49. Meissner, J., Trans. Soc. Rheol., 16, 405 (1972).

50. Chang, H., and A.S. Lodge, Rheol. Acta, 11, 127 (1972).

51. Bailey, E.D., Trans. Soc. Rheol., 18, 635 (1974).

52. Denson, C.D., and R.J. Gallo, Polym. Eng. Sci., 11, 174 (1971).

53. Joye, D.D., Ph.D. dissertation, Lehigh University (1972).

54. Maerker, J.M., and W.R. Schowalter, Rheol. Acta, 13, 627 (1974).

55. Glearson, G., and S. Middleman, unpublished paper (1975).

56. Cogswell, F.N., Rheol. Acta, 8, 187 (1969).

57. Nitschman, H., and J. Schrade, Helv. Chim. Acta, 31, 297 (1948).

58. Ziabicki, A., Kolloid Z., 175, 14 (1961).

59. Chen, I., G.E. Hagler, L.E. Abbott, D.C. Bogue and J.L. White, Trans. Soc. Rheol., 16, 473 (1972).

60. Han, C.D., and L. Segal, J. Appl. Poly. Sci., 14, 2973 (1970).

61. Acierno, D., J.N. Dalton, J.M. Rodriguez, and J.L. White, J. Appl. Poly. Sci., 15, 2395 (1971).

62. Spearot, J.A., and A.B. Metzner, Trans. Soc. Rheol., 16, 495 (1972).

63. Hudson, N.E., J. Ferguson, and P. Mackie, Trans. Soc. Rheol., 18, 541 (1974).

64. Acierno, D., G. Titomanlio, and L. Nicodemo, Rheol. Acta, 13, 532 (1974).

65. R.T. Balmer, unpublished paper.

66. Oliver, D.R. and R. Bragg, Rheol. Acta, 13, 830 (1974).

67. Coleman, B.D. and W. Noll, Arch. Rat. Mech. Anal., 6, 355 (1960).

68. R. Aris, "Vectors, Tensors, and the Basic Equations of Fluid Mechanics", Prentice-Hall, Englewood Cliffe, N.J., Ch. 10 (1962).

69. Wade, W.H., and R.S. Schechter, unpublished paper (1975)

70. Hyman, W.A., and R. Skalak, AIChE J., 18, 149 (1972).

71. Villadsen, J. and W.E. Stewart, Chem. Eng. Sci. 22, 1483 (1967).

72. Finlayson, B.A., "The method of weighted residuals and variational principles"., Academic Press 1972.

73. Leider, P.J., Ind. Eng. Chem., Fundam., 13, 342 (1974).

74. Fordham, S., Proc. Roy. Soc. (London), A194, 1 (1948).

75. Slattery, J.C., "Momentum, Energy, and Mass Transfer in Continua", McGraw-Hill (1972).

76. Weissenberg, K., "The testing of materials by means of the Rheogoniometer", Sangomo Control Limited .

77 Abdel-Khalik, S.I., O. Hassager, and R.B. Bird, J. Chem. Phys., 61, 4312 (1972).

78. Carreau, P.J., I.F. Macdonald and R.B. Bird, Chem. Eng. Sci., 23, 901 (1968).

79. Sutterby, J.L., Trans Soc. Rheol., 17, 559 (1973).

80. Heidemann, R.A., D. Sc. Thesis (1966), Washington University.

81. Han, C.D., Trans Soc. Rheol., 18, 163 (1974).

82. Goddard, J.D., Trans. Soc. Rheol., 11, 381 (1967).

APPENDIX I

EQUIPMENT SPECIFICATIONS AND CALIBRATIONS

I-1. Instruments

I-1-1. The Function Generator

(a) exponential potentiometer--Helipot Model NL5611-2054-0, from Beckman Instruments, Inc., Fullerton, California

(b) linear potentiometer--Helipot Model 5611 series from Beckman Instruments, Inc., Fullerton, California

(c) sinusoidal potentiometer--Helipot Model NL5713 R20k C50 SIN/COS, from Beckman Instruments, Inc., Fullerton, California

(d) stepper motors--Part Number KR45132-P2-S6-F3 and KL45132-P2-S6-F1, from A.W. Haydon Company, Waterbury, Connecticut

(e) stepper board (for controlling the rotational speed of the stepper motors)--Part Number 5000-77, from Houston Instrument, Bellaire, Texas

I-1-2. The Light Sensing Assembly

(a) photomultiplier tube--RCA 931A (9-stage, side-on type having S-4 spectral response), from RCA/Electronic Components, Harrison, New Jersey

(b) focus lens--Part Number 823575 Cannon Lens FL 50mm 1:1.8

(c) photomultiplier tube power supply--Model Number 472R (voltage ranging from 10 volts to 2110 volts), from Brandenburg, England

(d) light source--Kodak Carousel slide projector 600H with ELH Quartz lamp from Eastman Kodak Company, Rochester, New York

(e) blue filter--Part Number 26-5611, from Ealing Optics, Cambridge, Massachusetts

I-1-3. <u>Controller and Drive System</u>

(a) servo controller--Model NC 102F solid state dc servo controller from Control Systems Research, Inc., Pittsburgh, P.A.

(b) drive motor--Model Number 6VM-1-C172 from Micro Switch, Freeport, Illinois

I-1-4. <u>The Rotating Cylinder Assembly</u>

(a) glass cylinder--Precision bore pyrex tube (2" 0.001 I.D., 3/16" heavy wall, O.D. ground & polished, 24" long) from Wilmad Glass Co., Inc., Buena, New Jersey

(b) bearings--NDH Bearings Number 8506 (Bore diameter 1 3/16", O.D.=2 7/16"), from New Departure Hyatt Bearings, Division of General Motors Corporation, Sandusky, Ohio

(c) temperature controller--Model 400, from Victory Engineering Co., Perkasie, P.A.

I-1-5. The Measurement Apparatus

(a) recorder 1--Omniscribe two-pens recorder, from Houston Instrument, Bellaire, Texas

(b) recorder 2--Model 320 Sanborn dual channels dc amplifier recorder, from Sanborn Division, Hewlett Packard, Waltham, Massachusetts

(c) digital voltmeter--Series CX-2, from Non-linear System, Inc., Del Mar, California

(d) logarithmic amplifier--Model 4350, from Teledyne Philbrick, Burlington, Massachusetts

I-2. The Electronic Diagrams of the Analog Devices

I-2-1. The Function Generator--The electronic diagram is shown in Fig.I-1. By adjusting the positions of Switches FA and FB in Fig.I-1, a signal ranging from 0 to 10 volts with specific functional characteristics (exponential, linear, and sinusoidal) can be produced at point P.

Since the rotational speed of the stepper motor is controlled by the stepper board, the frequency of the sinusoidal function, the $\bar{\beta}$ in the exponential function $e^{\bar{\beta}t}$, and the slope of the linear function are dependent upon the speed settings in the stepper board.

I-2-2. The Controller--Fig.I-2 shows the electronic diagram of the controller. The gain of the controller is adjustable by changing the resistance in the variable resistor R_i in Fig.I-2. Terminals 1 and 2 are the inputs to the con-

Figure I-1 Electronic Diagram of the Function Generator.

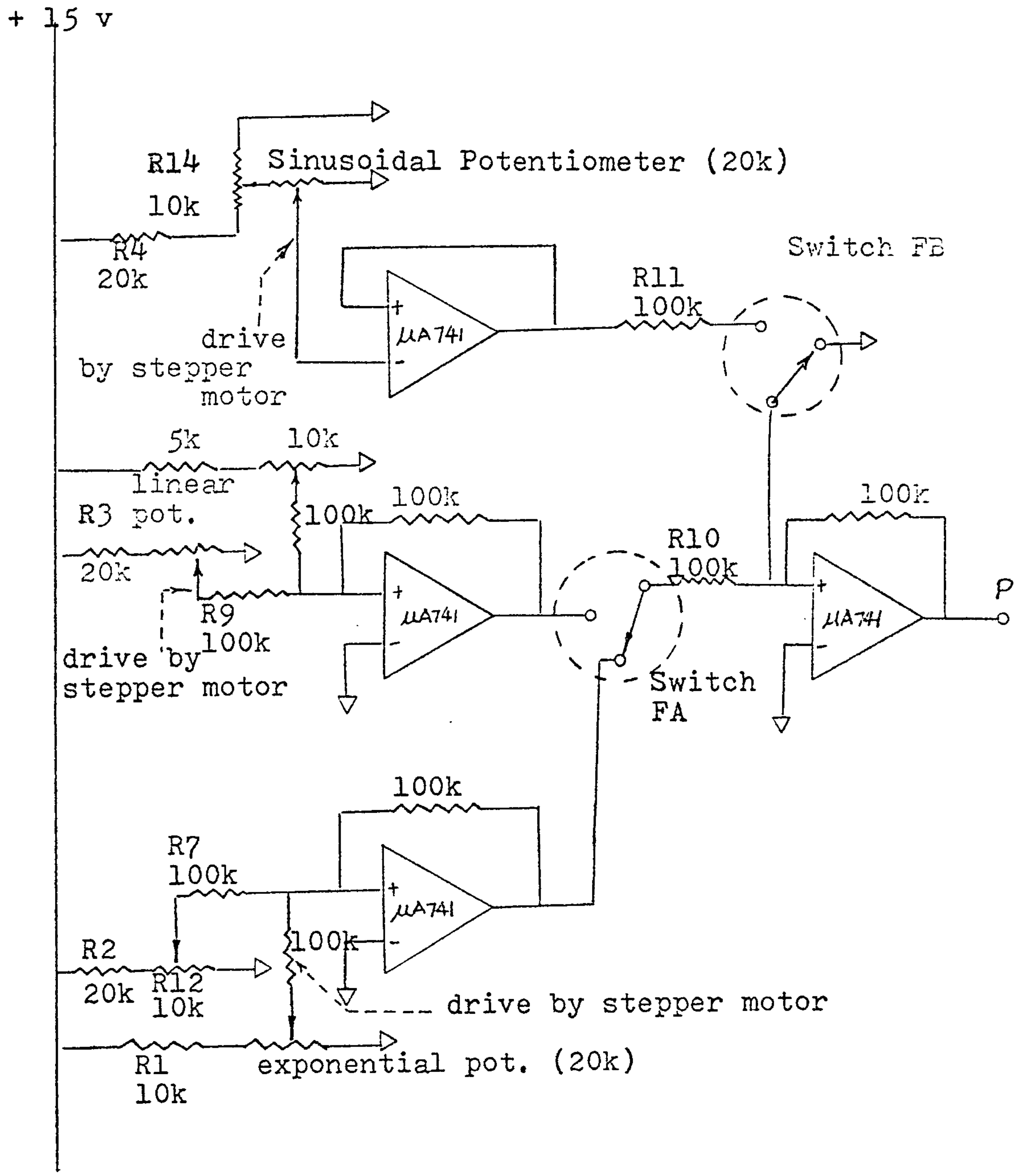

Figure I-2 The Circuit of the Controller

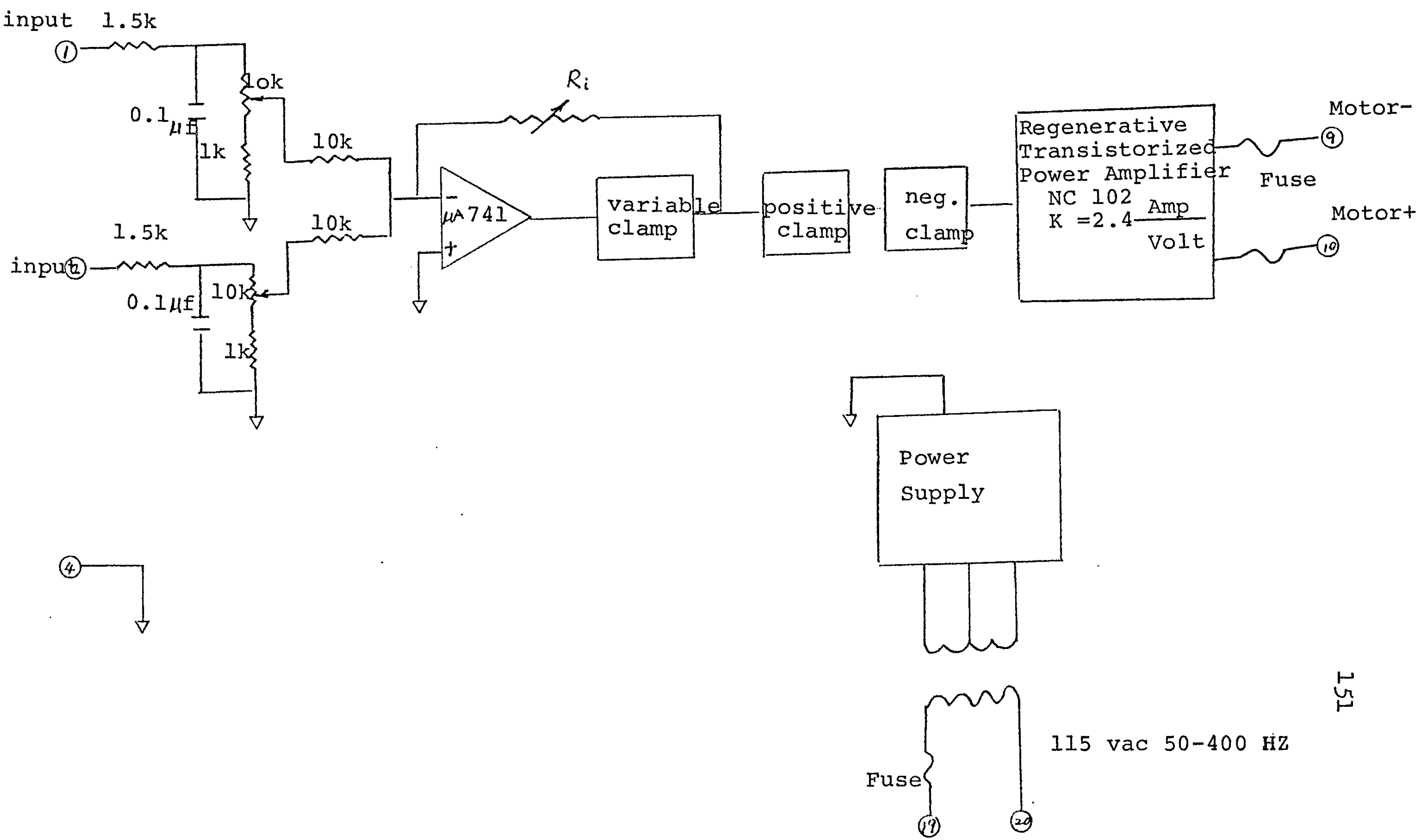

troller while Terminals 9 and 10 are the outputs and are connected to the drive motor.

I-2-3. The Multiplier--The electronic diagram and the electronic components of the multiplier are shown in Fig. I-3. Both the input and the output of the multiplier are limited between 0 and 10 volts. It should be noted that the output of the multiplier is equal to 1/10 of the expected value. For example, with input 1=1 volt and input 2=2 volts, the output of the multiplier is equal to $\frac{\text{Input 1} \times \text{Input 2}}{10} = 0.2$ volts.

If input 1 is equal to input 2, the multiplier then becomes a square device.

I-2-4. The Quadratic Inverter--Based on the calibrations described in Section 3-5-1, the quadratic inverter was used for converting the signal S_P from the photomultiplier tube to the signal S_D which is quantitatively proportional to the drop diameter D. The electronic diagram of the quadratic inverter is shown in Fig I-4. Block T is a square device as described in Section I-2-3. Switch S-1 is a 5 poles-5 position switch. The positions of the Switch S-1 and the resulting electronic connections are listed in Table I-1.

I-2-5. The amplifier--For a given input voltage x, the output voltage of an amplifier with gain R is Rx. The electronic diagram of the amplifier is shown in Fig. I-5. The values

Figure I-3 The Circuit of the Multiplier

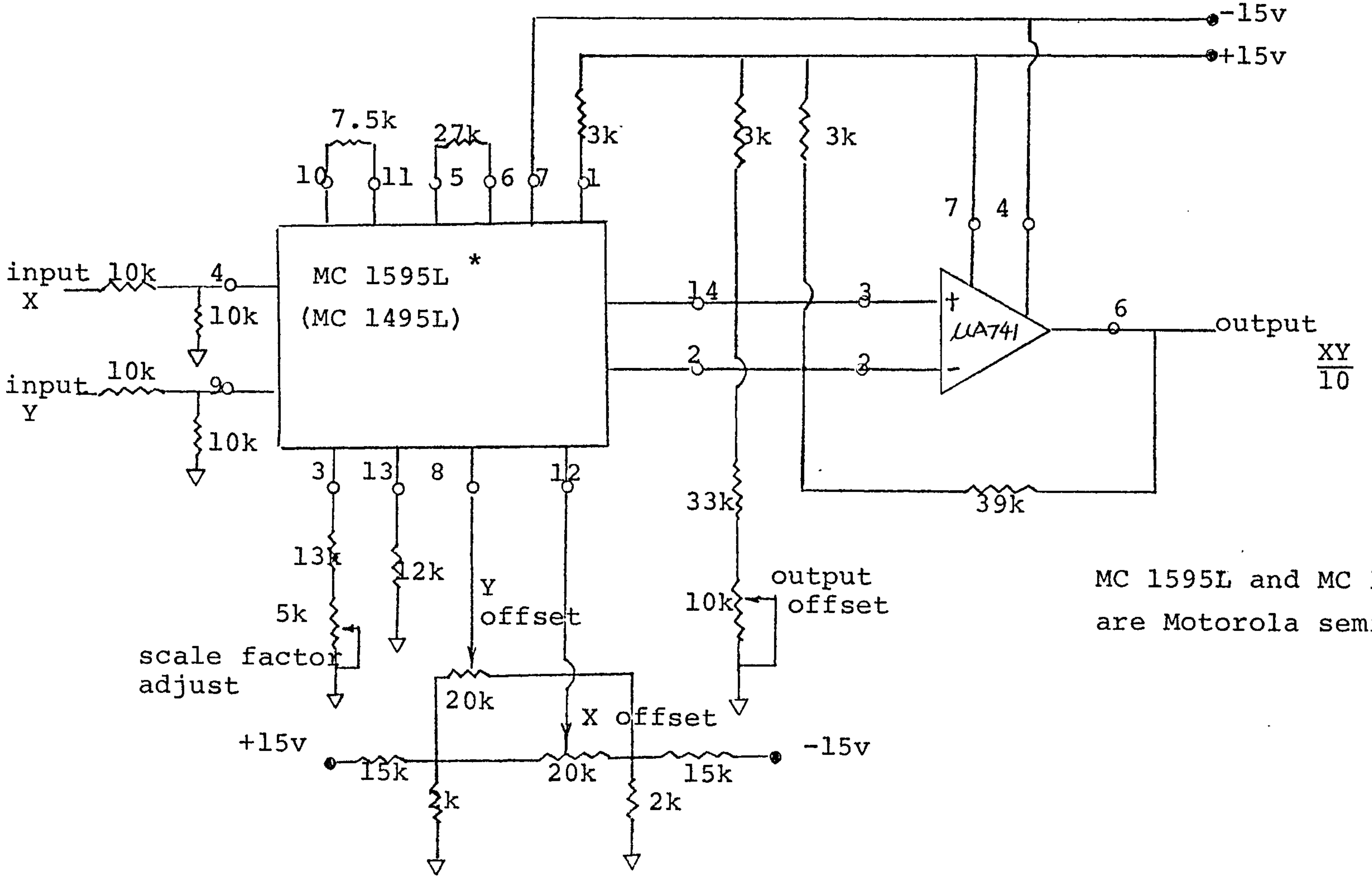

MC 1595L and MC 1495L* are Motorola semiconductor

Figure I-4 The Circuit of the Quadratic Inverter

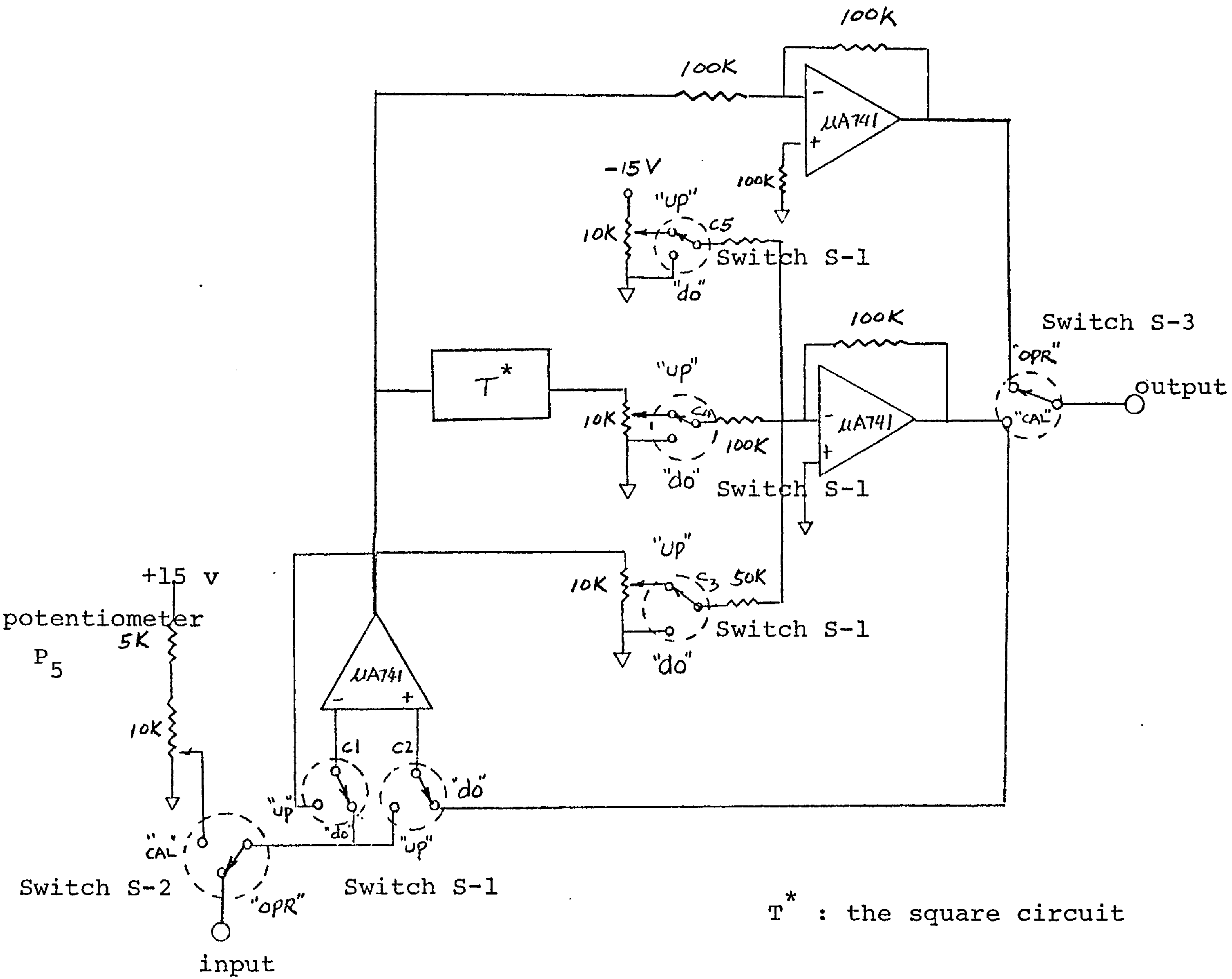

T* : the square circuit

Position / Connection	1	2	3	4	5
C_1	"do"	"up"	"up"	"up"	"up"
C_2	"do"	"up"	"up"	"up"	"up"
C_3	"up"	"up"	"do"	"up"	"do"
C_4	"up"	"up"	"up"	"do"	"do"
C_5	"up"	"up"	"do"	"do"	"up"

Table I-1 The Positions of Switch S-1 in the Quadratic Inverter and the Resulting Connections

Figure I-5 The Circuit of the Amplifier

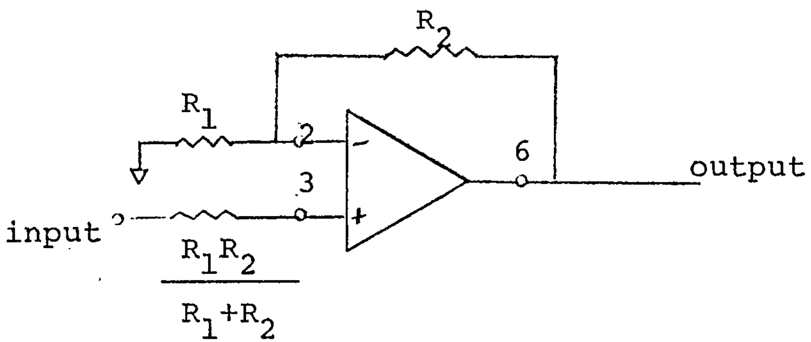

Table I-2 The Values of the Resistors in the Amplifier and the Resulting Gain

Gain R	R_1	R_2
1	1 kΩ	9 kΩ
100	100 Ω	9.9 kΩ
1000	100 Ω	99.9 kΩ

of resistor R_1 and R_2 and the resulting gain $\mathcal{R}$ are listed in Table I-2.

I-2-6. Inverter--Fig.I-6 shows the electronic diagram of the inverter. The function of the inverter is to generate an output signal having the same voltage level as the input but with opposite polarity.

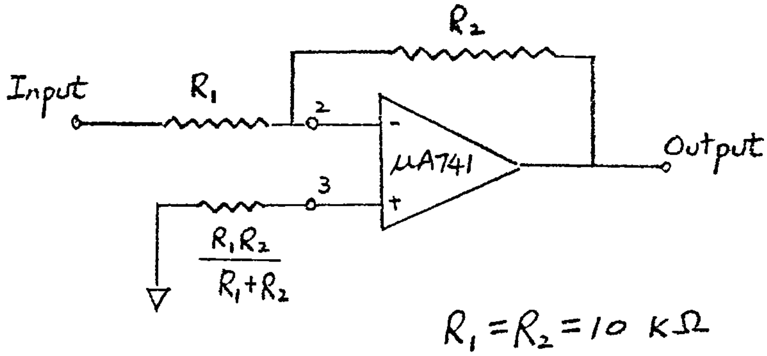

Figure I-6. The Circuit of the Inverter

I-3. Calibrations of the Analog Devices

I-3-1. Calibration of the Multiplier

To obtain the maximum accuracy of the output signal, the multiplier must be frequently calibrated. The calibrating procedures for the multiplier are as follows:

Step 1. For the X input offset

(a) Connect Oscillator (1 KH_z, 5 V_{pp} sinewave) to the "Y" input (pin 4).

(b) Connect "X" input (pin 9) to ground.

(c) Adjust X offset potentiometer P_2 for an ac null at the output.

Step 2. For the Y input offset

(a) Connect Oscillator (1 KH_z, 5 V_{pp} sinewave) to the "X" input (pin 9)

(b) Connect "Y" input (pin 4) to ground.

(c) Adjust "Y" offset potentiometer P_1, for an ac null at the output.

Step 3. For the output offset

(a) Connect both "X" and "Y" input to ground.

(b) Adjust output potentiometer P_4, until the output voltage is zero volts dc.

Step 4. For the scale factor

(a) Apply + 10 volt dc to both the "X" and "Y" inputs.

(b) Adjust P_3 to achieve +10.0 volt at the output.

Step 5. Repeat steps 1 through 4 as necessary.

I-3-2. Calibration of the Amplifier

The amplifier with gain k is calibrated as follows:

Step 1. Connect the input to ground.

Step 2. Adjust the offset potentiometer until the output voltage is zero volts dc.

Step 3. Apply +1 volt dc to the input.

Step 4. Adjust the gain potentiometer to achieve the expected output value, i.e. input=1 volt and k=4, then the expected output is kx=4x1 =4 volts.

Step 5. Repeat steps 1 through 4 as necessary.

I-3-3. Calibration of the Quadratic Inverter

For a given set of a, b, and c values and the input voltage x_I, the quadratic inverter with three adjustable potentiometers can produce an output signal x_o according to the following equation:

$$x_I = ax_o^2 - bx_o + c \qquad \text{(I-3-1)}$$

The procedures for setting the values of a, b, and c in the quadratic inverter are as follows:

(i) Setting the value of a

Step 1. Set the Switch S-1 in position "3".

Step 2. Set the Switch S-2 in position "CAL".

Step 3. Set the Switch S-3 in position "OPR".

Step 4. Turn the potentiometer P5 until the output of the quadratic inverter is -2 volts.

Step 5. Set the Switch S-3 in position "CAL".

Step 6. Turn the potentiometer A until the output of the quadratic inverter reachs the expected value of (-0.4a), i.e. if a=2, then the expected value is -0.8 volts.

(ii) Setting the value of b

Step 1. Set the Switch S-1 in position "4".

Step 2. Set the Switch S-2 in position "CAL".

Step 3. Set the Switch S-3 in position "OPR".

Step 4. Turn the potentiometer P5 until the output of the quadratic inverter is -2 volts.

Step 5. Set the Switch S-3 in position "CAL".

Step 6. Turn the potentiometer B until the output of the quadratic inverter reachs the expected value of (-2b), i.e., if b=2, then the expected value is -4 volts.

(iii) Setting the value of c

Step 1. Set the Switch S-1 in position "5".

Step 2. Set the Switch S-3 in position "CAL".

Step 3. Turn the potentionmeter C until the output of the quadratic inverter is equal to the value of c.

It should be noted that after completing the procedures for setting the values of a, b, and c, Switches S-1, S-2, and S-3 should be turned to positions "1", "OPR", and "OPR" respectively. In that case, for a given input x_I, the quadratic inverter will generate an output x_o according to Equation (I-3-1).

I-4. Theory of Control

Two different types of experiments- stress growth and approximate creep were performed in the drop elongation apparatus. In the stress growth experiments, the drop diameter is required to decrease exponentially with time while in the approximate creep experiments, the product of the rotational speed ω and the drop diameter D is held constant throughout the course of experiments.

To achieve the desired behavior of the drop diameter and ωD in respective stress growth and approximate creep experiments, two feedback control loops were used in the drop elongation apparatus. The block diagrams of the feedback loops are shown in Fig. I-7 for

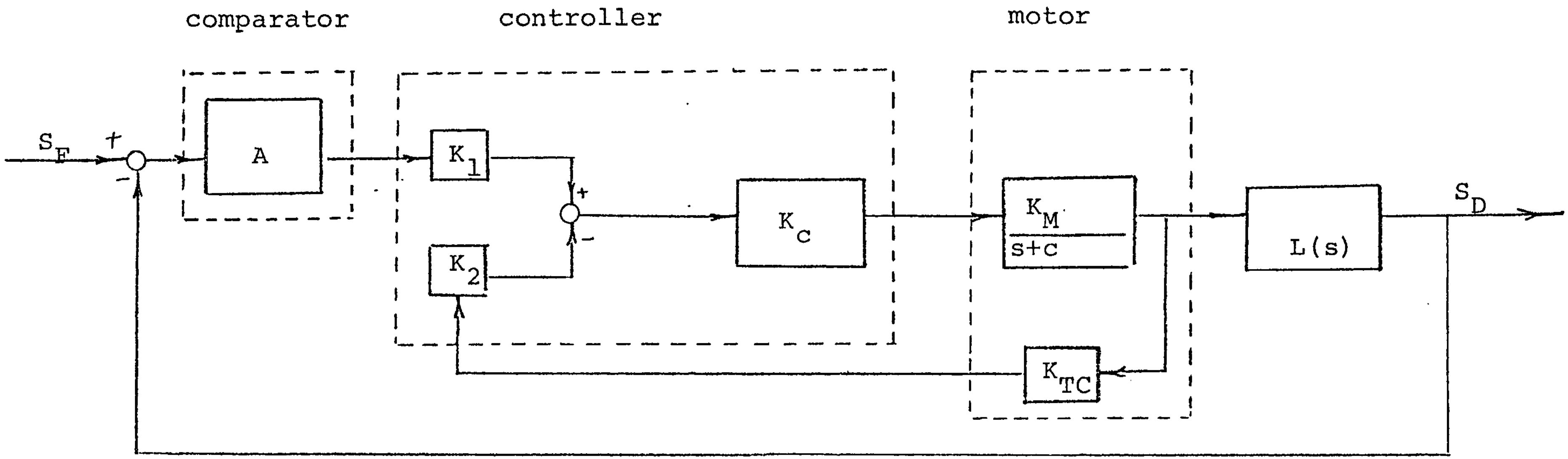

Figure I-7 The Closed-Loop Block Diagrams in the Stress Growth Experiment the stress growth and in Fig. I-8 for the approximate creep experiments where

S_F= signal from the function generator

S_D= controlled signal

A = gain of the comparator

K_c= gain of the controller

K_1, K_2= scale factors

K_m= gain of the motor

c = characteristic constant of the motor

K_{TC}= the tachometer constant

G(s)= the transfer function of a lumped device including the rotating cylinder, the light sensing assembly, the drop response, the amplifier, the quadratic inverter, and the logarithmic amplifier.

L(s)= the transfer function of a lumped device including the rotating cylinder, the light sensing assembly, the drop device, the amplifier, and the quadratic inverter.

The closed loop block diagrams in Figs. I-7 and I-8 can be reduced to the open loop diagrams in Figs I-9 and I-10 respectively.

To achieve the desired control response without knowing L(s) and G(s), the following relations must be satisfied

$$AK_1K_cK_mL(S) \ggg (s+c+K_cK_mK_{TC}) \text{ for the stress growth experiment} \quad \text{(I-4-1)}$$

$$AK_1K_cK_m\sqrt{G(s)K_{TC}} \ggg \frac{\sqrt{S_D}}{S_F}(s+c+K_{TC}K_2K_cK_m) \text{ for the approximate creep experiment} \quad \text{(I-4-2)}$$

Both equations can be satisfied by employing a large gain A of the comparator.

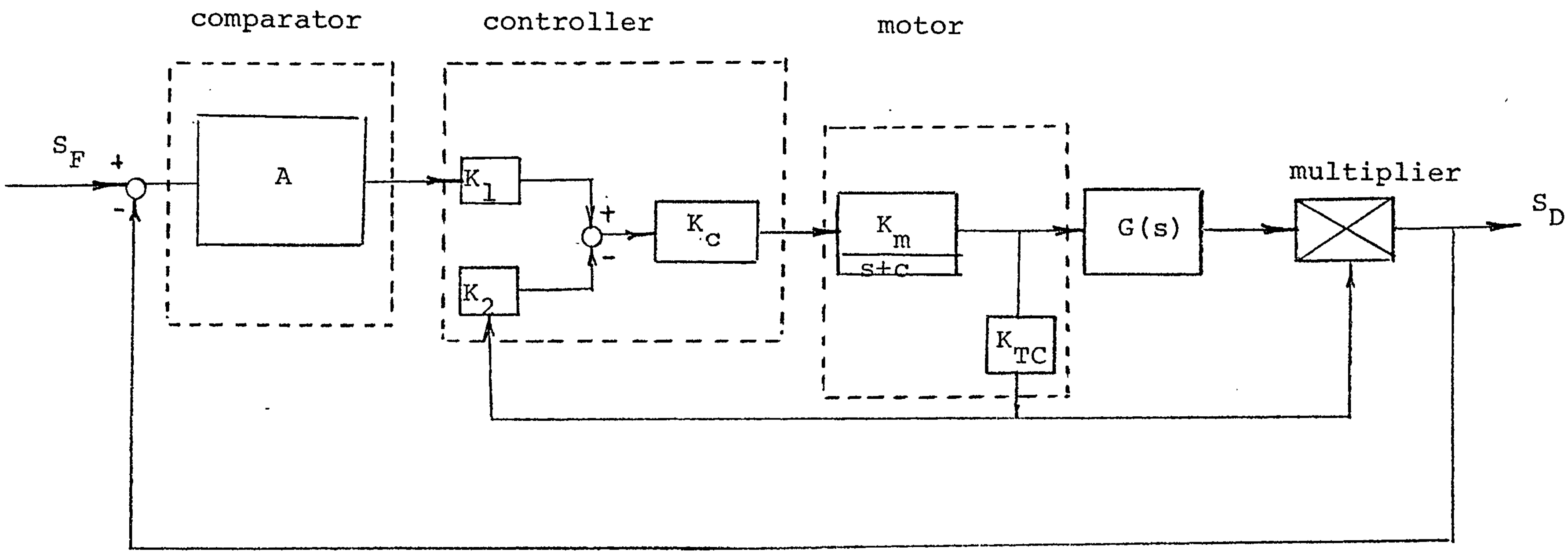

Figure I-8 The Closed-Loop Block Diagrams in the Approximate Creep Experiment

Figure I-9 The Open-Loop Block Diagrams in the Stress Growth Experiment

$$S_F \longrightarrow \boxed{\dfrac{AK_1K_cK_mL(s)}{s+c+K_cK_mK_{TC}+AK_1K_cK_mL(s)}} \longrightarrow S_D$$

Figure I-10 The Open-Loop Block Diagrams in the Approximate Creep Experiment

$$S_F \longrightarrow \boxed{\quad U(s) \quad} \longrightarrow S_D$$

$$U(s)= \frac{AK_1K_cK_m\sqrt{G(s)K_{TC}} - \sqrt{\dfrac{S_D}{S_F}}(s+c+K_{TC}K_2K_mK_c)}{AK_1K_cK_m\sqrt{G(s)K_{TC}}}$$

APPENDIX II

SELECTION OF COLLOCATION POINTS IN USING ORTHOGONAL COLLOCATION METHOD

In Section 4-2-2, the unknown coefficients C_m (m=2,4,6..) in Equation (4-2-32) were determined at any instant of time by using two approximate method: the least square and the orthogonal collocation. In the latter regard, a set of collocation points must be selected at which Equation (4-2-32) is satisfied. In this appendix the way of selecting the collocation points is described.

Since τ_{rr}, $\tau_{r\theta}$, and $\tau_{\theta\theta}$ can be related to the stream function ψ through the Newton's law of viscosity, Equation (4-2-14) and (4-2-22) can be generalized as

$$L^V(\psi) = 0 \qquad \text{in V} \qquad \text{(II-1)}$$

and

$$L^S(\psi) = 0 \qquad \text{on S} \qquad \text{(II-2)}$$

respectively, where S is the drop surface, V is the drop domain (volume), and L^V and L^S are the respective partial differential-equation and boundary-condition operator.

As shown in Section 4-2-2, a function ψ_T is found to satisfy Equation (II-1) as

$$\psi_T^{(n)} = C_2^{(n)} r^3 \bar{P}_2(\hat{\eta}) + \sum_{m=2}^{2(n-1)} C_{m+2}^{(n)} \left(\bar{P}_{m+2}(\hat{\eta}) + \frac{m+1}{m+2} \bar{P}_m(\hat{\eta}) \right) r^{m+3} \qquad \text{(II-3)}$$

where $\bar{P}_m(\hat{\eta}) = \int_{-1}^{\hat{\eta}} P_m(\eta')\,d\eta'$, $P_m(\hat{\eta})$ is the Legendre Polynomial of degree m, $\hat{\eta}$ is defined as $\cos\theta$, and C_m (m=2,4,6...) are undetermined constants.

By substituting Equation (II-3) into Equation (II-2), the boundary residual is obtained,

$$R_n = L^s(\psi_T^{(n)}) \qquad \text{(II-4)}$$

Analogous to Galerkin's method, the boundary residual was made to be orthogonal to a set of orthogonal polynomials P_i with degree $i<n$ on the drop surface S.

$$\int_S L^s(\psi_T^{(n)})\,P_i\,dS = 0 \qquad \text{(II-5)}$$

where P_i is yet to be specified.

Noting that ds is equal to $R_D d\theta$ (R_D and θ are defined in the coordinate system shown in Fig. 4-4) and $x = \cos^2\theta$, Equation (II-5) becomes

$$2\int_0^1 R_D L^s(\psi_T^{(n)})\,P_i\,(x^{-\frac{1}{2}})(1-x)^{-\frac{1}{2}}\,dx = 0 \qquad \text{(II-6)}$$

Hence, once $\psi_T^{(n)}$ has been adjusted to satisfy $R_D L^s(\psi_T^{(n)}) = 0$ at n collocation points, $x_1, \ldots x_n$, the function $R_D L^s(\psi_T^{(n)})$ either vanishes everywhere or contains a polynomial factor $G_n(x)$ of degree n in x whose zeroes are the collocation points. Thus, the collocation points are chosen by specifying that $R_D L^s(\psi_T^{(n)})$ is orthogonal to all the functions $P_i(x)$ with respect to the weight function $x^{-\frac{1}{2}}(1-x)^{-\frac{1}{2}}$ on the interval $[0,1]$. This specification is automatically satisfied by taking $R_D L^s(\psi_T^{(n)})$ and $P_i(x)$ from the orthogonal polynomial set defined by

$$\int_0^1 x^{-\frac{1}{2}}(1-x)^{-\frac{1}{2}}\,P_i(x)\,P_n(x)\,dx = 0 \qquad \text{(II-7)}$$

for all positive integers i,n and $i \neq n$.

The polynomials defined by Equation (II-7) are Jacobi Polynomials. Hence, the n collocation points used in the numerical simulation in Section 4-2-2 are the zeroes of the Jacobi Polynomials of degree n.

APPENDIX III

SHEAR AND OSCILLATORY DATA

Table III-1. Shear Data of PIB

Shear Rate (sec^{-1})	Viscosity (poise)	Normal Stress Difference ($dyne/cm^2$)
0.043	6850	-
0.054	6540	-
0.068	6421	-
0.085	6300	-
0.108	6190	-
0.136	5800	-
0.17	5442	-
0.215	5190	-
0.27	5000	-
0.34	4564	-
0.43	4366	-
0.54	4030	2254
0.68	3970	2772
0.85	3744	3433
1.08	3300	4283
1.36	3150	5184
1.7	2880	7018
2.15	2608	7913
2.7	2454	9860
3.41	2302	12220
4.3	2203	15120
5.4	1989	17440
6.8	1950	19940
8.54	1820	23510
10.8	1750	25850
13.6	1601	27830
17.1	1405	-

Table III-2. Oscillatory Data of PIB

Frequency (sec^{-1})	Dynamic Viscosity (poise)	Dynamic Rigidity (dyne/cm^2)
0.0299	6700	-
0.0377	6650	5.13
0.0475	6430	-
0.06	6400	59.33
0.0754	6213	97.4
0.0950	6187	142.5
0.1194	5948	196.9
0.150	5500	260
0.188	5200	337
0.238	4600	428.3
0.299	4225	533
0.377	3750	657.3
0.4750	3652	734
0.6	3322	874
0.754	3202	1045
0.95	2899	1272
1.194	2703	1575
1.5	2480	1834
1.88	2250	2182
2.38	2050	2539
2.99	1956	3132
3.77	1745	4234
4.75	1555	4800
6.0	1467	5906
7.54	1321	5505
9.425	1361	6227
11.9	1120	5812
14.95	1002	-

Table III-3. Shear Data of PAA

Shear Rate (sec^{-1})	Viscosity (poise)	Normal Stress Difference ($dyne/cm^2$)
0.0054	9602	-
0.0068	9500	-
0.0085	9480	-
0.0108	9168	-
0.0136	7903	-
0.017	6700	-
0.022	6154	-
0.027	5317	-
0.0342	4645	-
0.043	4183	-
0.054	3439	-
0.068	3161	-
0.0855	2652	-
0.108	2308	-
0.136	1980	-
0.17	1690	-
0.215	1402	-
0.271	1210	-
0.34	900	-
0.43	780	-
0.54	720	-
0.68	530	-
0.855	470	1216
1.08	390	1700
1.36	340	2000
1.7	280	2172
2.15	240	2508
2.71	195.5	2800
3.4	172	3051
4.3	145	3427
5.4	119	4067
6.8	100	4387
8.54	88	4702
10.8	73	5984
13.6	68	6543
17.1	60.5	7642
21.5	53	8806
27.1	46	10570
34.2	35.2	12000
54.1	28.5	14500
85.4	20.5	20450

Table III-4. Oscillatory Data of PAA

Frequency (sec^{-1})	Dynamic Viscosity (poise)	Dynamic Rigidity ($dyne/cm^2$)
0.006	8691	-
0.0075	8450	32.1
0.0095	8000	36.7
0.012	6902	39.8
0.015	5802	47.0
0.0188	5300	61.0
0.0238	4500	73.0
0.03	4005	85.5
0.0377	3200	98.3
0.0475	2650	112.0
0.06	2102	127.6
0.075	1737	135.0
0.095	1415	158.0
0.12	1261	177.0
0.15	1095	183.0
0.188	856.9	220
0.238	742	237
0.299	600	256.8
0.377	498	281.0
0.475	400.5	294.0
0.596	358	321.4
0.754	285.5	351.5
0.95	230.2	373.4
1.2	190.1	398.0
1.5	163.0	429.0
1.88	134.5	451.0
2.38	112.7	486.0
2.99	91.8	510.0
3.77	75.6	549.0
4.75	61.7	579.5
5.95	50.3	666.0
7.54	41.3	688
9.43	33.6	710
11.9	27.7	796
15.0	24.4	878
18.85	19.0	989
23.81	19.4	1120

APPENDIX IV

EXTENSIONAL DATA

IV-1. Stress Growth Data

Table IV-1-1. Stress Growth Data of Newtonian Silicone Oil at $\dot{\gamma} = 0.003\ sec^{-1}$

Time (sec)	Radius (cm)	$(\pi_{zz} - \pi_{rr})$ (dyne/cm²)	Instantaneous Extensional Viscosity (poise)
0	0.4134	0	0
1	0.413	40	15440
2	0.4125	51	19591
3	0.412	48	18708
4	0.4114	47	18423
5	0.4109	39	15082
6	0.4103	38	15169
7	0.4100	45	17577
8	0.4090	47	18076
9	0.4085	46	17781
10	0.408	40	15576

IV-1. Stress Growth Data

Table IV-1-2. Stress Growth Data of Newtonian Silicone oil at $\dot{\gamma} = 0.005\ \text{sec}^{-1}$

Time (sec)	Radius (cm)	$(\Pi_{zz} - \Pi_{rr})$ (dyne/cm^2)	Instantaneous Extensional Viscosity (poise)
0	0.396	0	0
0.5	0.396	65	13014
1	0.395	80	16016
2	0.393	87	17973
3	0.392	84	16706
4	0.391	86	17327
5	0.390	92	18432
6	0.389	86	17136
7	0.388	84	16796
8	0.387	84	16939
9	0.386	85	17074
10	0.385	84	16722

Table IV-1-3. Stress Growth Data of Newtonian Silicone Oil at $\dot{\gamma} = 0.0077\ sec^{-1}$

Time (sec)	Radius (cm)	$(\Pi_{zz} - \Pi_{rr})$ (dyne/cm^2)	Instantaneous Extensional Viscosity (poise)
0	0.377	0	0
0.5	0.377	113	14555
1	0.376	136	17624
2	0.374	146	18913
3	0.373	143	18580
4	0.372	133	17215
5	0.370	135	17453
6	0.369	135	17516
7	0.367	125	16297
8	0.366	124	16097
9	0.364	123	15889
10	0.363	123	15876

Table IV-1-4. Stress Growth Data of Newtonian Silicone Oil at $\dot{\gamma} = 0.0133 sec^{-1}$

Time (sec)	Radius (cm)	$(\Pi_{zz} - \Pi_{rr})$ (dyne/cm2)	Instantaneous Extensional Viscosity (poise)
0	0.368	0	0
0.5	0.367	149	11202
1	0.365	220	16555
2	0.363	249	18756
3	0.361	244	18393
4	0.358	242	18246
5	0.356	242	18247
6	0.353	244	18387
7	0.351	238	17980
8	0.349	215	16190
9	0.346	221	16672
10	0.344	228	17155

Table IV-1-5. Stress Growth Data of Newtonian Silicone Oil at $\dot{\gamma}$ = 0.015 sec^{-1}

Time (sec)	Radius (cm)	$(\Pi_{zz} - \Pi_{rr})$ (dyne/cm^2)	Instantaneous Extensional Viscosity (poise)
0	0.321	0	0
1	0.320	264	17595
2	0.318	262	17472
3	0.315	279	18603
4	0.313	281	18734
5	0.311	276	18403
6	0.308	268	17828
7	0.306	258	17244
8	0.303	251	16754
9	0.301	244	16250
10	0.299	245	16290

Table IV-1-6. Stress Growth Data of Newtonian Silicone Oil at $\dot{\gamma} = 0.0171\ sec^{-1}$

Time (sec)	Radius (cm)	$(\Pi_{zz} - \Pi_{rr})$ (dyne/cm2)	Instantaneous Extensional Viscosity (poise)
0	0.324	0	0
0.5	0.323	159	9277
1	0.320	292	17038
2	0.318	294	17154
3	0.316	314	18270
4	0.313	305	17831
5	0.310	304	17724
6	0.308	304	17780
7	0.305	296	17295
8	0.3024	296	17320
9	0.300	269	15744
10	0.297	260	15204

Table IV-1-7. Stress Growth Data of Newtonian Silicone Oil at $\dot{\gamma}$ = 0.0193 sec^{-1}

Time (sec)	Radius (cm)	$(\Pi_{zz} - \Pi_{rr})$ (dyne/cm^2)	Instantaneous Extensional viscosity (poise)
0	0.390	0	0
0.5	0.391	142	7356
1	0.389	293	15170
2	0.387	328	17033
3	0.382	348	18053
4	0.379	352	18280
5	0.375	369	19130
6	0.372	332	17223
7	0.368	325	16880
8	0.365	317	16471
9	0.361	329	17097
10	0.358	325	16856

Table IV-1-8. Stress Growth Data of Newtonian Silicone Oil at $\dot{\gamma} = 0.03\ sec^{-1}$

Time (sec)	Radius (cm)	$(\Pi_{zz} - \Pi_{rr})$ (dyne/cm^2)	Instantaneous Extensional Viscosity (poise)
0	0.401	0	0
0.5	0.400	188	6274
1	0.397	522	17401
2	0.391	548	18247
3	0.385	541	18034
4	0.379	527	17565
5	0.374	521	17367
6	0.368	505	16811
7	0.363	496	16538
8	0.357	492	16384
9	0.352	487	16248
10	0.347	476	15887

Table IV-1-9. Stress Growth Data of PIB at $\dot{\gamma} = 0.0055\ sec^{-1}$

Time (sec)	Radius (cm)	$(\Pi_{zz} - \Pi_{rr})$ (dyne/cm^2)	Instantaneous Extensional Viscosity (poise)
0	0.335	0	0
1	0.334	22	4120
2	0.333	39	7003
3	0.332	61	11100
4	0.331	102	18502
5	0.330	105	19002
6	0.329	110	20127
7	0.329	111	20349
8	0.328	115	20988
9	0.327	113	20510
10	0.326	104	20530
11	0.325	107	19546

Table IV-1-10. Stress Growth Data of PIB at $\dot{\gamma} = 0.0082\ sec^{-1}$

Time (sec)	Radius (cm)	$(\Pi_{zz} - \Pi_{rr})$ (dyne/cm^2)	Instantaneous Extensional Viscosity (poise)
0	0.309	0	0
1	0.308	41	5130
2	0.306	58	7040
3	0.306	82	10050
4	0.304	100	12283
5	0.303	106	13001
6	0.302	122	15400
7	0.301	152	18571
8	0.300	167	20494
9	0.299	170	20778
10	0.298	165	20226
11	0.296	163	19941
12	0.295	174	21362
13	0.294	178	21856
14	0.293	176	21588

Table IV-1-11. Stress Growth Data of PIB at $\dot{\gamma}$ = 0.0086 sec^{-1}

Time (sec)	Radius (cm)	$(\Pi_{zz}-\Pi_{rr})$ (dyne/cm^2)	Instantaneous Extensional Viscosity (poise)
0	0.313	0	0
1	0.313	22	2482
2	0.310	59	6909
3	0.310	60	6971
4	0.309	82	9585
5	0.308	103	12009
6	0.307	110	12869
7	0.306	139	16144
8	0.305	154	18046
9	0.303	176	20509
10	0.303	171	19851
11	0.301	180	21011
12	0.301	169	19616
13	0.299	174	20342
14	0.298	172	20162
15	0.296	188	20854

Table IV-1-12. Stress Growth Data of PIB at $\dot{\gamma}$ = 0.0107 sec^{-1}

Time (sec)	Radius (cm)	$(\Pi_{zz}-\Pi_{rr})$ (dyne/cm²)	Instantaneous Extensional Viscosity (poise)
0	0.303	0	0
1	0.301	42	3962
2	0.300	79	7383
3	0.298	104	9738
4	0.297	103	9671
5	0.295	117	10982
6	0.294	176	16476
7	0.292	167	15668
8	0.291	160	15000
9	0.290	185	17243
10	0.288	197	18451
11	0.287	179	16800
12	0.286	206	19261
13	0.283	200	18699
14	0.283	210	19655
15	0.279	203	19014

Table IV-1-13. Stress Growth Data of PIB at $\dot{\gamma} = 0.01307\ sec^{-1}$

Time (sec)	Radius (cm)	$(\Pi_{zz} - \Pi_{rr})$ (dyne/cm^2)	Instantaneous Extensional Viscosity (poise)
0	0.334	0	0
1	0.332	52	4001
2	0.330	105	8002
3	0.328	130	9957
4	0.325	170	13007
5	0.323	196	15004
6	0.321	242	18502
7	0.319	268	20502
8	0.317	289	22120
9	0.315	298	22791
10	0.313	312	23831
11	0.311	309	23587
12	0.309	308	23597
13	0.307	305	23340

Table IV-1-14. Stress Growth Data of PIB at $\dot{\gamma}$ = 0.0156 sec^{-1}

Time (sec)	Radius (cm)	$(\Pi_{zz} - \Pi_{rr})$ (dyne/cm^2)	Instantaneous Extensional Viscosity (poise)
0	0.352	0	0
1	0.351	60	3848
2	0.348	102	6525
3	0.346	140	8967
4	0.344	174	11131.4
5	0.342	214	13720
6	0.339	252	16119
7	0.337	269	16236
8	0.335	380	22965
9	0.333	370	22346
10	0.331	373	22576
11	0.328	389	23939
12	0.326	408	24690
13	0.323	404	24434
14	0.321	408	24640

Table IV-1-15. Stress Growth Data of PIB at $\dot{\gamma} = 0.01564\ sec^{-1}$

Time (sec)	Radius (cm)	$(\Pi_{zz} - \Pi_{rr})$ (dyne/cm^2)	Instantaneous Extensional Viscosity (poise)
0	0.394	0	0
1	0.391	124	8275
2	0.388	181	12037
3	0.385	229	15272
4	0.383	287	19124
5	0.380	285	18913
6	0.377	327	21757
7	0.375	337	22479
8	0.372	354	23657
9	0.369	379	25302
10	0.366	384	25564
11	0.364	388	25881
12	0.361	386	25686

Table IV-1-16. Stress Growth Data of PIB at $\dot{\gamma}$ = 0.0161 sec^{-1}

Time (sec)	Radius (cm)	$(\Pi_{zz}-\Pi_{rr})$ (dyne/cm^2)	Instantaneous Extensional Viscosity (poise)
0	0.312	0	0
1	0.310	157	9829
2	0.307	221	13761
3	0.305	260	16161
4	0.302	345	21453
5	0.300	529	26665
6	0.298	500	31089
7	0.295	496	30848
8	0.293	488	30343
9	0.290	448	27846
10	0.288	479	29815
11	0.286	467	29036

Table IV-1-17. Stress Growth Data of PIB at $\dot{\gamma} = 0.0163\ sec^{-1}$

Time (sec)	Radius (cm)	$(\Pi_{zz} - \Pi_{rr})$ (dyne/cm^2)	Instantaneous Extensional Viscosity (poise)
0	0.351	0	0
1	0.347	125	7668
2	0.345	203	12470
3	0.344	253	15557
4	0.341	324	19883
5	0.339	348	21356
6	0.336	388	23765
7	0.334	399	24512
8	0.332	432	26559
9	0.329	437	26809
10	0.327	449	27511
11	0.324	444	27283
12	0.322	450	27584

Table IV-1-18. Stress Growth Data of PIB at $\dot{\gamma} = 0.018\ sec^{-1}$

Time (sec)	Radius (cm)	$(\Pi_{zz} - \Pi_{rr})$ (dyne/cm^2)	Instantaneous Extensional Viscosity (poise)
0	0.393	0	0
1	0.390	161	8944
2	0.387	243	9003
3	0.383	321	13508
4	0.380	360	17851
5	0.376	401	20011
6	0.373	433	22250
7	0.370	449	24099
8	0.366	430	24960
9	0.363	445	23907
10	0.360	441	24757

Table IV-1-19. Stress Growth Data of PIB at $\dot{\gamma} = 0.020\ sec^{-1}$

Time (sec)	Radius (cm)	$(\Pi_{zz} - \Pi_{rr})$ (dyne/cm^2)	Instantaneous Extensional Viscosity (poise)
0	0.386	0	0
1	0.383	131	6524
2	0.378	258	12911
3	0.375	318	15885
4	0.372	360	18040
5	0.369	379	18960
6	0.366	434	21685
7	0.362	475	23812
8	0.359	529	26416
9	0.356	576	28770
10	0.353	571	28531
11	0.349	592	29605
12	0.346	605	30250
13	0.342	617	30841
14	0.339	612	30594

Table IV-1-20. Stress Growth Data of PIB at $\dot{\gamma} = 0.0202\ sec^{-1}$

Time (sec)	Radius (cm)	$(\Pi_{zz} - \Pi_{rr})$ (dyne/cm^2)	Instantaneous Extensional Viscosity (poise)
0	0.322	0	0
1	0.320	133	6605
2	0.317	232	11502
3	0.314	303	15001
4	0.310	426	21102
5	0.307	453	22413
6	0.304	513	25409
7	0.301	508	25003
8	0.298	503	24900
9	0.295	473	24500
10	0.292	517	25873
11	0.289	519	26008

Table IV-1-21. Stress Growth Data of PIB at $\dot{\gamma} = 0.0232\ sec^{-1}$

Time (sec)	Radius (cm)	$(\Pi_{zz} - \Pi_{rr})$ (dyne/cm^2)	Instantaneous Extensional Viscosity (poise)
0	0.319	0	0
1	0.317	130.2	5600
2	0.313	313.2	13511
3	0.310	374	16122
4	0.306	405	17472
5	0.303	518	22324
6	0.299	598	25771
7	0.296	588	25321
8	0.2922	607	26199
9	0.289	638	27484
10	0.286	631	27182
11	0.282	624	26868

Table IV-1-22. Stress Growth Data of PIB at $\dot{\gamma} = 0.0253 \text{ sec}^{-1}$

Time (sec)	Radius (cm)	$(\Pi_{zz} - \Pi_{rr})$ (dyne/cm^2)	Instantaneous Extensional Viscosity (poise)
0	0.323	0	0
1	0.321	153	6052
2	0.317	228	9034
3	0.313	355	14022
4	0.309	431	17034
5	0.305	534	21120
6	0.301	683	26977
7	0.297	714	28216
8	0.294	707	27938
9	0.290	702	27717
10	0.286	696	27524
11	0.283	698	27579
12	0.279	689	27234
13	0.276	695	27450

Table IV-1-23. Stress Growth Data of PIB at $\dot{\gamma}$ = 0.0279 sec^{-1}

Time (sec)	Radius (cm)	$(\Pi_{zz}-\Pi_{rr})$ (dyne/cm^2)	Instantaneous Extensional Viscosity (poise)
0	0.336	0	0
1	0.329	248	8890
2	0.326	374	13421
3	0.322	579	20761
4	0.318	757	27114
5	0.314	868	31112
6	0.310	895	32067
7	0.306	942	33623

Table IV-1-24. Stress Growth Data of PIB at $\dot{\gamma}$ = 0.0283 sec^{-1}

Time (sec)	Radius (cm)	$(\Pi_{zz}-\Pi_{rr})$ (dyne/cm^2)	Instantaneous Extensional Viscosity (poise)
0	0.353	0	0
1	0.341	657	23219
2	0.337	670	23678
3	0.333	797	28188
4	0.328	903	31913
5	0.324	897	31687
6	0.319	996	35234
7	0.314	944	33407
8	0.311	1025	36277
9	0.306	1039	36756

Table IV-1-25. Stress Growth Data of PIB at $\dot{\gamma}$ = 0.029 sec^{-1}

Time (sec)	Radius (cm)	$(\Pi_{zz}-\Pi_{rr})$ (dyne/cm^2)	Instantaneous Extensional Viscosity (poise)
0	0.356	0	0
1	0.346	233	8050
2	0.338	322	11152
3	0.334	536	18551
4	0.329	739	25555
5	0.323	866	30002
6	0.319	970	33558
7	0.315	1041	36001
8	0.311	1011	34980
9	0.308	1068	36937

Table IV-1-26. Stress Growth Data of PIB at $\dot{\gamma}$ = 0.031 sec^{-1}

Time (sec)	Radius (cm)	$(\Pi_{zz}-\Pi_{rr})$ (dyne/cm^2)	Instantaneous Extensional Viscosity (poise)
0	0.326	0	0
1	0.321	249	8050
2	0.317	419	13523
3	0.312	623	20080
4	0.306	812	26202
5	0.301	1005	32865
6	0.298	1032	33739
7	0.293	1080	35298
8	0.289	1088	35569

Table IV-1-27. Stress Growth Data of PIB at $\dot{\gamma} = 0.0345\ \text{sec}^{-1}$

Time (sec)	Radius (cm)	$(\Pi_{zz} - \Pi_{rr})$ (dyne/cm^2)	Instantaneous Extensional Viscosity (poise)
0	0.334	0	0
0.5	0.333	85	2455
1	0.331	254	7360
1.5	0.326	380	11018
2	0.324	547	15843
3	0.318	854	24750
4	0.313	1074	31131
5	0.308	1207	34968

Table IV-1-28. Stress Growth Data of PIB at $\dot{\gamma} = 0.0358\ \text{sec}^{-1}$

Time (sec)	Radius (cm)	$(\Pi_{zz} - \Pi_{rr})$ (dyne/cm^2)	Instantaneous Extensional Viscosity (poise)
0	0.352	0	0
0.5	0.350	124	3472
1	0.347	250	6989
1.5	0.345	481	13447
2	0.342	700	19563
2.5	0.339	882	24654
3	0.337	1078	30139
3.5	0.333	1188	33227
4	0.330	1270	35496

Table IV-1-29. Stress Growth Data of PAA at $\dot{\gamma}$ = 0.0064 sec^{-1}

Time (sec)	Radius (cm)	$(\Pi_{zz} - \Pi_{rr})$ (dyne/cm2)	Instantaneous Extensional Viscosity (poise)
0	0.277	0	0
1	0.276	84	13129
2	0.275	88	13744
3	0.273	95	14834
4	0.273	98	15250
5	0.272	103	15983
6	0.272	111	17283
7	0.271	131	20473
8	0.270	136	21178
9	0.269	135	21011
10	0.269	141	21914
12	0.267	166	25878
14	0.265	170	26467
16	0.264	183	28454
18	0.262	186	28989

Table IV-1-30. Stress Growth Data of PAA at $\dot{\gamma} = 0.0076\ sec^{-1}$

Time (sec)	Radius (cm)	$(\Pi_{zz}-\Pi_{rr})$ (dyne/cm^2)	Instantaneous Extensional Viscosity (poise)
0	0.331	0	0
1	0.328	99	13002
2	0.328	107	14015
3	0.326	118	15502
4	0.325	128	16721
5	0.323	128	16774
6	0.322	132	17250
7	0.321	153	20010
8	0.320	156	20512
9	0.319	166	21734
10	0.319	172	22522
12	0.315	191	25014
14	0.313	210	27532
16	0.310	146	32251
18	0.308	251	32887
20	0.305	251	32840

Table IV-1-31. Stress Growth Data of PAA at $\dot{\gamma}$ = 0.0084 sec^{-1}

Time (sec)	Radius (cm)	$(\Pi_{zz}-\Pi_{rr})$ (dyne/cm^2)	Instantaneous Extensional Viscosity (poise)
0	0.323	0	0
1	0.321	112	13389
2	0.320	120	14312
3	0.319	110	13141
4	0.318	127	15109
5	0.317	132	15744
6	0.316	143	17132
7	0.314	154	18431
8	0.312	157	18686
9	0.311	172	20543
10	0.310	174	20787
12	0.307	189	22573
14	0.305	223	26719
16	0.302	237	28225
18	0.300	262	31302
20	0.297	266	31899

Table IV-1-32. Stress Growth Data of PAA at $\dot{\gamma}$ = 0.0088 sec^{-1}

Time (sec)	Radius (cm)	$(\Pi_{zz} - \Pi_{rr})$ (dyne/cm^2)	Instantaneous Extensional Viscosity (poise)
0	0.310	0	0
1	0.299	95	10814
2	0.298	124	14060
3	0.296	128	14531
4	0.296	137	15568
5	0.294	151	17176
6	0.292	170	19298
7	0.292	180	20423
8	0.289	192	21766
9	0.288	212	24063
10	0.287	226	25750
12	0.285	248	28144
14	0.282	286	32475
16	0.279	285	32439
18	0.277	286	32491
20	0.274	286	32505

Table IV-1-33. Stress Growth Data of PAA at $\dot{\gamma} = 0.0094\ \mathrm{sec}^{-1}$

Time (sec)	Radius (cm)	$(\Pi_{zz} - \Pi_{rr})$ (dyne/cm^2)	Instantaneous Extensional Viscosity (poise)
0	0.312	0	0
1	0.307	119	12634
2	0.306	125	13230
3	0.304	123	13018
4	0.302	124	13177
5	0.301	135	14325
6	0.300	150	15982
7	0.298	162	17145
8	0.297	160	16965
9	0.296	160	16883
10	0.294	184	19589
12	0.292	217	23108
14	0.289	255	27112
16	0.286	284	30176
18	0.283	298	31655
20	0.281	313	33149

Table IV-1-34. Stress Growth Data of PAA at $\dot{\gamma} = 0.0105 \text{ sec}^{-1}$

Time (sec)	Radius (cm)	$(\pi_{zz}-\pi_{rr})$ (dyne/cm^2)	Instantaneous Extensional Viscosity (poise)
0	0.292	0	0
1	0.290	190	18079
2	0.288	195	18567
3	0.287	200	19120
4	0.285	221	21060
5	0.284	235	22408
6	0.283	250	23766
7	0.280	271	25797
8	0.279	269	25646
9	0.278	310	29541
10	0.276	321	30605
12	0.273	377	35905
14	0.270	371	35345

Table IV-1-35. Stress Growth Data of PAA at $\dot{\gamma}$ = 0.012 sec^{-1}

Time (sec)	Radius (cm)	$(\Pi_{zz}-\Pi_{rr})$ (dyne/cm^2)	Instantaneous Extensional Viscosity (poise)
0	0.309	0	0
1	0.307	200	16697
2	0.305	259	21612
3	0.303	273	22767
4	0.301	284	23658
5	0.299	307	25648
6	0.297	322	26928
7	0.296	344	28678
8	0.294	341	28477
9	0.293	359	29948
10	0.290	411	34249
12	0.286	428	35685
14	0.283	440	36701

Table IV-1-36. Stress Growth Data of PAA at $\dot{\gamma} = 0.0136 \text{ sec}^{-1}$

Time (sec)	Radius (cm)	$(\Pi_{zz} - \Pi_{rr})$ (dyne/cm^2)	Instantaneous Extensional Viscosity (poise)
0	0.369	0	0
1	0.365	380	27941
2	0.363	406	29898
3	0.360	415	30488
4	0.358	418	30739
5	0.356	407	29912
6	0.355	415	30537
7	0.351	428	31424
8	0.349	436	32014
9	0.346	444	32607
10	0.344	467	34337
12	0.338	514	37874
14	0.334	527	38760

Table IV-1-37. Stress Growth Data of PAA at $\dot{\gamma}$ = 0.0142 sec^{-1}

Time (sec)	Radius (cm)	$(\Pi_{zz} - \Pi_{rr})$ (dyne/cm^2)	Instantaneous Extensional Viscosity (poise)
0	0.333	0	0
1	0.332	281	19730
2	0.329	316	22211
3	0.327	332	23362
4	0.324	362	25404
5	0.322	379	25915
6	0.320	400	28105
7	0.318	423	29716
8	0.316	436	30631
9	0.314	459	32257
10	0.311	487	34259
12	0.307	526	36977
14	0.302	541	38021
16	0.298	561	39412
18	0.294	566	39777

Table IV-1-38. Stress Growth Data of PAA at $\dot{\gamma}$ = 0.0159 sec^{-1}

Time (sec)	Radius (cm)	$(\Pi_{zz} - \Pi_{rr})$ (dyne/cm^2)	Instantaneous Extensional Viscosity (poise)
0	0.325	0	0
1	0.320	392	24669
2	0.312	444	27877
3	0.309	482	30285
4	0.307	490	30821
5	0.304	509	32004
6	0.302	528	33197
7	0.299	541	34049
8	0.297	546	34380
9	0.295	622	39164
10	0.293	667	41274
12	0.288	777	48086
14	0.284	895	56273

IV-2. Approximate Creep Data

Table IV-2-1. Approximate Creep Data of Newtonian Silicone Oil at $\left(\frac{\Delta\rho\omega^2 R^2}{z}\right)$ =215 dyne/cm^2

Time (sec)	Radius (cm)	Extensional Strain	$(\Pi_{zz}-\Pi_{rr})$ (dyne/cm^2)	Instantaneous Extensional Viscosity (poise)
0	0.394	0	0	0
1	0.389	0.024	103	18100
2	0.387	0.034	100	18096
3	0.386	0.039	98	17807
4	0.385	0.045	97	17668
5	0.384	0.050	95	17152
6.4	0.382	0.059	92	16663.6
7	0.381	0.062	91	16482.7
8	0.380	0.067	89	16164
9	0.379	0.073	88	15831
10.8	0.378	0.081	84.7	15330.2

Table IV-2-2. Approximate Creep Data of Newtonian Silicone Oil at $\left(\frac{\Delta\rho\omega^2 R^2}{z}\right)$ =341 dyne/cm^2

Time (sec)	Radius (cm)	Extensional Strain	$(\Pi_{zz}-\Pi_{rr})$ (dyne/cm^2)	Instantaneous Extensional Viscosity (poise)
0	0.373	0	0	0
0.2	0.368	0.029	233	18500
0.4	0.367	0.031	229	18153
1	0.366	0.037	227	18015
2	0.364	0.050	224	17738
3	0.362	0.063	219	17380
4	0.360	0.075	215	17047
5	0.357	0.088	211	16716
6	0.355	0.101	216	16365
7	0.353	0.113	202	16012
8	0.351	0.126	197	15650
9	0.348	0.138	193	15277
10	0.346	0.151	188	14889

Table IV-2-3. Approximate Creep Data of Newtonian Silicone Oil at $\left(\frac{\Delta\rho\omega^2R^2}{z}\right)$ =495 dyne/cm^2

Time (sec)	Radius (cm)	Extensional Strain	$(\Pi_{zz}-\Pi_{rr})$ (dyne/cm^2)	Instantaneous Extensional Viscosity (poise)
0	0.465	0	0	0
1	0.455	0.046	440	18326
2	0.448	0.077	431	17967
3	0.443	0.100	425	17692
4	0.438	0.122	418	17401
5	0.433	0.145	410	17093
6	0.429	0.166	403	16798
7	0.425	0.184	397	16529
8	0.419	0.212	386	16100
9	0.415	0.228	380	15836
10	0.409	0.258	378	15740

Table IV-2-4. Approximate Creep Data of Newtonian Silicone Oil at $\left(\frac{\Delta\rho\omega^2R^2}{z}\right)$ =661 dyne/cm^2

Time (sec)	Radius (cm)	Extensional Strain	$(\Pi_{zz}-\Pi_{rr})$ (dyne/cm^2)	Instantaneous Extensional Viscosity (poise)
0	0.539	0	0	0
0.5	0.531	0.036	577	19256
0.7	0.529	0.424	576	19213
0.9	0.528	0.424	575	19166
1.5	0.522	0.064	570	18966
2.5	0.514	0.095	560	18666
3.5	0.509	0.115	557	18566
4.5	0.501	0.146	548	18266
5.5	0.495	0.169	541	18033
6.5	0.489	0.196	533	17776
7.5	0.481	0.228	523	17430
8.5	0.476	0.249	516	17183
9.5	0.468	0.282	503	16767
10.5	0.462	0.309	493	16433

Table IV-2-5. Approximate Creep Data of PIB at $\left(\frac{\Delta\rho\omega^2 R^2}{2}\right)$ =373 dyne/cm^2

Time (sec)	Radius (cm)	Extensional Strain	$(\Pi_{zz}-\Pi_{rr})$ (dyne/cm^2)
0	0.380	0	0
1	0.374	0.031	310
2	0.371	0.046	307
3	0.368	0.062	304
4	0.366	0.077	302
5	0.363	0.090	299
6	0.361	0.104	296
7	0.359	0.116	294
8	0.356	0.128	292
9	0.354	0.144	288
10	0.352	0.154	286
11	0.350	0.166	283
12	0.348	0.177	281
13	0.346	0.189	278
14	0.343	0.204	275
15	0.342	0.211	273

Table IV-2-6. Approximate Creep Data of PIB at$\left(\frac{\Delta\rho\omega^2 R^2}{2}\right)$ =433 dyne/cm^2

Time (sec)	Radius (cm)	Extensional Strain	$(\Pi_{zz}-\Pi_{rr})$ (dyne/cm^2)
0	0.355	0	0
1	0.352	0.015	368
2	0.348	0.037	364
3	0.345	0.056	361
4	0.342	0.076	357
5	0.338	0.094	353
6	0.335	0.114	349
7	0.333	0.130	346
8	0.330	0.147	341
9	0.327	0.161	338
10	0.325	0.175	335
11	0.323	0.189	331
12	0.320	0.207	327
13	0.318	0.217	324
14	0.316	0.231	320
15	0.314	0.246	316

Table IV-2-7. Approximate Creep Data of PIB at $\left(\frac{\Delta\rho\omega^2R^2}{z}\right)$ =690 dyne/cm^2

Time (sec)	Radius (cm)	Extensional Strain	$(\Pi_{zz}-\Pi_{rr})$ (dyne/cm^2)
0	0.388	0	0
1	0.378	0.053	625
2	0.374	0.074	621
3	0.371	0.093	618
4	0.368	0.107	615
5	0.362	0.138	609
6	0.358	0.161	604
7	0.354	0.184	599
8	0.351	0.202	595
9	0.348	0.220	590
10	0.344	0.240	585
11	0.340	0.263	580
12	0.337	0.281	574

Table IV-2-8. Approximate Creep Data of PIB at $\left(\frac{\Delta\rho\omega^2R^2}{z}\right)$ =947 dyne/cm^2

Time (sec)	Radius (cm)	Extensional Strain	$(\Pi_{zz}-\Pi_{rr})$ (dyne/cm^2)
0	0.392	0	0
1	0.377	0.081	877
2	0.371	0.110	871
3	0.366	0.141	865
4	0.361	0.164	860
5	0.358	0.183	856
6	0.352	0.216	848
7	0.349	0.235	843
8	0.344	0.260	837
9	0.341	0.281	831
10	0.337	0.306	824
11	0.334	0.320	819

Table IV-2-9. Approximate Creep Data of PIB at $\left(\frac{\Delta\rho\omega^2R^2}{2}\right)$ =1233 dyne/cm^2

Time (sec)	Radius (cm)	Extensional Strain	$(\Pi_{zz}-\Pi_{rr})$ (dyne/cm^2)
0	0.354	0	0
1	0.336	0.104	1251
2	0.330	0.140	1243
3	0.326	0.170	1236
4	0.321	0.198	1229
5	0.316	0.228	1221
6	0.312	0.253	1214

Table IV-2-10. Approximate Creep Data of PAA at $\left(\frac{\Delta\rho\omega^2R^2}{2}\right)$ =188 dyne/cm^2

Time (sec)	Radius (cm)	Extensional Strain	$(\Pi_{zz}-\Pi_{rr})$ (dyne/cm^2)
0	0.362	0	0
1	0.360	0.016	136
2	0.359	0.020	135
3	0.358	0.025	134
4	0.357	0.030	134
5	0.357	0.032	133
6	0.356	0.037	133
7	0.355	0.040	132
8	0.354	0.044	132
9	0.354	0.046	131
10	0.353	0.053	130
11	0.352	0.056	129
12	0.352	0.058	129
13	0.351	0.064	129

Table IV-2-11. Approximate Creep Data of PAA at $\left(\frac{\Delta\rho\omega^2 R^2}{2}\right)$ =265 dyne/cm^2

Time (sec)	Radius (cm)	Extensional Strain	$(\Pi_{zz}-\Pi_{rr})$ (dyne/cm^2)
0	0.402	0	0
1	0.397	0.023	225
2	0.396	0.029	224
3	0.394	0.037	223
4	0.394	0.039	223
5	0.392	0.047	222
6	0.391	0.053	222
7	0.391	0.056	221
8	0.388	0.067	220
9	0.387	0.074	220
10	0.386	0.077	219
11	0.385	0.083	218
12	0.384	0.090	217
13	0.382	0.099	216

Table IV-2-12. Approximate Creep Data of PAA at $\left(\frac{\Delta\rho\omega^2 R^2}{2}\right)$ =365 dyne/cm^2

Time (sec)	Radius (cm)	Extensional Strain	$(\Pi_{zz}-\Pi_{rr})$ (dyne/cm^2)
0	0.424	0	0
1	0.421	0.015	328
2	0.417	0.037	326
3	0.415	0.046	325
4	0.412	0.060	323
5	0.409	0.074	322
6	0.406	0.087	320
7	0.405	0.096	319
8	0.402	0.107	318
9	0.401	0.115	317
10	0.399	0.126	315
12	0.395	0.137	313
14	0.391	0.145	310

Table IV-2-13. Approximate Creep Data of PAA at $\left(\frac{\Delta\rho\omega^2R^2}{2}\right)$ =416 dyne/cm^2

Time (sec)	Radius (cm)	Extensional Strain	$(\Pi_{zz}-\Pi_{rr})$ (dyne/cm^2)
0	0.389	0	0
1	0.384	0.026	374
2	0.381	0.045	372
3	0.377	0.066	369
4	0.374	0.078	368
5	0.372	0.094	366
6	0.368	0.113	363
7	0.365	0.127	362
8	0.363	0.141	360
9	0.360	0.155	358
10	0.359	0.165	356
12	0.355	0.185	353
14	0.351	0.206	350
16	0.348	0.226	346
18	0.344	0.247	343

Table IV-2-14. Approximate Creep Data of PAA at $\left(\frac{\Delta\rho\omega^2R^2}{2}\right)$ =458 dyne/cm^2

Time (sec)	Radius (cm)	Extensional Strain	$(\Pi_{zz}-\Pi_{rr})$ (dyne/cm^2)
0	0.382	0	0
1	0.373	0.047	413
2	0.368	0.071	410
3	0.364	0.094	407
4	0.361	0.111	405
5	0.356	0.138	401
6	0.354	0.152	399
7	0.351	0.167	397
8	0.349	0.180	395
9	0.347	0.189	394
10	0.345	0.200	392
11	0.344	0.212	390
12	0.342	0.222	388
13	0.340	0.232	386
14	0.338	0.243	384
16	0.334	0.264	383
18	0.331	0.286	376
20	0.329	0.299	374

Table IV-2-15. Approximate Creep Data of PAA at $\left(\frac{\Delta\rho\omega^2R^2}{2}\right)$ =641 dyne/cm^2

Time (sec)	Radius (cm)	Extensional Strain	$(\Pi_{zz}-\Pi_{rr})$ (dyne/cm^2)
0	0.452	0	0
1	0.447	0.023	605
2	0.440	0.052	603
3	0.434	0.078	600
4	0.430	0.097	598
5	0.425	0.120	595
6	0.421	0.141	593
7	0.415	0.168	589
8	0.412	0.182	587
9	0.408	0.205	584
10	0.405	0.221	582
12	0.398	0.253	577
14	0.388	0.299	569
16	0.384	0.327	565
18	0.378	0.354	560
20	0.374	0.379	555
22	0.369	0.405	549
24	0.364	0.433	543

Table IV-2-16. Approximate Creep Data of PAA at $\left(\frac{\Delta\rho\omega^2R^2}{2}\right)$ =748 dyne/cm^2

Time (sec)	Radius (cm)	Extensional Strain	$(\Pi_{zz}-\Pi_{rr})$ (dyne/cm^2)
0	0.446	0	0
1	0.436	0.046	710
2	0.428	0.083	706
3	0.420	0.124	701
4	0.412	0.161	697
5	0.403	0.203	691
6	0.398	0.230	687
7	0.392	0.263	682
8	0.384	0.299	676
9	0.384	0.304	675
10	0.376	0.345	667
12	0.367	0.391	658
14	0.362	0.420	652
16	0.357	0.449	645
18	0.351	0.479	638
20	0.347	0.507	631
22	0.341	0.537	623
24	0.336	0.566	614
26	0.332	0.595	605

Table IV-2-17. Approximate Creep Data of PAA at $\left(\frac{\Delta\rho\omega^2R^2}{2}\right)$ =837 dyne/cm^2

Time (sec)	Radius (cm)	Extensional Strain	$(\Pi_{zz}-\Pi_{rr})$ (dyne/cm^2)
0	0.446	0	0
1	0.443	0.014	802
2	0.430	0.074	796
3	0.424	0.101	793
4	0.416	0.143	788
5	0.407	0.184	782
6	0.399	0.226	777
7	0.393	0.256	772
8	0.387	0.285	767
9	0.381	0.318	761
10	0.376	0.345	756
12	0.365	0.401	745
14	0.356	0.455	733
16	0.351	0.484	726
18	0.347	0.507	720
20	0.342	0.536	712
22	0.336	0.566	703
24	0.330	0.603	691

IV-3. Steady Extensional Viscosity Data

Table IV-3-1. Steady Extensional Flow Data of PIB

Extension Rate (sec^{-1})	Extensional Viscosity (poise)
0.0055	20990
0.0082	20270
0.0086	20340
0.0105	22650
0.0125	22810
0.0130	23830
0.0161	26660
0.0180	25000
0.0200	29500
0.0202	26010
0.0215	27880
0.0233	29120
0.0234	33500
0.0257	32900
0.0279	33620
0.0280	36760
0.0289	36940
0.0299	37730
0.03	41800
0.0302	38600

Table IV-3-2. Steady Extensional Flow Data of PAA

Extension Rate (sec^{-1})	Extensional Viscosity (poise)
0.0035	29800
0.0043	31080
0.0062	31300
0.00643	29500
0.007	31500
0.0072	30550
0.0073	31800
0.0076	32800
0.0078	33100
0.0081	33300
0.0088	33510
0.009	34630
0.00911	34780
0.00942	33900
0.01	34830
0.0105	35910
0.0107	36030
0.0125	38400
0.0132	43490
0.0135	39840
0.0142	40000
0.0144	43940
0.0148	48710

NOMENCLATURE

A	(1) amplitude ratio in the superimposed shear oscillatory (2) gain of the comparator
a_i	parameters in Equation (6-2-12)
$\bar{a}_i$	parameters in Equation (2-1-1)
a_o	amplitude defined in Equation (4-1-3)
a_s	shear rate defined in Equation (2-1-5)
b	parameter in Equation (6-2-2)
c	parameter in Equation (6-2-4)
A_m, B_m, C_m, D_m	constants in Equation (4-2-23)
$C_{mn}^{(t)}$	Cauchy-Green Strain tensor
D	drop diameter
E	parameter defined in Equation (6-2-20)
E^4	equal to $\left(\frac{\partial^2}{\partial r^2}+\frac{1-\hat{\eta}^2}{r^2}\frac{\partial^2}{\partial \hat{\eta}^2}\right)^2$ in spherical coordinate system where $\hat{\eta} = \cos\theta$
G	density ratio of the outer phase to the drop phase used in numerical simulations
G'	dynamic rigidity
G_I, G_{II}, G_{III}	kernel functions in the Goddard memory integral expansion
$g(t', t'')$	function introduced in Equation (6-2-2)
$g(t', t'', t''')$	function introduced in Equation (6-2-4)
g_{ij}	covariant components of the metric tensor (fixed components)
g^{ij}	contravariant components of the metric tensor (fixed components)
H	curvature at the horizontal end of the drop
$\bar{H}$	drop curvature

H_o	drop curvature defined in Section 4-2-1
H_{ij}	tensor functional
J	slope of the output signal from the logarithmic amplifier vs. time
K_1, K_2	scale factor in the controller
K_c	gain of the controller
K_{TC}	tachometer constant
$L(t)$	instantaneous length of the drop
$L(s), G(s)$	transfer function of a lumped device defined in Section I-4
$m(t-t', \dot{\underset{\sim}{\gamma}})$	memory function in the B-C model
n	direction normal to the drop surface
P_o	pressure along the axis outside the drop
P_m	Legendre Polynomial of degree m
$\bar{P}_m(x)$	defined as $\int_{-1}^{x} P_m(x')dx'$
R_1, R_2	radii of the principal curvatures defined by Equation (4-2-5)
R_c	radius at the center of a horizontal drop
R_e	dimensionless radius at the horizontal end of the drop
R_o	starting drop radius
$R_{o_{max}}$	maximum possible starting drop radius
$\bar{R}(\theta)$	dimensional drop surface
$R_D(\theta)$	dimensionless drop surface
RE	Reynolds number defined as $\frac{\Delta\rho R_o^2 \omega_o}{\mu}$
S	defined as ω/ω_o in Section 4-2-2
S_D	output signal from the quadratic inverter
S_P	signal from the photomultiplier tube
S_F	signal from the function generator

S_V	visual drop diameter
$\bar{t}$	direction tangential to the drop surface in a meridonal plane
t, t'	present and past time respectively
Δt	defined as $\omega_0 \bar{\Delta t}$ where ω_0 is the initial rotational speed and $\bar{\Delta t}$ is the dimensional time interval
T	time period of drop elongation simulation
$(\bar{V}_r, \bar{V}_\theta, \bar{V}_\phi)$	dimensional velocity in spherical coordinate system
v_i	velocity in the Cartesian coordinate system
x_1, x_2, x_3	the Cartesian coordinates
x, x'	positions occupied at time=t and t' respectively
Z( )	Riemann Zeta function
$(\bar{r}, \bar{z})$ and (r, z)	coordinates of the drop at time=t and 0 respectively
r_0, z_0	semiaxes of the drop shape
$(\bar{r}, \theta, \phi)$	spherical coordinate system

GREEKS

Δ_{ij}	rate of deformation tensor
α_1, α_2	slope parameters in the Bird-Carreau model
α_a	angular acceleration defined in Section 2-4
α'	defined as $\frac{\Delta\rho\omega^2}{2\sigma}$ in Section 4-2-1
$\hat{\alpha}$	defined as $\tan^{-1}(-\frac{1}{\bar{R}}\frac{d\bar{R}}{d\theta})$
$\dot{\bar{\gamma}}$	extension rate
$\bar{\gamma}$	extensional strain
$\dot{\gamma}$	shear rate
α	defined as $\frac{\Delta\rho\omega^2 R^3}{2\sigma}$ in Section 2-4

$\dot{\gamma}_{max}$	maximum possible extension rate
$\underset{\sim}{\dot{\gamma}}$	rate of deformation tensor
K	defined by HR
$\bar{K}$	curvature defined by Equation (4-2-17)
π_{ij}	total stress tensor
τ_{ij}	extra stress tensor
π'_{ij}	total stress tensor of the continuous phase
δ_{ij}	delta function
$\lambda_i (i=1,5)$	time constants in Equation (6-2-12)
λ_1, λ_2	time constants in the Bird-Carreau model
$\lambda_{1p}, \lambda_{2p}, \eta_p$	parameters in Equation (6-2-22)
η_0	zero shear viscosity
η'_0	viscosity of the continuous phase in Section 2-4
$\hat{\eta}$	defined as $\cos\theta$
η'	dynamic viscosity
$\bar{\eta}^+$	instantaneous (apparent) extensional viscosity
$\bar{\eta}$	steady extensional viscosity
ω	(i) frequency in the superimposed shear oscillatory test
	(ii) rotational speed of the drop
ω_T	output signal of the tachometer
ω_0	rotational speed of the drop at time=0
ω_{max}	maximum speed of the drive motor
ρ, ρ_1	density of the drop phase
ρ', ρ_2	density of the continuous phase

μ, μ'	viscosities of the Newtonian drop and the continuous phases respectively, defined in the analysis in Section 4-2-2
ψ	stream function
Σ	defined by Equation (4-2-4)
$\bar{\Phi}$	phase difference in the superimposed shear oscillatory test
$\bar{\Theta}$	first normal stress coefficient
β	second normal stress coefficient
$\dot{\Sigma}$	corotating rate of deformation tensor
$\bar{\Gamma}^{ij}$	strain tensors defined in Equation (6-2-18)
Γ_{ij}	strain tensors defined in Equation (6-2-19)
σ	interfacial tension between the continuous and disperse phases

SUPERSCRIPTS

$*$	designates dimensionless